



**Development of Low-Dimensional Materials in Energy Scavenging**

**Kittirat Phooplub**

**A Thesis Submitted in Fulfillment of the Requirements for the  
Degree of Doctor of Philosophy in Physics  
Prince of Songkla University**

**2018**

**Copyright of Prince of Songkla University**



# **Development of Low-Dimensional Materials in Energy Scavenging**

**Kittirat Phooplub**

**A Thesis Submitted in Fulfillment of the Requirements for the  
Degree of Doctor of Philosophy in Physics**

**Prince of Songkla University**

**2018**

**Copyright of Prince of Songkla University**

**Thesis Title**            Development of Low-Dimensional Materials in Energy Scavenging

**Author**                    Mr.Kittirat Phooplub

**Major Program**        Physics

---

**Major Advisor:**

.....  
 (Assoc. Prof. Dr.Nantakan Muensit)

**Examining Committee:**

.....Chairperson  
 (Assoc. Prof. Dr.Soodkhet Pojprapai)

.....Committee  
 (Assoc. Prof. Dr.Jirut Meesane)

.....Committee  
 (Assoc. Prof. Dr.Nantakan Muensit)

The Graduate School, Prince of Songkla University, has approved this thesis as fulfillment of the requirements for the Doctor of Philosophy Degree in Physics.

.....  
 (Prof. Dr. Damrongsak Faroongsarng)  
 Dean of Graduate School

This is to certify that the work here submitted is the result of the candidate's own investigations. Due acknowledgement has been made of any assistance received.

.....Signature

(Assoc. Prof. Dr.Nantakan Muensit)

Major Advisor

.....Signature

(Mr.Kittirat Phooplub)

Candidate

I hereby certify that this work has not been accepted in substance for any degree, and is not being currently submitted in candidature for any degree.

.....Signature

(Mr. Kittirat Phooplub)

Candidate

ชื่อวิทยานิพนธ์	การพัฒนาวัสดุที่มีมิติต่ำในการดักจับพลังงาน
ผู้เขียน	นายกิตติรัตน์ ภู่วลัย
สาขาวิชา	ฟิสิกส์
ปีการศึกษา	2561

## บทคัดย่อ

วิทยานิพนธ์นี้รายงานการพัฒนาวัสดุที่มีมิติต่ำในการดักจับพลังงาน การศึกษาถูกแบ่งออกเป็น ส่วน 3 คือ การศึกษาระเบียบวิธีการดักจับพลังงาน การเตรียมและการศึกษาสมบัติของวัสดุโพซิโคโนลิทริก และ การประยุกต์ใช้ในการดักจับพลังงาน โดยในส่วนของพลังงานที่ได้รับความสนใจในวิทยานิพนธ์นี้คือ พลังงานกล ซึ่งเป็นแหล่งพลังงานที่พบได้ตั้งแต่ ในระดับโรงงาน เช่น การสั่นของเครื่องกล หรือในชีวิตประจำวัน เช่น การเคลื่อนไหวของส่วนต่าง ๆ ของร่างกาย ระเบียบวิธีที่ทำให้ความสนใจในงานนี้คือ ระเบียบวิธีโพซิโคโนลิทริก ซึ่งเป็นการแปลงพลังงานกลเป็นพลังงานไฟฟ้าโดยอาศัยวัสดุที่ไม่มีแกนสมมาตรรอบจุดศูนย์กลางของโครงสร้าง โดยระเบียบวิธีดังกล่าวมีข้อดีเหนือกว่าระเบียบวิธีอื่น คือ ไม่ต้องการแหล่งจ่ายไฟภายนอก และสามารถเก็บเกี่ยวพลังงานได้แม้อยู่ในบริเวณที่มีการสั่นที่ความถี่ต่ำ ส่วนที่สองเป็นการศึกษาวัสดุที่จะนำมาใช้ในการดักจับพลังงาน โดยวัสดุที่ทำให้ความสนใจในงานนี้คือ ซิงค์ออกไซด์ (ZnO) และ อิเล็กโตรแอคทีฟพอลิเมอร์ พีวีดีเอฟ เฮชเอฟพี P(VDF-HFP) ซิงค์ออกไซด์เป็นวัสดุที่ได้รับความสนใจอย่างแพร่หลาย ไม่ว่าจะเป็นด้าน อิเล็กทรอนิกส์ทางแสง เครื่องสำอาง หรือแม้แต่ด้านการเก็บเกี่ยวพลังงาน ซิงค์ออกไซด์ได้รับการศึกษาอย่างแพร่หลายและพบว่าเมื่อลดขนาดลงในระดับนาโน สมบัติทางโพซิโคโนลิทริกจะสูงขึ้น ในงานนี้ได้ศึกษาการเตรียมซิงค์ออกไซด์ระดับนาโนด้วยกระบวนการไฮโดรเทอร์มอล โดยได้มีการศึกษาตั้งแต่สารตั้งต้นที่ใช้ ความเข้มข้น และ สารละลายที่ใช้ โดยสามารถเตรียมได้ในรูปแบบที่แตกต่างกันไม่ว่าจะเป็น แท่งซิงค์ออกไซด์ระดับไมโครเมตร แท่งซิงค์ออกไซด์ระดับนาโนเมตร อนุภาคซิงค์ออกไซด์ระดับนาโน โดยสิ่งที่เป็นปัจจัยสำคัญในการกำหนดขนาดของซิงค์ออกไซด์ที่เตรียมได้ คือ ความเป็นขั้วของสารละลาย กรณีที่เตรียมน้ำ ซิงค์ออกไซด์ที่เตรียมได้จะมีขนาดใหญ่ แต่เมื่อเตรียมในสารละลายที่มีความเป็นขั้วต่ำ เช่น แอลกอฮอล์ ซิงค์ออกไซด์ที่ได้จะมีขนาดเล็กกลงในระดับ 10 นาโน ในส่วนของการศึกษาสมบัติได้ทำการศึกษาโดยกล้องจุลทรรศน์แรงอะตอม (AFM) โดยได้ศึกษาทั้งในส่วนสัญญาณวิทยา สมบัติโพซิโคโนลิทริก และ สมบัติทางกล โดยการศึกษาสมบัติโพซิโคโนลิทริกอาศัยเทคนิค piezoresponse force microscopy (PFM) โดยสามารถบอกได้ว่าซิงค์ออกไซด์ที่เตรียมขึ้นมีสมบัติโพซิโคโนลิทริก และยังบอกทิศของโพลาริเซชันได้อีกด้วย ส่วนสมบัติทางกลได้ศึกษาผ่านระเบียบวิธี force-distance microscopy ซึ่งเป็นระเบียบวิธีที่สามารถ ตรวจสอบสมบัติเชิงกลในระดับพิโกนิวตัน ได้ประยุกต์ระเบียบวิธีดังกล่าวเพื่อศึกษา สมบัติเชิงกลของวัสดุประกอบ

คอลลาเจน และ ซิงค์ออกไซด์ระดับนาโน โดยพบว่าซิงค์ออกไซด์ สามารถเพิ่มเสถียรภาพทางกลให้กับ คอลลาเจนได้ เมื่อตรวจพบแล้วว่าซิงค์ออกไซด์มีความเป็นไอโซอิเล็กทริกและยังมีผลต่อสมบัติเชิงกลของวัสดุ จึงได้นำซิงค์ออกไซด์รูปแบบต่าง ๆ ไปผสมกับ พีวีดีเอฟ เฮชเอฟพี เพื่อขึ้นรูปเป็นวัสดุเก็บเกี่ยวพลังงานโดยพบว่า วัสดุประกอบ พีวีดีเอฟ เฮชเอฟพี กับ แท่งซิงค์ออกไซด์ระดับนาโนให้ผลดีที่สุด โดยสามารถแปลงพลังงานจากการสั่น ได้ถึงระดับ 1 ไมโครวัตต์ ที่ความเข้มข้นในการผสม 2 เปอร์เซ็นต์โดยน้ำหนักซึ่ง ค่าพลังงานที่ได้สามารถนำไปประยุกต์ใช้กับไมโครคอนโทรลเลอร์ที่ใช้พลังงานต่ำได้อีกด้วย

<b>Thesis Title</b>	Development of low-dimensional materials in energy scavenging
<b>Author</b>	Mr. Kittirat Phooplub
<b>Major Program</b>	Physics
<b>Academic Year</b>	2018

### **Abstract**

This thesis work reported the development of low-dimensional material for energy scavenging. The study was separated into three parts, studying the energy scavenging methods, preparation and characterization of piezoelectric materials, and application in energy scavenging. The energy that was interested in this work was mechanical that was ambient energy in daily life. The energy could be either factory scale or human scale. To scavenge the energy, piezoelectric method was elected because the piezoelectric method provided the high voltage output and small mechanical damping without an external voltage source. The piezoelectric method used the material with non-centrosymmetric property to convert the mechanical energy into electrical energy. The second part was the material processing. The piezoelectric materials that was observed in this work were ZnO and P(VDF-HFP). ZnO had gained widespread attention in many application, for example, electronic, optic cosmetic, and energy harvesting. In the energy harvesting application, ZnO was found that the piezoelectric property was greater when the size of ZnO was reduced into nanoscale. In this work, ZnO was prepared via hydrothermal method. The effect of precursor, concentration and solvent were observed. Macrorod, nanorod and nanoparticle were successfully prepared. The polarity of the solvent was found to be the main parameter to determine the size of ZnO. Amount of 10 nm diameter was obtained when the ZnO was prepared in methanol. The prepared ZnO were characterized by using atomic force microscopy base. Topography, piezoresponse force microscopy (PFM) and force-distance curve were studied. From PFM resulted, prepared ZnO was piezoelectric material and the method could identify the direction of growing. ZnO was also observed for bioengineering application by mixing the ZnO into collagen film. The mechanical properties of the reinforce was observed by force-distance microscopy. From the result, ZnO enhanced the young's modulus and thermal stability of the collagen.



In energy harvesting application, ZnO was mixed into electroactive polymer P(VDF-HFP) to maximize the energy power. The effect of size, shape, and concentration of ZnO were tested. The result showed that the composite film 2 wt% ZnO nanorod P(VDF-HFP) generated electrical power upto 1  $\mu$ W that the power was enough for low-power microcontroller.

## Acknowledgements

The completion of this thesis would be quite impossible without the help of many people. I wish to express my gratitude to those who have contributed to the completion of this thesis:

I express my sincere thanks to my advisors, Associate Professor Dr. Nantakan Muensit for giving me the opportunity to work on my interested field, for their help, guidance, advice, encouragement, suggestion and support through the whole duration of this work.

I would like to thank The Royal Golden Jubilee (RGJ) Ph.D. Programme (PHD/0034/2553), the Graduate School Research Support Funding for Thesis 2011, the Center of Excellence in Nanotechnology for Energy (CENE), the Department of Physics, Faculty of Science, Prince of Songkla University, Hat Yai, Songkhla, Thailand for the financial supports. The AFM technical term was under a collaboration with Professor Dr. Andrei L Kholkin, Centre for Research in Ceramics and Composite Materials (CICECO), University of Aveiro, Aveiro, Portugal. The tissue engineering information was under an assistance with Associate Professor Dr. Jirut Meesane

I would like to thank all staffs of the Department of Physics and Department of Chemistry, Faculty of Science, Prince of Songkla University for document managements.

I also would like to thank the examination committee members of thesis for their valuable time.

Finally, I would like to thank:

Miss Sirirat Ouiganon who support me even when I lost my way; Most importantly, I wish to thank my family especially my mother for their love, understanding, trust and support throughout my life.

Kittirat Phooplub

## **The Relevant of the Research work to Thailand**

The purpose of this Doctor of Science Thesis in Physics is to develop a low-dimensional material to scavenge energy from waste energy source. The final device can generate power up to 1  $\mu\text{W}$  that is enough to supply to low power electric devices. The scavenging technology can reduce the using of battery and save the electric power.

## Contents

	<b>Page</b>
ABSTRACT (Thai)	v
ABSTRACT (English)	vii
ACKNOWLEDGEMENTS	ix
LIST OF TABLES	xiii
LIST OF FIGURES	xiv
<b>CHAPTER 1: INTRODUCTION AND THESIS OVERVIEW</b>	
1.1 Introduction and statement of the problems	1
1.2 Thesis outline	2
1.3 Objectives of research	3
<b>CHAPTER 2: PIEZOELECTRIC ENERGY HARVESTING</b>	4
2.1 Fundamental sources of energy and energy harvesting techniques	4
2.2 Piezoelectric energy harvesting	7
2.3 Constitutive equation for piezoelectric energy harvesting	10
2.4 Electromechanical coupling properties of fundamental shape	13
2.5 Piezoelectric energy harvesting method	17
2.6 Vibration mode of cantilever	18
2.7 Conclusions	26
<b>CHAPTER 3: SYNTHESYTE OF ZNO NANOSTRUCTURE AND SURFACE MODIFICATION</b>	27
3.1 Introduction	27
3.2 Theory of crystal growth and surface interaction	29
3.3 Materials and methods	35
3.4 Results and discussion	38
3.5 Conclusion	46
<b>CHAPTER 4: ATOMIC FORCE MICROSCOPY: AN APPLICATION FOR NANOSTRUCTURE CHARACTERIZATION</b>	48
4.1 Introduction	48
4.2 Atomic force microscopy	49
4.3 Force displacement curve spectroscopy	57

**Contents (Cont.)**

4.4 Application of force displacement curve in energy harvesting	59
4.5 Piezoresponse Force Microscopy (PFM)	60
4.6 Application of PFM	68
4.7 Conclusions	76
<b>CHAPTER 5: MICROPOWER ENERGY HARVESTING</b>	<b>77</b>
5.1 Introduction	77
5.2 Energy harvester and measurement setup	78
5.3 Effect of shape and size of ZnO to the performance of energy Harvester	82
5.4. Conclusion	84
<b>CHAPTER 6: CONCLUSIONS</b>	<b>86</b>

## List of Tables

<b>Table</b>	<b>Page</b>
Table 2.1 Types of fundamental piezoelectric relation (Ikeda, 1990).	11
Table 2.2 Matrix notation of symmetric tensors.	12
Table 2.3 Electromechanical in various vibration modes of piezoelectric material.	14
Table 2.4 Listed of physical properties of ZnO.	21
Table 2.5 The first six mode of vibration for hexagonal rod with different boundaries.	23
Table 2.6 Corresponding voltage according to deformation at characteristic frequency for hexagonal rod with different boundaries.	24
Table 2.7 Eigen frequency for hexagonal rod with different boundaries.	25
Table 3.1 Conclusion of pair interaction of atoms, or molecules (Isaelachvili, 1984).	33
Table 3.2 The ratio of the maximum intensity at plane (100) by (002) in each condition.	39
Table 4.1 List of contact cantilever from Applied NanoStructures, Inc.	52
Table 4.2 List of dynamic cantilevers from Applied NanoStructures, Inc.	52
Table 5.1 Material properties of P(VDV-HFP) with various concentrations of ZnO of different shapes (Phooplub and Muensit, 2018)	82

## List of Figures

<b>Figure</b>	<b>Page</b>
Figure 2.1 Number of publications of each year with a key word “piezoelectric vibration energy harvesting” by Thomson Reuters Web of Sciences.	7
Figure 2.2 Energy flow in development of piezoelectric energy harvester (Edited from Kim et al. 2007).	7
Figure 2.3 The crystal structures of ZnO, the red and the pink solid cycles are Zn and O atoms, respectively.	10
Figure 2.4 Schematic diagram of the linear and inertial-base generator (edited from Wei and Jing 2017).	17
Figure 2.5 Free-body diagram of infinitesimal cantilever in transverse mode.	19
Figure 2.6 The Relation between frequency of each modes of vibration of ZnO cantilever like with changed length.	25
Figure 3.1 The sketch of mechanism process of OA.	32
Figure 3.2 The relation between pH value and surface functional groups of ZnO (modified form Degen and Kosec, 2000).	34
Figure 3.3 Molecular structures of polyelectrolytes PDDA and PSS.	36
Figure 3.4 The XRD pattern of ZnO prepared by using 0.02 mole Zn(CH <sub>3</sub> COO) <sub>2</sub> ·2H <sub>2</sub> O with a) NaOH and b) KOH at 0.04, 0,08 and 0.16 mole.	38
Figure 3.5 SEM images of ZnO a) without CTAB b) with CTAB.	39
Figure 3.7 Absorption spectra during growth process of the ZnO prepared by using Zn(CH <sub>3</sub> COO) <sub>2</sub> ·2H <sub>2</sub> O and KOH as precursors in methanol solution.	40
Figure 3.8 TEM image of ZnO prepared by using methanol as the solvent with reaction time a) 3 h and b) 3 days (edited from Phooplub and Muensit 2018) and c) is a sketch of mechanism from nanoparticles to nanorods.	41

## List of Figures (Cont.)

<b>Figure</b>	<b>Page</b>
Figure 3.9 SEM image of a) low magnification and b) high magnification of vertical aligned ZnO nanorods on silicon wafer.	42
Figure 3.10 SEM image of ZnO microrods.	43
Figure 3.11 Zeta potential of ZnO in at different pH value.	43
Figure 3.12 Zeta potential coated ZnO nanorods.	44
Figure 3.13 a) absorption spectra of ZnO, PDDA and PSS, b) absorption spectrum of coated nanorod c) and d) TEM image of 1 layer and 2 layers of PSS/PDDA coated ZnO, respectively.	45
Figure 3.14 Time dependent of normalized absorbance peak of ZnO and Coated ZnO nanorods.	46
Figure 4.1 The sketched image of a) AFM cantilever and b) the photograph of ACL model (adapted form Applied NanoStructures, Inc., USA).	50
Figure 4.2 Resonant frequency of ACL cantilever model.	53
Figure 4.3 Schematic of AFM model easyscan2 (Nanosurf, Switzerland).	54
Figure 4.4 PID loop gain for Z controller in Nanosurf easyscan2 (Nanosurf, Switzerland)	55
Figure 4.5 The graphic user interface (GUI) of Nanosurf easyscan 2.	56
Figure 4.6 Topography image of ZnO nanorods vertical on glass slide.	57
Figure 4.7 The force distance curve.	58
Figure 4.8 Schematic diagram the piezoelectric force microscopy.	61
Figure 4.9 The cantilever deflection corresponding to crystal vibration (adapted from Soergel 2011)	65
Figure 4.10 The piezoresponse signal from lock-in-amplifier with respect to the polarization of piezoelectric grain (Editted from Soergel 2011)	67
Figure 4.11 The phase diagram of piezoresponse signal in case of with and without inherent background (Editted from Soergel 2011)	67
Figure 4.12 The deformation of ZnO hexagonal rod at 0o 45o and 90o degree from z axis. The color contour indicated the normalized electrical voltage.	68



### List of Figures (Cont.)

<b>Figure</b>	<b>Page</b>
Figure 4.13. Relation between deformation and rotational angle.	69
Figure 4.14 The deformation of rod when the cantilever tip was located at the middle side. The color contour indicated the normalized electrical voltage.	70
Figure 4.15 PFM characterization of commercial piezoelectric bimorph, a) topography image, b), c), d), e), and f) were PFM images of the bimorph at 20, 25, 30, 35, and 40 kHz, respectively.	71
Figure 4.16 The vibration spectrum of the cantilever located on the sample.	72
Figure 4.17 The observed a) topography image and b) PFM image of ZnO vertical aligned on the platinum coated silicon wafer. The observed c) topography image and d) PFM image of ZnO macrorods lied on the platinum coated silicon wafer. The bright and the dark represented the in-phase and out-off-phase of the PFM signal.	73
Figure 4.18 The observed topography and PFM images of ZnO macrorod with activated voltage peak a) and b) 1 V, c) and d) 3 V, e) and f) 5 V.	74
Figure 5.1 The structure of the energy harvester based ZnO P(VDF-HFP) nanocomposite (Phooplub and Muensit, 2018).	77
Figure 5.2 The Energy harvesting setup.	78
Figure 5.3 The energy harvesting software.	79
Figure 5.4 The LabVIEW source code for energy harvesting observation.	80
Figure 5.5 Curves of a) Open-circuit voltage output with different concentrations and forms of ZnO b) Obtained power with respect to the load resistance compared between bare P(VDF-HFP) and P(VDF-HFP) with 2 wt% NRs ZnO (Phooplub and Muensit, 2018).	82
Figure 5.6 Piezoelectric signal of 2 wt% NRs condition after rectified.	83

## List of Abbreviations

AFM	Atomic force microscope
CTAB	Cetyltrimethyl ammonium bromide
GUI	Graphic user interface
HFP	Hexafluoropropylene
HMTA	Hexamethylenetetramine
MET	Metabolic equivalent of task
MOCVD	Metalorganic chemical vapor deposition
MRs	Microrods
NPs	Nanoparticles
NRs	Nanorods
OA	Oriented attachment
PALS	Phase analysis light scattering
PDDA	Polydiallyldimethylammonium chloride
PFM	Piezoresponse force microscope
PID	Proportional–integral–derivative controller
PSS	Poly(styrenesulfonate)
PVDF	Poly(vinylidene fluoride)
PZT	Lead zirconate titanate
SEM	Scanning electron microscope
SFA	Surface force apparatus
TEM	Transmission electron microscope
TrFE	Trifluoroethylene
VLS	Vapor-liquid-solid
WSN	Wireless sensor network
ZnO	Zinc Oxide

## CHAPTER 1

### INTRODUCTION AND THESIS OVERVIEW

#### 1.1 Introduction and statement of the problems

A typical realization of renewable energy is a collection from natural resources in company with renewable energy technology such as sunlight, wind, rain, geothermal, and biomass. Most renewable energy is a clean energy providing sustainable benefits for human and particularly no harmful emission to climate. Several thousands of reports on clean energy mainly involve with physical structures relatively large in size. In this work, clean electrical energy via energy harvesting on a small scale of mechanical movements generated by nanostructure materials is a focus. A word “energy harvesting” is often taken place by “energy scavenging”. Although these two words are quite the same, the latter is, however, more related to irregular way of energy conversion from ambient sources. Novel technologies relating to scavenging energy from ambient vibrations such as noise and vibration have been developed for about a decade (Rahman and Hoque 2013, Fang, et al. 2018). In these technologies, traditional ferroelectric materials have been used because their coupling between mechanical and electrical properties can be done through the piezoelectric activity. In a similar period of time, low-dimensional structures of various materials have been discovered and systematically studied for various compositions and shapes (Wang, *et al.* 2006, Gao, *et al.* 2007, Cui, *et al.* 2016). The low-dimensional materials have been reported to have high potential application in optics, optoelectronics, catalysis, field effect transistor, ultrasensitive and piezoelectric. However, their applications in energy scavenging yet have not been extensively explored. This work thus aims to demonstrate the behavior of a low-dimensional material which is piezoelectric and the possibility of using the material to convert the mechanical deformation into the electrical energy that can be delivered to some ultra-low power electronic devices.

Energy conversion procedure is primarily concerned in this work. Because almost all nanomaterials have infinitesimal movements that are extremely hard to measure. Therefore, apart from fabricating nanomaterials, developing a useful

technique to explore a process of capturing ambient mechanical energy and converting it into useable electricity is inevitable. A mathematical insight has necessarily been laid down before validating by experimental.

Functional oxide-based nanostructures such as nanorod and nanobelt of zinc oxide (ZnO) have been chosen for a demonstration. This is because ZnO has unique properties which are semiconductor, piezoelectric and compatible with biological environment. Nanostructures of zinc oxide can be synthesized by several methods such as vapor liquid-solid method (Zhao *et al.* 2007), metal-organic chemical vapor deposition (Rivera, *et al.* 2015) and chemical method (Yu, *et al.* 2011). At first attempt, this work has fabricated ZnO by a solid state reaction. Afterwards, chemical reaction has been chosen. Material properties of ZnO have been characterized at the beginning via numerical methods. Several techniques, i.e., Atomic Force Microscope (AFM), Scanning Electron Microscope (SEM), Transmission Electron Microscope (TEM) etc. have been used as described in the respective chapters.

## **1.2 Thesis outline**

The thesis consists of 6 chapters. The statement of the problem and the objectives are presented in this chapter.

Chapter 2 addresses the background of clean energy generated by small and smart energy harvesting systems. The piezoelectricity including modeling and constitutive equations are mentioned.

Chapter 3 describes the physical and chemical reactions employed for preparing ZnO nanomaterials. Advantages and disadvantages of both techniques are discussed. Material properties for ZnO are included.

Chapter 4 application of atomic force microscope and synthesized ZnO nanomaterials implemented in tissue engineering technology and piezoelectric measurement.

Chapter 5 Focuses on development of micropower energy harvesting of smart polymer material benefited from ZnO.

Chapter 6 summarized the main findings presented in this work. Future outlook of the research is also placed in this Chapter.

### **1.3 Objectives of research**

1. To fabricate ZnO nanomaterials and investigate their energy conversion characteristics numerically and experimentally,

2. To enhance micropower energy harvesting of smart polymer material by synthesized ZnO nanomaterials.

3. To study the reinforcement of ZnO nanomaterials in biomaterial.

## CHAPTER 2

### PIEZOELECTRIC ENERGY HARVESTING

Finishing of a new power supply with self-powered and pollution free functions to feed a wireless sensor network (WSN) device is a major key in the energy management field. The concept of energy harvesting is brought in to account, particularly piezoelectric energy harvesting because the source of energy is stray energies in our living space and the size of the harvester is suitable for WSN devices.

Chapter 2 overviews the piezoelectric energy harvesting. The first topic is focused on the introduction of energy harvesting, basic principle, and development. The second part is involved piezoelectricity. Performance and interpretation of each structure are observed via classical calculation and helping of a numerical model.

#### 2.1 Fundamental sources of energy and energy harvesting techniques

Energy harvesting is the process to transfer an ambient energy source into electrical energy. The targeted energy sources are solar, thermal, vibration and wind. Energy from solar, wind and water sources are normally categorized to a large-scale of energy sources. The energy from the sources can be supplied to a household or factory scale. Energy harvesting plays an attention only to the small scale of the order of millijoules.

A temperature difference between the two regions results the heat energy transfer. When a machine is operated, the energy lost is generated in term of heat energy. The effect generates the temperature difference between the machine and the natural. The energy can be converted to electrical energy by a thermoelectric generator. The efficiency of the difference of the temperature. Amount of 3% is obtained at  $10^{\circ}\text{C } \Delta T$ , while 14% is at  $50^{\circ}\text{C}$ .

There are several methods to harvest the energy, for example, thermoelectric, thermionic, thermomagnetic, ferroelectric, and Nernst effect. Thermoelectric generator bases on Seebeck and Thompson effect. The n- and p-type

semiconductor materials are constructed to form of series of connected thermocouples. When the device is in the thermal gradient, the difference of the temperature generates electrical current. The electrical voltage generated from the device was the 2-3 voltage from the thermal difference over than 150°C with power around 1-2 watt. Eventhough the thermal energy harvesting is interesting, but the temperature of the human skin is around 32 to 35 °C that is different from surrounding around 5 °C (Webb. 1992). This result to generated voltage is in the scale of millivolt for a very thin film (Zhou, et al. 2018).

Mechanical energy that is kinetic and potential energy can be generated from either natural or man-made. The scale of the energy is verily from megajoule to nanojoule depended on the sources. Some of them are periodic and some are not. Example of periodic mechanical energy source is the vibration of the machine in the factory. The natural frequency is depended on the circuit in each country. Electric circuitry is normally operated at 50 Hz while some of the country, for example USA, is operated at 60 Hz.

Human motion is also interesting in the field. The motion is, for example, movement in daily life, performing basic body functions like respiration and blood circulation. This energy is classified to be the non-periodic mechanical energy. The spectrum of the motion is in very low frequency ( $< 200\text{Hz}$ ). The term of metabolic equivalent of task (MET) is used to determine the energy consumption physical activity of the human body(Ainsworth *et al.* 2011). It is defined as the ratio of metabolic rate and therefore the rate of energy consumption during a specific physical activity to a reference metabolic rate, set by 1.162 W/kg (Zhou, *et al.* 2018). The MET value can be classified into four levels, sedentary behavior (1.0-1.5 MET), light behavior (1.6-2.9), moderate behavior (3.0-5.9) and vigorous behavior ( $\geq 6\text{MET}$ ) (Ainsworth, et al. 2011). Amount of 1.162 W/kg can be obtained only watching television and the value can be reached to 22.078 W/kg from running at around 19 kph. Availability of the mechanical is enough to harvest.

Electrostatic, electromagnetic, piezoelectric and triboelectric are the four common methods to convert the energy. The four technique is based on Maxwell's equations. Electrostatic energy harvesting is an adaptive capacitor with movable

electrode. The energy is harvested according to the Ericsson cycles. When the mechanical force field is absent, the distance between the electrode is fixed. Charge and discharge only occur. When the distance of the electrode is forced by the mechanical energy, energy harvesting function is taken place. Triboelectric energy harvesters rely on friction contact of two materials with different polarities charge accumulation. The cycle of charge flow occurs during the repeating of contact and non-contact of the two material that is the effect of electrostatic induction.

Comparison of these four techniques, the piezoelectric technique provides the high voltage output, small mechanical damping, no voltage source required, no mechanical stoppers needed, and high energy density (Roundy, et al. 2003). The advantages are beneficially over the three techniques that the operation is required external power source for electrostatic technique (Roundy, et al. 2003), the efficiency at low frequency for electromagnetic technique (Miao, et al. 2006), and the durability is not satisfactory with electrostatic charge accumulation for triboelectric technique (Wang, et al. 2015). However, high impedance and low current of the piezoelectric of the technique must be resolved (Khan et al. 2014).



## 2.2 Piezoelectric energy harvesting

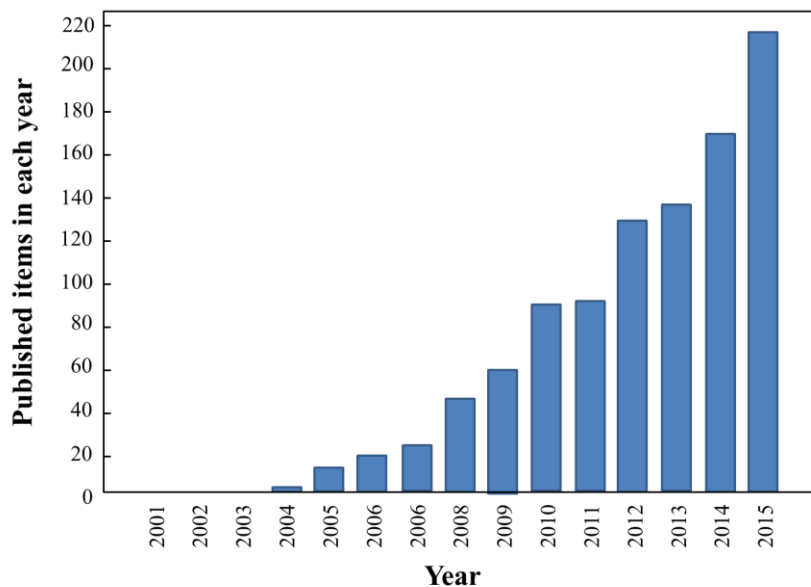


Figure. 2. 1. Number of publications of each year with a key word “piezoelectric vibration energy harvesting” by Thomson Reuters Web of Sciences.

Development of piezoelectric energy harvester is increasing for a decade. The publication of in the field is continually increased since 2001 as seen in the figure 2.1. The first publication is in the topic “Energy Harvesting Eel” by Allen and Smits in 2001. Flexible piezoelectric polyvinylidene difluoride membrane or another word “ell” was used to harvest energy from vertex stream. Nowadays, a lot of piezoelectric harvesters have been revealed.

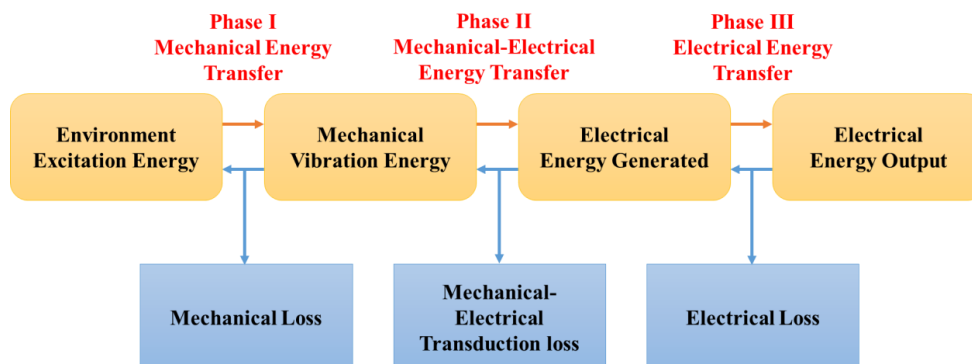


Figure 2.2. Energy flow in development of piezoelectric energy harvester (Edited from Kim et al. 2007).

The principle of energy flow in piezoelectric energy harvesting is conducted by Kim et al. as shown in figure 2.2. Designing of energy harvester must be matched to mechanical energy in the environment. Cantilever beam structure, a beam with fixed one end and free one end, is discussed in the field. The displacement is strongest at the free end of cantilever while the strain is strongest at the location nearly the fixed end. Most of the invention plate the piezoelectric around the root to obtain the maximum stress from the structure (Roundy and Wright 2004). The cantilever structure strongly vibrates when the structure is placed in the energy field with the frequency that matches to the cantilever of another word 'resonant frequency'. The resonant frequency of cantilever is depended on the dimensions of the beam. In case of the interesting mechanical source is single frequency vibration, if the resonance of the cantilever is tuned to match with the mechanical source the maximum energy is obtained.

Clamped circular plates is a structure to harvest the energy from compression. Kim and coworker develop the energy harvester that consist of the two dome-shaped metal end-caps glued on piezoelectric sheet called a piezoelectric 'cymbal' (Kim *et al.* 2004). The structure transfers the force in normal direction to radial direction.

Eventhough the mechanical energy transfer is important, but the efficiency of the device is still depended on piezoelectric material. Greater piezoelectric coefficient can highly generate electric power. Piezoelectric ceramics, polymer and semiconductor have their different advantage and disadvantage. Lead zirconate titanate (PZT) is a one of piezoelectric materials that widely used because the coupling coefficient is the greatest. Fang and co-worker have developed PZT based energy harvester in the cantilever structure. The harvester generated power peak around 2.16  $\mu\text{W}$  under resonant excitation with strength of 1 g acceleration with 609 Hz frequency (Fang, et al. 2006). Screen print unimorph silicon/PZT produced by Lei and their group in 2012 generated piezoelectric power 14 $\mu\text{W}$  with optimal load of 100k $\Omega$  from 1 g acceleration with 235 Hz. Limitation of the harvester with PZT that cannot be used at low frequency is the stiff of the material. In order to obtain the structure that operates at low power the size of the harvester should be increased. Another limitation is the

brittleness of the material, that made the device cannot be placed at the force field with large displacement.

Poly(vinylidene fluoride) (PVDF) is the most popular piezoelectric polymer. PVDF belongs to  $mm2$  crystal symmetry. The piezoelectricity of the polymer is depended on the conformation of the polymer structure. The highest polarization can be obtained when the fluoride is located the same side along the backbone. The phase is call  $\beta$ -phase. However, in the general condition of preparation, the non-polar phase ( $\alpha$ -phase) is obtained. To maximize the  $\beta$ -phase, post-process is required. Poling process, applying the external electric field at the temperature around 90-130 °C, enhanced the piezoelectric coefficient from 3.7 to 28 pC/N. However, the piezoelectric coefficient of the polymer is far away from the PZT.

Development of the piezoelectric polymer is relied on enhancement the piezoelectric coefficient and neglecting the post-process. A lot of dopant is brought in to account. Doping of graphene nanoparticle enhanced ferroelectric behavior and dielectric constant that was able to scavenges a maximum power of 36 nW (Rahman, et al. 2013). Lead zirconate titanate (PZT) immersed in the polymer improved the piezoelectric coefficient from -32 to 84 pC/N (Tiwari, et al. 2016). Modified P(VDF-HFP) by carbon black also shows higher performance which could reach the level of up to 561%. (Wu, et al. 2016).

Semiconductor is one of the popular piezoelectric materials, particularly, II-IV compound semiconductor. The advantage over the first two group is rectifying behavior when some metal is used as an electrode. This enable the harvester not only generate electrical power but also converse the AC signal to DC signal by without any external diode. the ZnO is a one of II-IV semiconducting material with multifunction that is used in many applications; cosmetic, antibacterial, electronic, photonic and piezoelectric. The crystal structure of ZnO is shared by three structure; wurtzite, zinc blende and rock salt (Figure 2.3). Wurtzite structure (6mm space group) is found in the thermodynamic stable phase that have the most non-zero piezoelectric elements in the three structures. Overlapping of two hexagonal Zn and O (Figure 2.3c) result to non-centrosymmetric. The distance between Zn and O resulted to the dipole in the material.

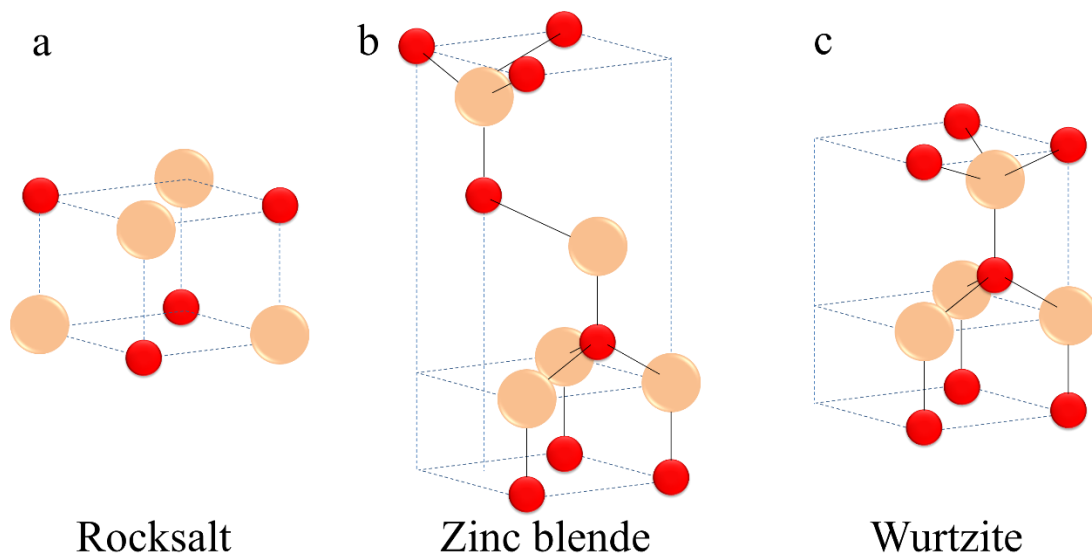


Figure 2.3. The crystal structures of ZnO, the red and the pink solid circles are Zn and O atoms, respectively.

Most of the usage form of ZnO is one dimensional form because of its controllable polarization direction during growth process resulted to lower effect of neighborhood grain. In between 2006-2010, Wang' group developed energy harvesting or scavenging with nanorods of ZnO. Electrode patterns and an alignment of ZnO have been designed and modified in different ways. The results from his research group are that the electrical output has been improved from 6 mV to 1.2V (Wang and Song, 2006; Yang *et al.* 2009; Hu *et al.* 2010 ).

For the last decade, research corporate the advantage of each material to fabricate the harvester to maximize the output power. The development is not limiting to use some of material as a dopant. The development also found as a layer by layer that makes the device can supply the power energy to small power electronic devices.

### 2.3 Constitutive equation for piezoelectric energy harvesting

Piezoelectricity is an electromechanical coupling system. Piezoelectric equation can be derived by application of the thermodynamic law. The finalized

equations can be done by difference pairs of independent parameters and the corresponding free energy that is summarized in the Table 2.1.

Table 2.1 Types of fundamental piezoelectric relation (Ikeda, 1990)

Independent variable	Type	Piezoelectric relation	Form	Thermodynamic function
S,D	Extensive	$T = c^D S - hD$ $E = -hS + \beta^S D$	h-form	Helmholz free energy
T,E	Intensive	$S = s^E T + dE$ $D = dT + \varepsilon^T E$	d-form	Gibbs free energy
T,D	Mixed	$S = s^D T + gD$ $D = -gT + \beta^T D$	g-form	Elastic Gibbs energy
S,E	Mixed	$T = c^E S - eE$ $D = eS + \varepsilon^S E$	e-form	Electric Gibbs energy

The relation between 4 piezoelectric coefficients are

$$d_{nij} = \varepsilon_{nm}^T g_{mij} = e_{nkl} s_{klij}^E \quad (2.1a)$$

$$e_{nij} = \varepsilon_{nm}^S h_{mij} = d_{nkl} c_{klij}^E \quad (2.1b)$$

$$g_{nij} = \beta_{nm}^T d_{mij} = h_{nkl} s_{klij}^D \quad (2.1c)$$

$$h_{nij} = \beta_{nm}^T e_{mij} = g_{nkl} c_{klij}^D \quad (2.1d)$$

In practical, d-form piezoelectric equation is almost used to determine the performance of a material in piezoelectric application. D is preferable for analyses of sound and vibration because the value can be determined via quantity of free charge directly.

The other way to identify performance of the system is determination via coupling coefficient  $k^2$ , ratio between stored mechanical energy and supplied electrical energy or stored electrical energy and supplied mechanical energy. In the case

of piezoelectric the coupling is defined by ratio of the square of interaction coefficient term and product of the principal coefficients term. Recall piezoelectric equations d-form

$$k^2 = \frac{d^2}{\epsilon^T S E} \quad (2.2)$$

Principally, the piezoelectric coefficients are tensor. All of the process is accordingly to tensor algebra. The member of each tensor is depended on the physical properties is used to construct. Mechanical stress is resulted by force tensor and unit vector of the normal area in Cartesian coordinate that is a first range tensor. The size of the stress tensor is  $3 \times 3$ . Piezoelectric is the third range tensor is constructed by a second range tensor and a first range tensor. The member of the tensor is 27. However, the stress and strain tensor are symmetric that the indices can interchange. The tensor notation is turned into simpler matrix expression by index abbreviations as seen in table 2.2

Table 2.2 Matrix notation of symmetric tensors.

ij or kl	p of q
11	1
22	2
33	3
23,32	4
13,31	5
12,21	6

By the notation, the following identifications are made:

$$T_{ij} = T_p \quad (2.2a)$$

$$S_{ij} = S_p, \text{ when } i = j \quad (2.2b)$$

$$2S_{ij} = S_p, \text{ when } i \neq j$$

$$d_{nij} = d_{np} \quad (2.2c)$$

$$c_{klij} = c_{pq} \quad (2.2d)$$

The application of the matrix notation can reduce the member of the tensor, for example, 27 to 18 for piezoelectric tensor and 81 to 36 for elastic compliance and stiffness tensors. Piezoelectric property is related to the crystal structure directly. By application of matrix transformation and symmetry operation, some components of the tensor are disappeared and some of them are found a relation. For the detail of the symmetries in the piezoelectric coupling matrix of all crystal classes can see in “Physical properties of crystals” (Nye, 1957).

## 2.4 Electromechanical coupling properties of fundamental shape

The suitable shape of the material is necessarily optimized. Troiler-Mckinstry and Muralt shown comparison between piezoelectric bulk and thin film (Troiler-Mckinstry and Muralt, 2004). Sensitivity, effective piezoelectric coefficient, of the bulk in thickness mode is dominated by  $d_{33}$  purely. While the sensitivity is dramatically dropped for the thin film. The bending effect becomes significant. Troiler-Mckinstry and Muralt showed equations to express the effective piezoelectric coefficients both parallel and normal directions in terms of bulk coefficients as shown.

$$e_{31,f} = \frac{d_{31}}{s_{11}^E + s_{12}^E} = e_{31} - \frac{c_{13}^E}{c_{33}^E} e_{33} \quad (2.3a)$$

$$d_{33,f} = \frac{e_{33}}{c_{33}^E} = d_{33} - \frac{2s_{13}^E}{s_{11}^E + s_{12}^E} d_{31} \quad (2.3b)$$

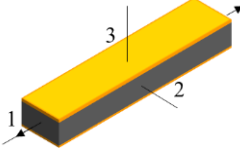

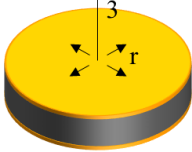
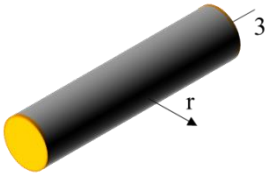
where subscript  $f$  is referred to the coefficient of the film.

Also, the piezoelectric coefficient is confirmed the greater value when the form of the nanostructure is considered (Zhao, *et al* 2004). The piezoelectric coefficient ZnO nanobelt have been characterized via atomic force microscope (AFM) in piezoelectric

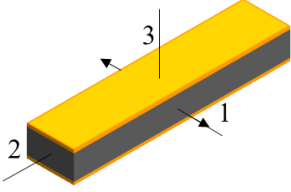
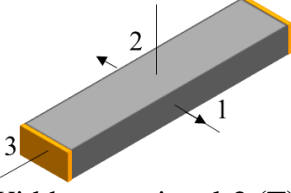
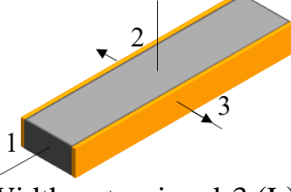
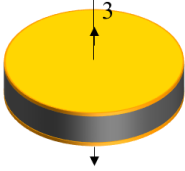
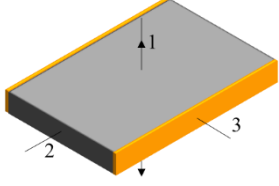
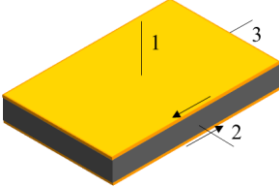
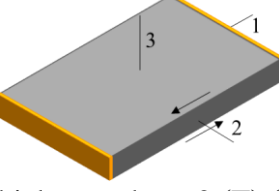
force microscope mode (PFM). The coefficient was greater than the bulk form around 2.5 times that effect from size effect of the material.

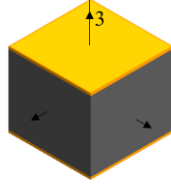
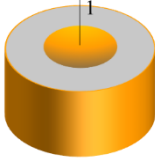
Not only the size and the shape of the piezoelectric material but also the alignment of an electrode on the piezoelectric is effect to the sensitivity of the material. Ikeda (Ikeda 1990) shown simply configuration and its coupling coefficient of each mode that is concluded in table 2.3.

Table 2.3 Electromechanical in various vibration modes of piezoelectric material.

Structure	Conditions		Electromechanical coupling coefficient ( $k^2$ )
	Mechanical	Electrical	
 Length-extensional (T)	$T_2 = 0$ $T_3 = 0$	$\frac{\partial E_3}{\partial x_1} = 0$	$k_{31}^2 = \frac{d_{31}^2}{s_{11}^E \epsilon_{33}^T}$
 Length-extensional (L)	$T_1 = 0$ $T_2 = 0$	$\frac{\partial D_3}{\partial x_1} = 0$	$k_{33}^2 = \frac{d_{33}^2}{s_{33}^E \epsilon_{33}^T}$
 Radial (extensional) (T)	$T_3 = 0$ $(u_\theta = 0)$	$\frac{\partial E_3}{\partial r} = 0$	$k_p^2 = \frac{2}{1 - \sigma} \frac{d_{31}^2}{s_{11}^E \epsilon_{33}^T}$
 Radial-dilatational (T)	$S_3 = 0$	$\frac{\partial E_3}{\partial r} = 0$	$k_p'^2 = \frac{2}{1 - \sigma'} \frac{e_{31}^2}{c_{11}^E \epsilon_{33}^{RT}}$



Structure	Conditions		Electromechanical coupling coefficient ( $k^2$ )
	Mechanica	Electrical	
 Width-extensional-1 (T)	$S_2 = 0$ $T_3 = 0$	$\frac{\partial E_3}{\partial x_1} = 0$	$k_{31}^{\prime 2} = \frac{e_{31}^{\prime 2}}{\tilde{c}^E \epsilon^{\prime WT}}$
 Width-extensional-2 (T)	$T_2 = 0$ $S_3 = 0$	$\frac{\partial E_3}{\partial x_1} = 0$	$k_{31}^{\prime\prime 2} = \frac{e_{31}^{\prime\prime 2}}{\tilde{c}^E \epsilon^{\prime\prime WT}}$
 Width-extensional-3 (L)	$S_1 = 0$ $T_2 = 0$	$\frac{\partial D_3}{\partial x_3} = 0$	$k_{31}^{\prime 2} = \frac{e_{33}^{\prime 2}}{\tilde{c}_{33}^D \epsilon^{\prime\prime WS}}$
 Thickness-extensional-1 (L)( $\perp$ )	$S_1 = 0$ $S_2 = 0$	$\frac{\partial D_3}{\partial x_3} = 0$	$k_t^2 = \frac{e_{33}^2}{c_{33}^D \epsilon_{33}^S}$
 Thickness-extensional-2 (T)( $\parallel$ )	$S_2 = 0$ $S_3 = 0$	$\frac{\partial E_3}{\partial x_1} = 0$	$k_e^2 = \frac{e_{31}^2}{c_{11}^E \epsilon_{33}^S}$
 Thickness-shear-1 (L)( $\perp$ )	$S_4 = 0$	$\frac{\partial D_1}{\partial x_1} = 0$	$k_{15}^2 = \frac{e_{15}^2}{c_{55}^D \epsilon_{11}^S}$
 Thickness-shear-2 (T) ( $\parallel$ )	$S_6 = 0$	$\frac{\partial E_1}{\partial x_1} = 0$	$k_{5e}^2 = \frac{e_{15}^2}{c_{55}^E \epsilon_{11}^S}$

Structure	Conditions		Electromechanical coupling coefficient ( $k^2$ )
	Mechanical	Electrical	
 Hydrostatic			$k_h^2 = \frac{d_h^2}{s_h^E \epsilon_{33}^T}$
 Tube	Thickness-extensional Length-extensional Circular-extensional		$k_t^2$ $k_{31}^2$ $k_{31}^2$
Note: T=transverse effect and L = longitudinal effect $\sigma = -s_{12}^E / s_{11}^E$ $\tilde{c}^E = 1 / s_{11}^E (1 - \sigma^2)$ $\sigma' = c_{12}^E / c_{11}^E, \epsilon_{33}^{RT} = \epsilon_{33}^S / (1 - k_p'^2), \epsilon_{33}^{RT} = \epsilon_{33}^T (1 - k_{31}^2)$ $e_{31}' = e_{31} - e_{33} c_{13}^E / c_{33}^E, \epsilon^{WT} = \epsilon_{33}^T (1 - k_{31}^2)$ $\epsilon_{31}'' = \epsilon_{31} (1 - c_{12}^E / c_{11}^E)$ $\tilde{c}^E = 1 / s_{11}^E (1 - \sigma_1^E \sigma_3^E), \sigma_1^E = -s_{13}^E / s_{33}^E, \sigma_3^E = -s_{13}^E / s_{33}^E$ $e_{33}' = e_{33} - e_{31} c_{31} / c_{11}^E, \tilde{c}_{33}^E = c_{33}^E - (c_{13}^E)^2 / c_{11}^E, \epsilon^{WTS} = \epsilon^{WS} / (1 - k_{33}^{-2})$ $\tilde{c}_{33}^D = 1 / s_{33}^D (1 - \sigma_1^D \sigma_3^D), \sigma_1^D = -s_{13}^D / s_{11}^D, \sigma_3^D = -s_{13}^D / s_{33}^D$ $k_e$ is an expedient coupling coefficient: $k_e^2 = k_e^2 / (1 - k_e^2)$ $k_{5e}$ is an expedient coupling coefficient: $k_{5e}^2 = k_{15}^2 / (1 - k_{15}^2)$ $d_h = 2d_{31} + d_{33}, s_h^E = 2(s_{11}^E + s_{12}^E) + 4s_{13}^E + s_{33}^E$			

The axes of each configuration are referred to material coordinate that the axis 3 is the poling direction. Structural, alignment and electrode pattern affect the sensitivity. Based on commercial PZT5A ([www.efunda.com](http://www.efunda.com), 15/4/2016),  $d_{15}$  is greater than  $d_{31}$  and  $d_{33}$  for 1.56 and 3.40 time, respectively. The material can show the best performance when the configurations thickness-shear-1 (L)( $\perp$ ) is considered.

The coupling coefficient can be used to predict the performance of the structure. However, the coefficient is derived in the static condition, that may not be

enough to describe the system because most of them is operated at the dynamic condition. The frequency response is necessary to consider. In obtain the information, sometimes the equation to describe is quite complicated that is hard to analyst the exact solution. The application of a numerical method is used to full few the problems. Finite element method is a numerical method is almost employed in continuum mechanic. The method is suitable for both static and dynamic system that enables us to optimize the model before implementation.

## 2.4 Piezoelectric energy harvesting method

The model of vibration energy harvesting system was developed by William and Yates in 1996 as shown in figure 2.4.

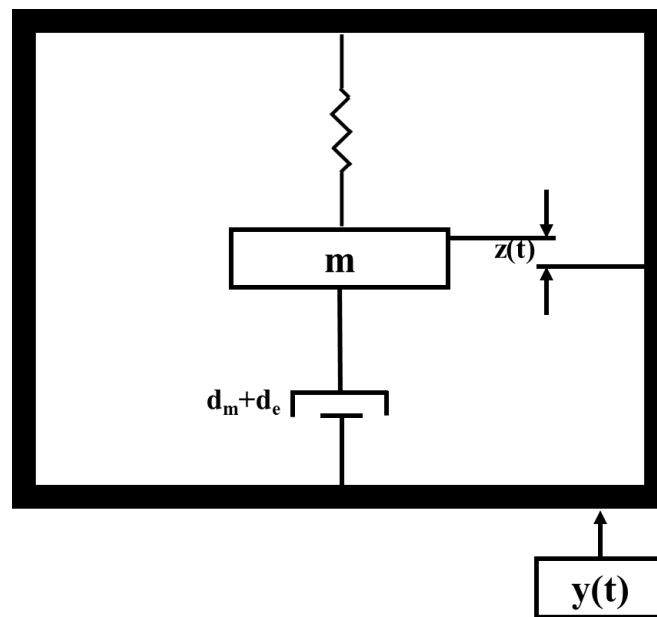


Figure. 2.4. Schematic diagram of the linear and inertial-base generator (edited from Wei and Jing 2017).

The Newtonian equation of the system is described by

$$m\ddot{z}(t) + (d_m + d_e)\dot{z}(t) + kz(t) = -m\ddot{y}(t) \quad (2.4)$$

where  $z(t)$  and  $y(t)$  are the spring deflection and the input displacement, respectively. The parameter  $m$ ,  $k$ ,  $d_m$  and  $d_e$  represent the seismic mass,

the spring constant, the mechanical damping coefficient and the electrical damping coefficient, respectively.

The equation of motion is obtained as following:

$$z(t) = \frac{\omega^2}{\sqrt{\left(\frac{k}{m} - \omega^2\right) + \left(\frac{(d_m + d_e)\omega}{m}\right)^2}} y_0 \sin(\omega t - \varphi) \quad (2.5)$$

where  $\varphi$  is the phase angle that is given by

$$\varphi = \tan^{-1}\left(\frac{d_T \omega}{k - \omega^2 m}\right) \quad (2.6)$$

The maximum energy can be extracted when the excitation energy is equaled to the natural frequency  $\omega_n$  of the spring. The maximum energy is described as following:

$$P_{out} = \frac{m \zeta_e y_0^2 \omega_n^3}{4 \zeta_T^2} \quad (2.7)$$

where  $\zeta_T$  is the total damping ratio that equals to  $d_T/2m\omega_n$

## 2.5 Vibration mode of cantilever

### - Longitudinal mode

The cantilever is portion into a segment with cross-section A and thickness  $dx$ . The segment is assumed to be pulled by a force  $P$  in left end and  $P + \frac{\partial P}{\partial x} dx$  in another one. After summing the force in  $x$ -axis and replace the force P in  $x$ -axis by  $\sigma_x A$ . By the linear elastic theory, the result becomes

$$\frac{\partial(AE \frac{\partial u}{\partial x})}{\partial x} + f = \rho A \frac{\partial^2 u}{\partial t^2} \quad (2.8)$$

where  $u$  is displacement of the beam in  $x$  axis,  $\rho$  is mass density,  $E$  is elastic modulus and  $f$  is applied force.

For the case of free vibration, which is vanishing of the external force, the solution of the equation can be separated into the term that depended on a space and time ( $u(x,t) = \sum cX(x)T(t)$ ). The result of the equation (2.8) thus become

$$u(x,t) = \sum c_{i1} \sin(\alpha_i x - \omega_i t) + c_{i2} \sin(\alpha_i x + \omega_i t) \quad (2.9)$$

$$\omega_i^2 = \frac{E\alpha_i^2}{\rho}, \omega_i l \sqrt{\frac{\rho}{E}} = \frac{(2i-1)\pi}{2} \quad (i = 1, 2, 3, \dots)$$

, where  $\omega_i$  is eigenfrequency of  $i$  th mode.

#### - Transverse mode

The cantilever is forced in  $e_z$ -axis which results to bending deformation from  $e_x$ -axis. The forces that act on the considered segment is shown in figure 2.5 consists of shear force  $V$  and bending moment  $M$ . Amplitude of bending, in this case, is assumed very small resulted to  $ds$  is nearly to  $dx$ .

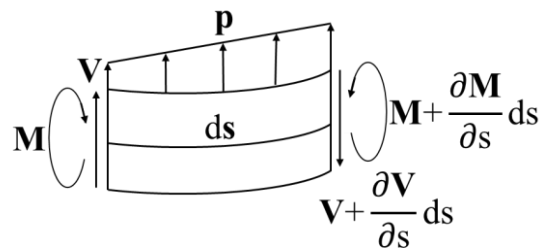


Figure 2.5. Free-body diagram of infinitesimal cantilever in transverse mode.

From the total force and total moment, the equation the state that describe the bending deformation can be shown by

$$\frac{\partial^2}{\partial x^2} \left( EI \frac{\partial^2 w}{\partial x^2} \right) + \rho A \frac{\partial^2 w}{\partial t^2} = p \quad (2.10)$$

Where  $w$  is deformation in  $e_z$ -axis, and  $I$  is the second moment that depending on the cross-section of the cantilever. The equation is also known as classical beam Euler-Bernoulli theory. By separation the solution the same as longitudinal mode ( $w(x,t) = \sum c W(x)T(t)$ ), the obtained general solution is become:

$$\begin{aligned} W(x) &= C_1 \sin ax + C_2 \cos ax + C_3 \sinh ax + C_4 \cosh ax \\ T(t) &= D_1 \sin \omega t + D_2 \cos \omega t \end{aligned} \quad (2.11)$$

By application of cantilever beam boundary conditions, the deformation is determined to be zero at the fixed end. At the free end, there are no shear and moment force. The corresponding eigenfrequency are found:

$$\beta^2 = (\alpha_i l)^2 =, \omega_i l^2 \sqrt{\frac{\rho A}{EI}} \quad (2.12)$$

To make it clearly that nanostructure like nanorod is not suitable for energy harvesting at very low frequency. ZnO nanorod is used as a model in the testing. By helpfull of COMSOL Multiphysics software. Material parameter for is listed in table 2.4. The diameter and length of nanostructure are 1 and 5 $\mu$ m and Modes of vibration ZnO nanorod in each form is in table 2.5 to 2.7.

Table 2.4 Listed of physical properties of ZnO.

Physical property	Value	Reference
Density (Kg/m <sup>3</sup> )	5680	
Dielectric	$\begin{pmatrix} 8.54 & 0 & 0 \\ 0 & 8.54 & 0 \\ 0 & 0 & 10.20 \end{pmatrix}$	
Elastic stiffness (GPa)	$\begin{pmatrix} 209.7 & 121.1 & 105.1 & 0 & 0 & 0 \\ 121.1 & 209.7 & 105.1 & 0 & 0 & 0 \\ 105.1 & 105.1 & 210.9 & 0 & 0 & 0 \\ 0 & 0 & 0 & 42.47 & 0 & 0 \\ 0 & 0 & 0 & 0 & 42.47 & 0 \\ 0 & 0 & 0 & 0 & 0 & 44.29 \end{pmatrix}$	(Bateman 1962)
Piezoelectric coefficient e (C/m <sup>2</sup> )	$\begin{pmatrix} 0 & 0 & 0 & 0 & -0.450 \\ 0 & 0 & 0 & -0.45 & 0 & 0 \\ -0.51 & -0.51 & 1.22 & 0 & 0 & 0 \end{pmatrix}$	(Carlotti et al. 1987)

Rigid modes (translation and rotation) were only found in the first two modes of the free-standing rod. The characteristic frequency and the mode of vibration next to the rigid mode of the freestanding rod were similar to the bar configuration. Transverse modes shape of the freestanding and the bar were started with a haft wavelength while the cantilever was started with a one forth wavelength. Each of the transverse modes shape of the three configurations was separated by  $\pi$ . The cantilever-like shown lowest eigenfrequency in vibration modes.

Corresponding induced voltage via piezoelectric effect was shown in table 2.6. Distribution of electric field was according to deformation at each eigenfrequency. The high compressive regime affected high positive induced voltage and vice versa.

Longitudinal mode, deforming gradient and the induced voltage was parallel to the natural axis of the rod. The distribution was symmetry. When an external load is connected to the two ends of the rod, the charge driven was not occurred due to equality of the electric field, the driven force only occurred within the material. In

realistic, when the piezoelectric material is forced, the temporary charge occurred due to the imbalance between the electric field at the two surfaces of the material. Adding ground to the boundary condition resulted imbalance of the electric field.

In the case of cantilever beam like bending, distribution of electric at the constraining surface is occurred. The deformation of the transverse mode of the cantilever is occurred perpendicular to the natural axis of the rod. In this case, there is one plane that isn't deformed. If the natural axis was set as a z-axis and the displacement was occurred in the positive value of x- axis, the regime over the plane would be pressed and the below one would be extruded. The effect resulted to gradient distribution of induced at the xy-plane.



Table 2.5 The first six mode of vibration for hexagonal rod with different boundaries.

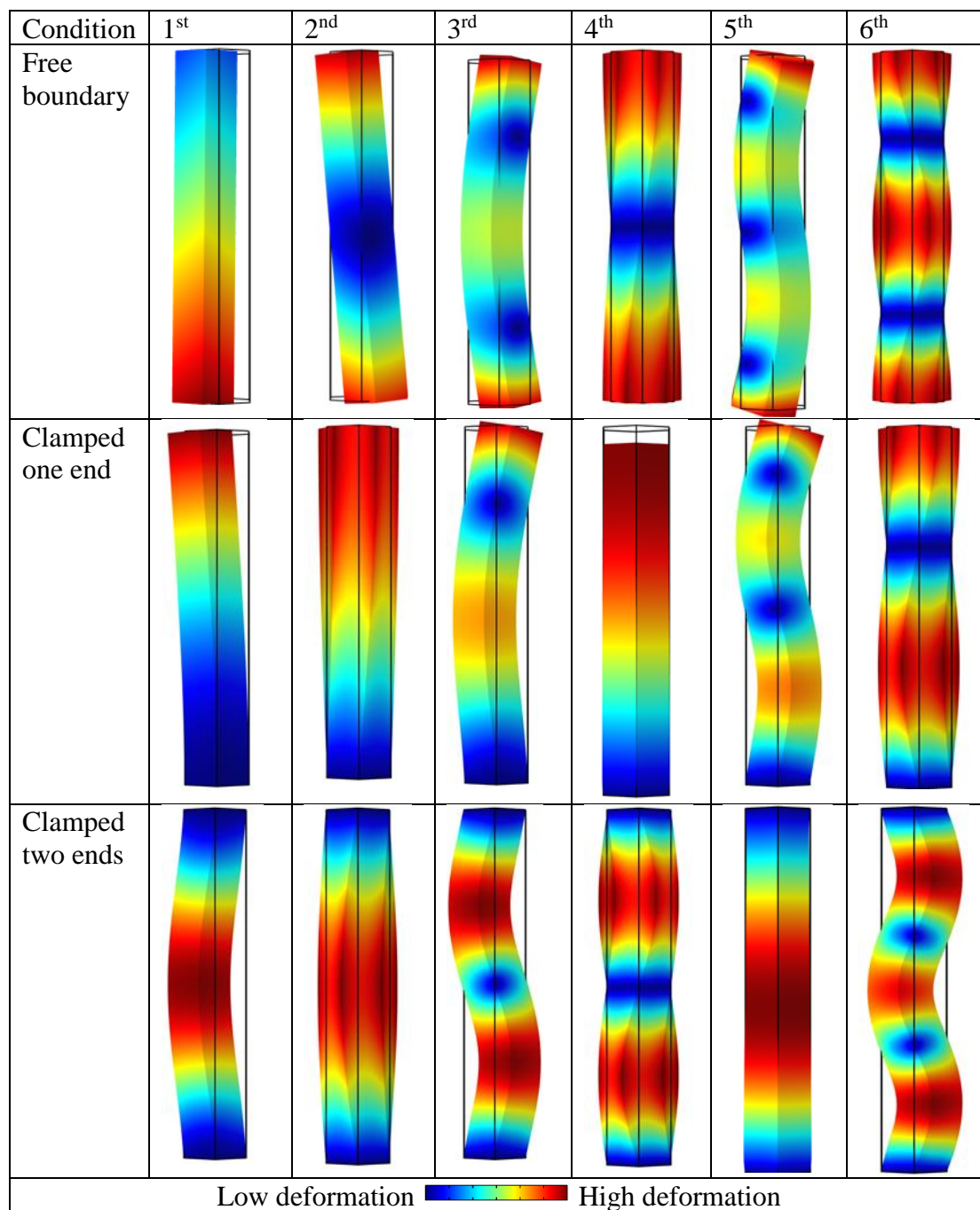


Table 2.6 Corresponding voltage according to deformation at characteristic frequency for hexagonal rod with different boundaries.

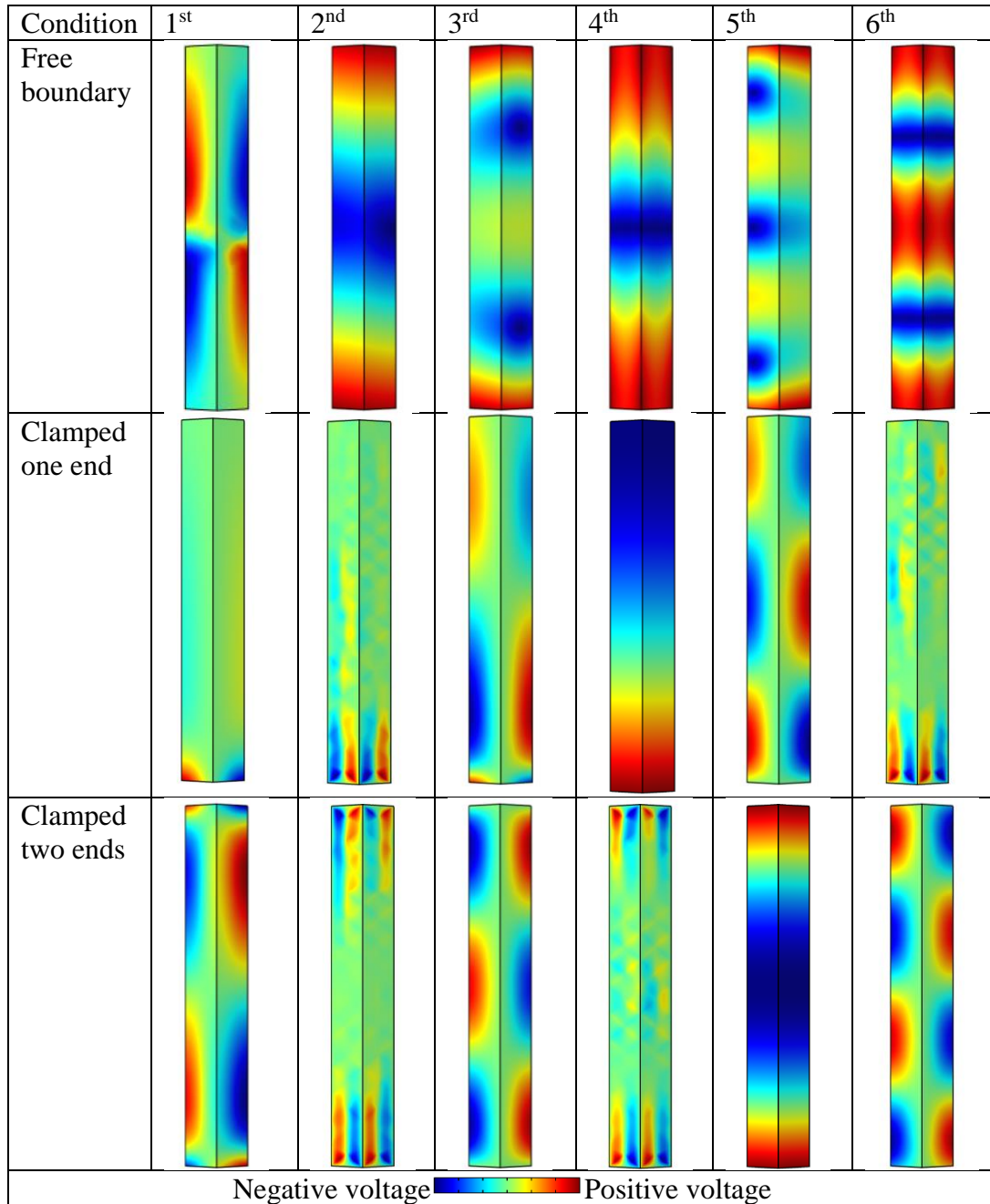


Table 2.7 Eigen frequency for hexagonal rod with different boundaries.

Condition	1 <sup>st</sup> (MHZ)	2 <sup>nd</sup> (MHZ)	3 <sup>rd</sup> (MHZ)	4 <sup>th</sup> (MHZ)	5 <sup>th</sup> (MHZ)	6 <sup>th</sup> (MHZ)
Free boundary	0	0	75.41	134.31	186.27	269.96
Clamped one end	12.87	67.27	72.17	127.26	177.97	201.86
Clamped two ends	72.019	134.74	170.15	269.46	275.62	289.35

Definition between the cantilever beam and rod is in their displacement characteristics. The beam showed only transverse mode and the rod undergo either longitudinal or torsional (Leissa and Qatu, 2011). In our calculation, the longitudinal and torsional occurred both the rod and the beam but the sequence of the mode was different. In case of the hexagonal prism with 10  $\mu\text{m}$  length, the torsional and longitudinal modes were found at the third and the fifth modes, respectively, while the hexagonal prism with 100  $\mu\text{m}$  length were found at the fifth and the eighth modes.

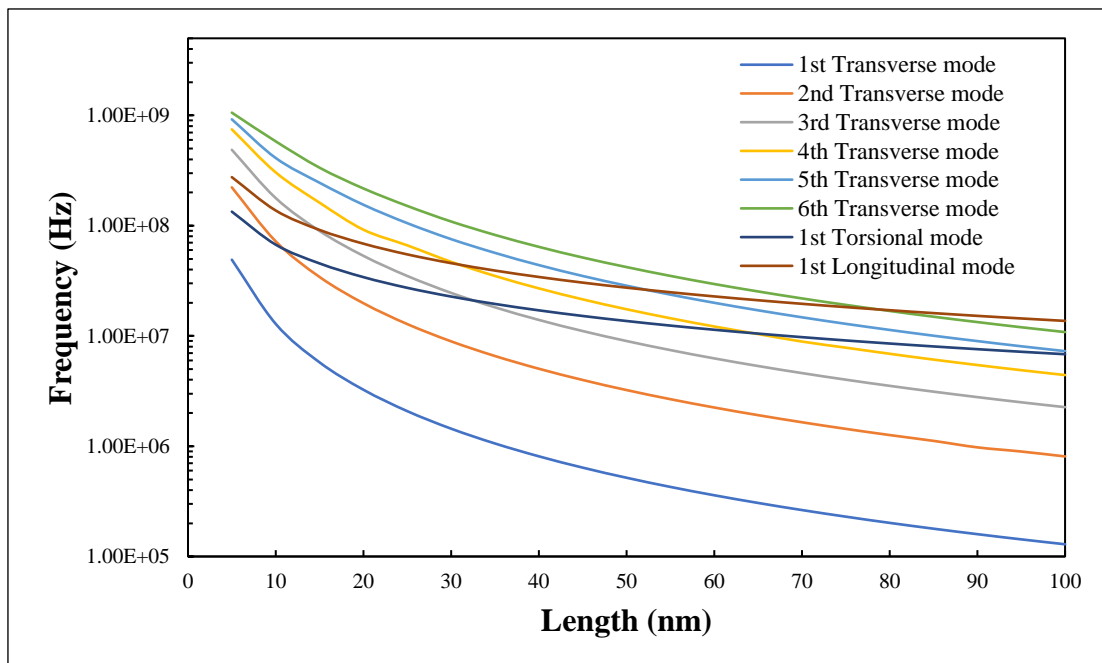


Figure 2.6. The Relation between frequency of each modes of vibration of ZnO cantilever like with changed length.

From the results, the resonance frequency of nanorod is in the range of MHz that is higher than the scale of natural and manmade vibration. To use the nanoparticle in the energy harvesting field, the suitable structure should be considered.

## **2.6 Conclusions**

Development of energy harvesting has been starting since the conventional method to change many kinds of energy to electrical was discovered. The main of each technique is maximized the efficiency to converse the energy. The piezoelectric method is using the physical property of the piezoelectric to change the form of mechanical energy to electrical energy. Maximization of the efficiency is involved in material processing directly. The operation is started from the process of synthesis to produce the material with singularity spontaneous polarization and minimized crystal defect. The shape and the electrical contact are a one of the factors is consider because of the anisotropic property of piezoelectricity. By application of the numerical method and high performance of computer which can be used to analyze to observe the performance and suitability of the piezoelectric material to match with a targeted system.

## CHAPTER 3

### SYNTHESIS OF ZNO NANOSTRUCTURE AND SURFACE MODIFICATION

Previously, mechanical and electromechanical coupling of ZnO in one-dimension have been discussed. The efficiency of the material can be tuned by the material processing. This chapter, the fabrication of ZnO and its surface modification are the main objectives. All of fabrication techniques and surface modifications of ZnO nanostructures will be described.

#### 3.1 Introduction

ZnO one-dimensional, nanorod and nanowire, can be fabricated by several methods such as vapor deposition (VLS), metalorganic chemical vapor deposition (MOCVD), and chemical route.

VLS method is the first discussed by Wagner and Ellis during the 1960s (Wagner and Ellis, 1964). Controllable of the aspect ratio of ZnO nanorods and vertical alignment of the nanorods are advantages of the method. The method is started with the dissolution of gaseous reactants into nanosized liquid droplets of a catalyst metal, followed by nucleation and growth of single crystalline rods and then wires. Three are important four factors for the method: the crystal matching between ZnO and substrate, the distance between a substrate and the reactants, the temperature and the gas flow rate (Cao, 2004).

Crystal orientation of ZnO is determined by a substrate. The c-plane sapphire substrate is frequently used because the crystal mismatch between ZnO and the substrate is less than 0.08% at room temperature (Hamada *et al.*, 2009). Silicon (Si) is a one of candidate, however the lattice mismatching between ZnO and Si made the prepared ZnO growth in random orientation (Lee *et al.*, 2003, Jeong and Lee, 2010). The positions and the size of ZnO nanorod are controlled by the size of the metal catalyst. The metal catalyst is normally evaporated on the substrate and then heated at the

eutectic temperature, the melting temperature of alloy, to form alloy droplets. The quantity of the droplet and the diameter of the droplet affect the density and the diameter of the ZnO nanorod, respectively. Gold (Ag) is frequently used in the field because the eutectic temperature of alloy Ag/Si is low around 370°C (Nakashima *et al.*, 1975). The position the droplet was controlled by the lithographical techniques. The diameter of ZnO nanorod is determined by the thickness of the gold thin film. If the thickness of the thin film is decreased, the diameter of nanorods was reduced (Yang *et al.*, 2002).

MOCVD is a chemical vapor deposition method of epitaxial growth of materials, especially compound semiconductors. The principle of operation is the transportation of precursor molecules via a gas carrier into a heated substrate or surface chemical reactor. The advantages of the MOCVD over the VLS is the lower operating temperature and the independent of metal catalyst (Huang *et al.*, 2001). Well-aligned ZnO nanowires was perfectly growth on Si substrate by the method (Zeng *et al.* 2005).

Synthesized ZnO nanorod via chemical route bases on precipitating of zinc and alkaline soft. Precursors, solvents, stabilizing agents, temperature, and reaction time affect the size and the shape of prepared nanostructures. In 2003, Liu *et al.* used  $\text{Zn}(\text{NO}_3)_2 \cdot 6\text{H}_2\text{O}$  as a precursor and NaOH as a precipitating agent. After that, the solution was loaded into the autoclave, nanorods with 45.6 nm of diameter and 1.54  $\mu\text{m}$  of length were obtained. In 2005, Wu *et al.* used  $\text{ZnCl}_2$  as a precursor and controlled the pH of the solution with an addition of the  $\text{NH}_3$ . The obtained samples are 60-100 nm in diameter and 500-600 nm in length. The hexagonal structure was synthesized by using 4 mM  $\text{Zn}(\text{CH}_3\text{COO})_2 \cdot 2\text{H}_2\text{O}$  and 20 mM NaOH as precursors. The flower like structure was obtained after stirred at 75 °C for 30 min (Kumra *et al.* 2013). Branch rod-like obtained from 0.2 M  $\text{Zn}(\text{CH}_3\text{COO})_2 \cdot 2\text{H}_2\text{O}$  and 1.6 M NaOH at 70 °C for 3 h (Suwanboon *et al.* 2010). Changing of NaOH to hexamethylenetetramine (HMTA) affected the shape of the ZnO from branch rod-like to columnar hexagonal (Suwanboon *et al.* 2010).

Even though the VLS and MOCVD methods successfully fabricate ZnO one-dimension. The operating temperature is limited the fabrication only on the high melting temperature substrates. Chemical route bases on coprecipitation of cation and anion solution becomes the main method for energy harvesting application. This technique can be prepared not only free-standing nanostructures but also nanorods

vertical aligned on the flexible substrates (Zhou *et al.*, 2010) because the operating temperature by the method is around melting temperature of the water. This chapter, growth mechanism, preparation of ZnO nanorods, and surface modification by chemical route will be discuss.

### 3.2 Theory of crystal growth and surface interaction

#### 3.2.1 Nucleation

Nucleation is the rearrangement of atoms or molecules as a cluster or nucleus, that can growth irreversibly to a macroscopically larger size. The process can be either homogeneous or heterogeneous depended upon residual foreign particles in the solution.

##### - Supersaturation

Nucleation and growth processes to form as the macroscopic particles need the driving force to drive the processes. The supersaturation state is required. The situation is defined by the different of chemical potential of a molecule in the solution and that in the bulk of crystal phase. From thermodynamic of the chemical potential,

$$\Delta\mu = kT \ln S \quad (3.1)$$

where  $k$  is the Boltzmann constant,  $T$  is the absolute temperature, and  $S$  is the supersaturation ratio that is a ratio between actual and equilibrium activities of molecules in the crystal. The situation is said to be supersaturation if the difference is positive. In the opposite, the dissolution case takes place when the difference is negative.

##### - Gibbs free for the nucleation process

Assuming, the shape of the interesting nucleus is a spherical shape. The work necessary to form the cluster of molecules is the difference between the free energy of its final and initial state and the spend energy for the interface between nucleus. The Gibbs free for the nucleation process is shown as following:

$$\Delta G_T = -\frac{4}{3}\pi \frac{r^3}{V} \Delta\mu + 4\pi r^2 \sigma \quad (3.2)$$

where  $\sigma$  is the surface free energy. By derivative operation with respect to cluster radius and replacing the difference of chemical potential of equation 3.1, the critical radius or nucleus size thus becomes:

$$r^* = \frac{2\sigma V}{kT \ln S} \quad (3.3)$$

The equation 3.3 shows the relation between the nucleus size and the supersaturation state.

### 3.2.2 Crystal growth

Growth mechanism is the second state of nanoparticle forming that occurs when the atom or molecule concentration falls below the critical supersaturation level. At the beginning of this state, the system is dominated by very small particles that the state is not in thermodynamic equilibrium. The smaller particles are dissolved as a source for growth of bigger particles that is the key for growth of nanocrystals. The particles is grown by the sequence of atoms or molecules diffusion towards the surface followed by reaction of the atoms or molecules at the surface of the nanocrystal. Coarsening effects, controlled either by mass transport or diffusion, are often termed the Ostwald ripening process, was announced in 1900 (Ostwald 1901). This diffusion limited Ostwald ripening process is the most predominant growth mechanism and was first determined by Lifshitz and Slyozov, followed by a related work by Wagner, known as the LSW theory (Lifshitz and Slyozov 1959; Lifshitz and Slyozov 1961; Wagner 1961).

Assuming the average radius of particles is  $r$ . the bulk liquid phase is considered to be supersaturated with atoms or molecules concentration  $c_b$ , the concentration at particle interface is  $c_i$ , and the solubility of the particle is  $c_r$ . the flux of atoms or molecules passing through a spherical surface with radius  $x$  (with respect to the center of the spherical) within the diffusion layer is given by Fick's first law:



$$J = 4\pi x^2 D \frac{dC}{dx} \quad (3.4)$$

By integration over space, assuming that  $\frac{dr}{dt} = \frac{JV_m}{4\pi r^2}$ , and using the Gibbs-Thompson equation the equation thus become:

$$\frac{dr}{dt} = \frac{2\sigma V_m^2 c_\infty}{RT \left( \frac{1}{D} + \frac{1}{k_d r} \right)} \frac{\left( \frac{1}{r_b} - \frac{1}{r} \right)}{r} \quad (3.5)$$

where  $\sigma$  is interfacial energy,  $c_\infty$  is the concentration of a flat particle,  $V_m$  is the molar volume,  $R$  is the universal gas constant,  $\delta$  is the thickness of the diffusion layer,  $k_d$  is the rate constant of a simple first order deposition reaction, and  $D$  is the diffusion coefficient.

By the diffusion limited, was determined by LSW theory, the diffusion is the slowest in the growth characterized ( $D \ll k_d r$ ) and the ratio  $r/r_b$  is constant. The integration of equation 3.5 can be reshown as a form:

$$r^3 - r_0^3 = Kt$$

$$K = \frac{8\sigma D V_m^2 c_\infty}{9RT} \quad (3.6)$$

where  $r_0$  is the average radius of the particle at the starting time or another word nuclei radius. The equation 3.6 is extensively used to describe growth mechanism of the nanoparticle, However, the equation is used just for spherical particles in supersaturate medium and the processes of nucleation is assumed to be finished before starting the growth mechanism process and the effect of aggregation is negligible.

### 3.2.3 Orientated Attachment

In 1998, Penn and Banfield discovered an important crystal growth mechanism named “oriented attachment” (OA). OA is extensively used to describe 1-d nanoparticle almost (Penn and Banfield 1998). Mechanism of OA is attachment of two domains at least. When attachment is occurred, the domains tent to reoriented itself

to match with each other resulted to the irregular shape. The conclusion of the mechanism is shown in figure 3.1.

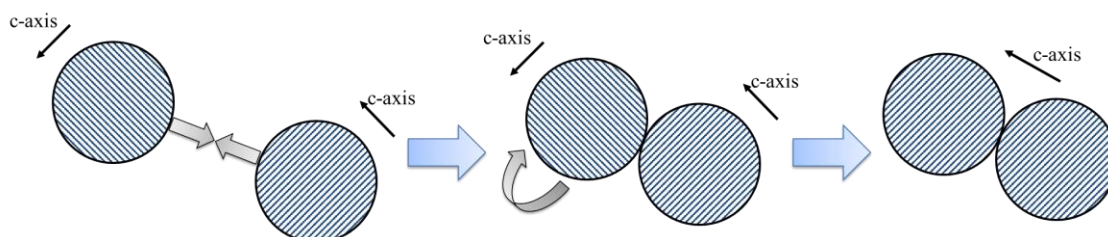


Figure 3.1. The sketch of mechanism process of OA.

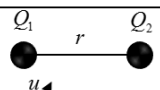
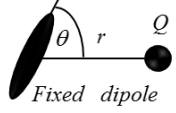
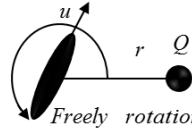
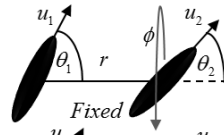
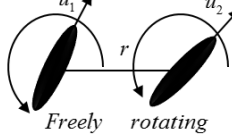
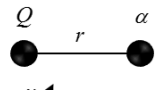
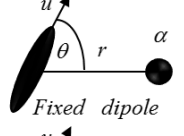
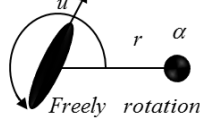
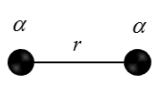
#### 3.2.4 Surface interaction between ZnO and ions molecule

Surface modification is a process to add some functional or to match the nanoparticle to the target application environment. The process is found in many applications, for example, drug transfer, surface wetting control, colloid stability, etc. The main criteria must be considered for the process is the interaction between nanoparticle surface and interested atoms or molecules. The interaction can be either quantum initial for example covalent bond, or electrostatic initial. Each interaction has different range of the force field. Covalent bonding is sharing of orbitals of different atom, the force field in this case is very short range. The length of bonding is very short, in scale of angstrom. Interaction between fixed charges on a particle with ions in a media can be consider as an electrostatic force of points charge. The energy interaction is depended on reverse of the distance between the charges. When compared with the covalent force, the length of the force is longer, but the strength of the interaction is lower.

The dipole moment can interaction either ionized atom of the polar molecule, but the strength of the interaction is different, invert of the distant square and cubic respectively that shorter range than charge-charge interaction. Van der wal force is another one of interaction can occur at the surface. But the strength of the force is

quietly small magnitude when compared with above. The conclusion of the interaction force field is in the table 3.1.

Table 3.1 Conclusion of pair interaction of atoms, or molecules (Isaelachvili, 1984).

Type of interaction	Interaction energy
Charge-Charge	 $+ \frac{Q_1 Q_2}{4\pi\epsilon_0 r}$
Charge-dipole	 $- \frac{Qu \cos \theta}{4\pi\epsilon_0 r^2}$
	 $- \frac{Q^2 u^2}{6(4\pi\epsilon_0)^2 kTr^4}$
Dipole-dipole	 $- \frac{u_1 u_2 [2 \cos \theta_1 \cos \theta_2 - \sin \theta_1 \sin \theta_2 \cos \phi]}{4\pi\epsilon_0 r^3}$
	 $- \frac{u_1^2 u_2^2}{3(4\pi\epsilon_0)^2 kTr^6}$
Charge-nonpolar	 $- \frac{Q^2 \alpha}{2(4\pi\epsilon_0)^2 r^4}$
Dipole-non-polar	 $- \frac{u^2 \alpha (1 + 3 \cos^2 \theta)}{2(4\pi\epsilon_0)^2 r^6}$
	 $- \frac{u^2 \alpha}{(4\pi\epsilon_0)^2 r^6}$
Two nonpolar molecule	 $- \frac{3}{4} \frac{h\nu\alpha^2}{(4\pi\epsilon_0)^2 r^6}$

ZnO the permanent polarization that is initially from Zn and O. The surface of ZnO is shared by several functional groups when immersed in media for example water. The surface can be either positive or negative form depended upon the pH value of the media as shown in the figure 3.1. The positive zone of the surface of ZnO is covered the range of pH 6 to 8. This regime, the surface is dominated by

$\text{Zn(OH)}^+$ . At the pH 10, the surface is formed a neutral form resulted to isolation point. At the zone of high, the media is rich with the hydroxyl group resulted to the combination of the group to the surface affect the negative charge is formed.

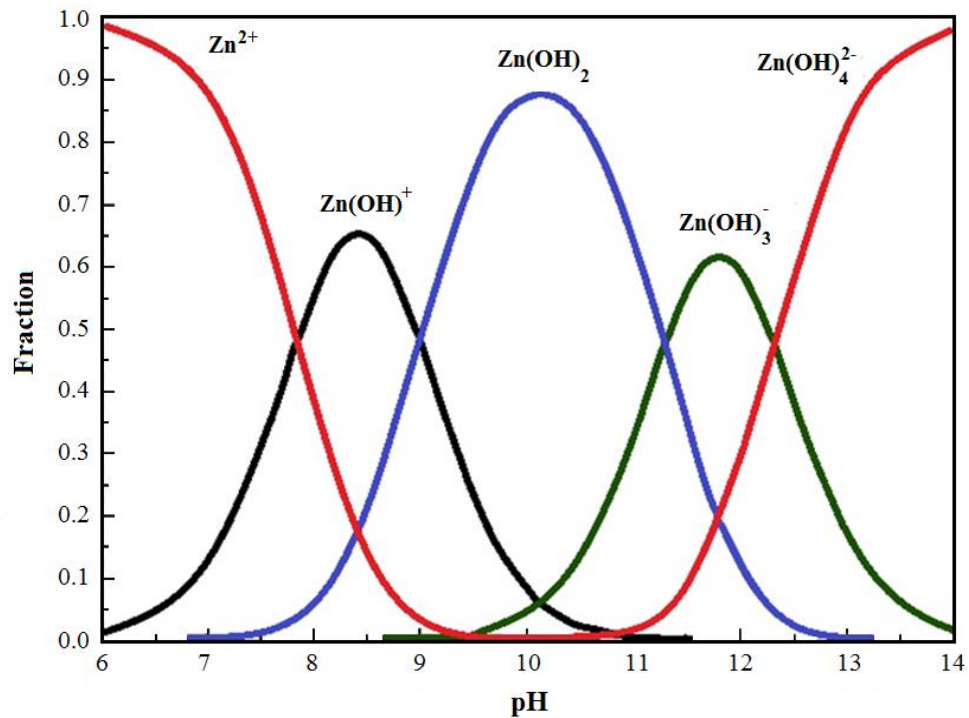


Figure 3.2. The relation between pH value and surface functional groups of ZnO (modified form Degen and Kosec, 2000).

The appearance of the surface of the ZnO nanoparticle when it is immersed in water affect the adsorption of counterion ions to the surface via electrostatic coulomb's force, the regime so-called Stern or Helmholtz layer. The layer locates next to the Stern layer is a diffusion layer or an electric double layer. The co-ions can interact with the Stern layer but the interaction is not strong, ions are not bound. This layer can be used to determine the surface charge which the method to measure is discussion next.

The particles or molecules can be used to interact with the surface of ZnO can be either electrolyte or polar molecule. However, to make the interaction

strength, it would be better to choose the charged particle or molecules because the force field of ion-ion is stronger than ion-dipole.

### 3.3 Materials and Methods

#### 3.3.1 ZnO bush microrods fabrication

ZnO was synthesized accordingly Suwanboon method (Suwanboon *et.al.*, 2010).  $\text{Zn}(\text{CH}_3\text{COO})_2 \cdot 2\text{H}_2\text{O}$  (Sigma Aldrich) and NaOH (Merck) were used as precursors and CTAB (Sigma Aldrich) was used as a stabilizer. The step of preparation was started with mixed the dissolve NaOH in deionizing water (DI water) with CTAB powder. Next step, the dissolved  $\text{Zn}(\text{CH}_3\text{COO})_2 \cdot 2\text{H}_2\text{O}$  was slowly added into the first solution and then continuously stirred at 70 °C for several hours. After that, the solution was cooled at room temperature and filtered by the filter paper No. 42 (Whatman). The obtained white powder was rinsed several times by DI water and ethanol, respectively. The powder was contained in an alumina crucible and calcined at 600 °C in a furnace for 1 h in order to remove any organic residual.

#### 3.3.2 ZnO nanorod fabrication

ZnO was reduced the size into the nanoscale by changing the solvent form DI water to alcohol. The precursors the same as the ZnO bush microrods were dissolved in alcohol and mixed at 60°C. The reaction was kept over than 3 h to make sure that nanorods were formed. After that, the obtained solution was cooled at room temperature and let the precipitate set down to the bottom of the solution and rinsed the precipitate several times by alcohol.

#### 3.3.3 ZnO vertical aligned nanorod fabrication

Fabrication of vertical aligned ZnO nanorods on a substrate was adapted from Green *et al.* method (Green *et al.* 2003). Quasi-colloid nanoparticles ZnO ~5 nm were prepared by mixing of  $\text{Zn}(\text{CH}_3\text{COO})_2 \cdot 2\text{H}_2\text{O}$  and KOH in methanol at 60°C for 2 h. The solution was spun on the cleaned substrate by calibrated home make spin-coater. The coated substrate was annealed at 400°C to get the homogeneous film. After that, the substrate was immersed in the mixture of  $\text{Zn}(\text{NO}_3)_2 \cdot 6\text{H}_2\text{O}$  (Sigma Aldrich) and

hexamethylenetetramine, HMTA (Sigma Aldrich) in DI water at 90°C for several times. The obtained film was rinsed and ultrasonic to clean the residual particle.

### 3.3.4 ZnO microrod fabrication

The process of synthesized ZnO microrod was adapted from ZnO vertical aligned nanorod fabrication. The difference was the nanoparticle were dropped in the growth solution directly.

### 3.3.5 Coating ZnO nanorods by polyelectrolyte

Polyelectrolytes polydiallyldimethylammonium chloride ( PDDA) (100,000-200,000 Mw, Sigma Aldrich) and poly(styrenesulfonate) (PSS)(70,000 Mw, Sigma Aldrich) were used as a polycationic and polyanionic, The chemical structure of each polyelectrolytes is shown in figure 3.3.

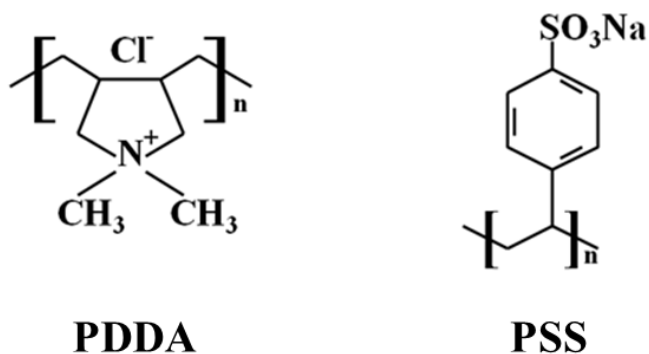


Figure 3.3 Molecular structures of polyelectrolytes PDDA and PSS.

The pH of ZnO quasi-colloidal was adjusted to 10.5 pH to maximize surface charge which covered with Zn(OH)<sup>3-</sup> specie. The solution was mixed with PDDA solution with ratio 1: 1 and kept at room temperature for 2 h. The mixture was centrifuged to get coated ZnO and immersed again in deionizing solution. PSS was coated to the coated PDDA ZnO by the same process.

### 3.3.6 Characterization

The crystal structure and texture of the nanostructures were examined by X-ray diffraction (XRD) technique (Philips X-Pert diffractometer, monochromatic Cu K $\alpha$ ). The patterns were recorded at a scan rate of 3° per min from 20° to 60° for phase and texture analyses.

Scanning electron microscope (SEM) was performed using an SEM5800 instrument (JEOL Ltd., Japan) for micro-texture investigation. The samples were prepared for the observation by application of gold plasma sputtering (SPIsupply, USA). The conductive layer was done at 0.1 mbar under N<sub>2</sub> atmosphere with driven current 10 mA for 2 min. Transmission electron microscope (TEM) JEOL JEM-2010 (JEOL Ltd., Japan) was employed for nano-investigation. The formvar-coated copper grid was used as a substrate for the observation

The surface roughness was characterized by atomic force microscope (AFM) Nanosurf easyscan2 (Nanosurf, Switzerland). The aluminum-coated stiff silicon cantilever (190 kHz ACL-A, AppNano, USA) was performed the surface scanning. Lambda 35 (Perkin Elmer, UK) was used to perform the absorption spectrum from the tested solution. A quartz cuvette was using as a solution containing for ultraviolet range observation.

Zeta potential (ZetaPALS, Brookhaven, USA) was used to determine the charges at the particles or molecules and can be used to predict the stability of the colloid state. The conventional instrument for measuring the potential based on the application of electrophoresis motion and laser dropper velocimetry (LDV). The solution was loaded into a 12.5 x 12.5 mm cross-section plastic cuvette with AQ 792 electrode.

### 3.4 Results and discussion

#### 3.4.1 ZnO crystal growth

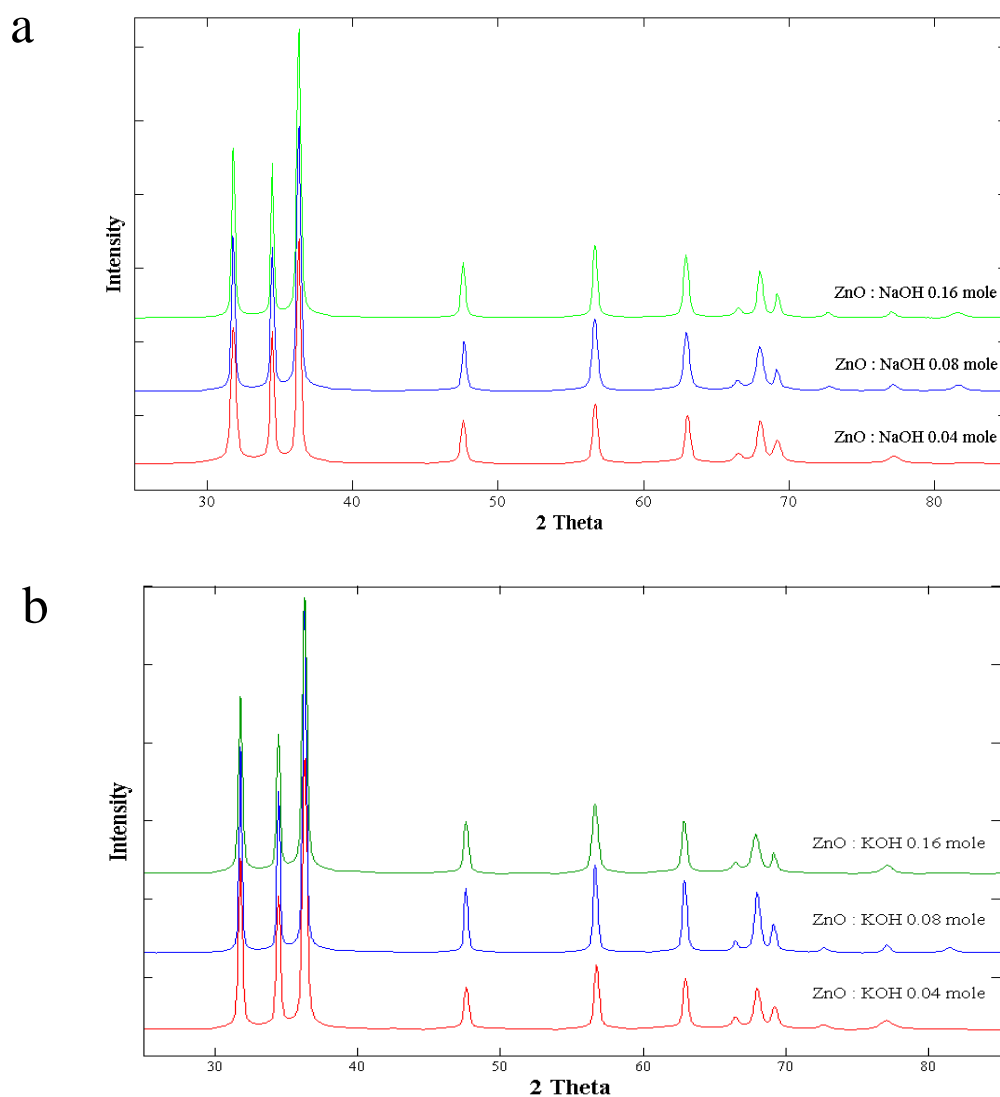


Figure 3.4 The XRD pattern of ZnO prepared by using 0.02 mole  $\text{Zn}(\text{CH}_3\text{COO})_2 \cdot 2\text{H}_2\text{O}$  with a) NaOH and b) KOH at 0.04, 0.08 and 0.16 mole.

The effect of alkaline salt was evaluated by using XRD that was shown in figure 3.4. ZnO prepared from both NaOH and KOH shown XRD peak at 31.82, 34.54, 36.42, 47.59, 56.71, 62.92, 66.47, 68.10, and 69.22 that were related to the (100), (002), (101), (102), (110), (103), (200), (112), and (201) ZnO crystalline planes. However, the ratio of the intensity at the (100) and (002) peaks was different as shown



in the table 3.2. Higher value indicated wurtzite structure while the low value meant the mixing of wurtzite and zinc blend structure. The ratio was nearly to 1 for NaOH at low concentration. The increasing of NaOH concentration to 0.16 M affected the increasing of the ratio to 1.12. However, the ratio was constant at 1.30 for ZnO prepared by using KOH. This because the size of the Na ion is lower than O atom that resulted the penetration of Na ion into the crystal. This effect could not be occurred in the case of K ion because the size is bigger. From the reason, KOH was preferred for ZnO fabrication (Deminets *et al.* 2002).

Table 3.2. The ratio of the maximum intensity at plane (100) by (002) in each condition.

Concentration	0.04M	0.08M	0.16M
NaOH ((100)/(002))	1.0459	1.0901	1.1162
KOH((100)/(002))	1.3066	1.3039	1.3002

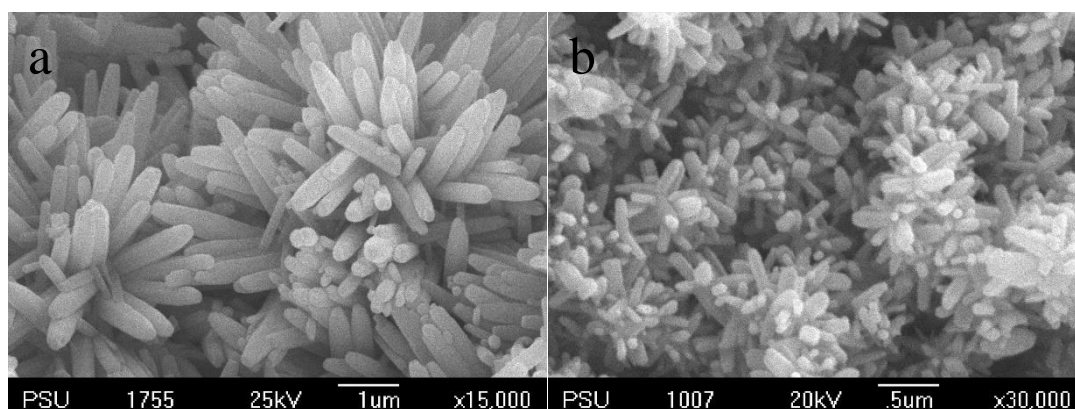
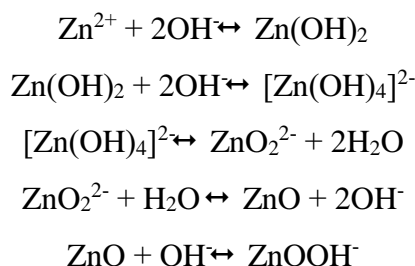


Figure 3.5 SEM images of ZnO a) without CTAB b) with CTAB.

Figure 3.5 shown ZnO branch rods prepared by using  $\text{Zn}(\text{CH}_3\text{COO})_2 \cdot 2\text{H}_2\text{O}$  and KOH with. Figure 3.5a shown ZnO branch rods with average diameter  $305 \pm 41$  nm. The formation of ZnO in one-dimension form by this technique was occurred at strong basic solution as following:



After this process, nuclides were obtained. For the growth step, each plane have different growth rate. (000 $\bar{1}$ ) plane had the lowest growth rate that result to the longest time to reach the equilibrium condition that resulted to the growth of ZnO in c-axis. The growth rate of each plane can be tuned by application of stabilizer. CTAB is cationic that is in a form CTA<sup>+</sup> when immerses in water. The cationic is adsorbed by ZnO nuclei. The surface is then dominated by the negative species. The decreasing of the surface energy resulted to decrease the driving force for particle (Suwanboon, et.al. 2010). Figure 3.5b SEM image of ZnO with application of CTAB. The diameter and the length of the branch rods was dramatically reduced to 65% from the condition without CTAB.

The physical property of the solvent was affected the rate of formation. This phenomenon was observed study kinetic growth rate of ZnO in different kind of alcohol (Sultana *et.al.*2008). The growth rate was very low in the case of low carbon backbone and the rate was increased by using high carbon backbone alcohol.

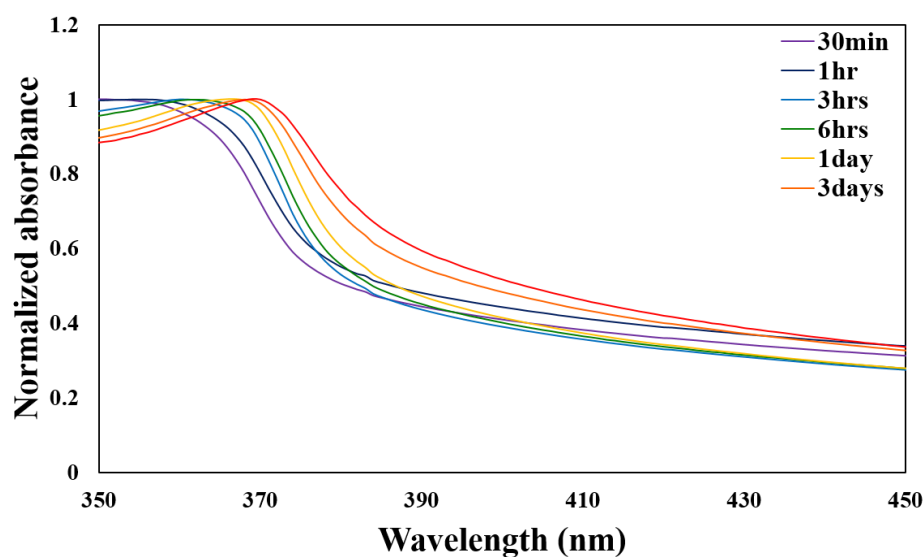


Figure 3.7 Absorption spectra during growth process of the ZnO prepared by using  $\text{Zn}(\text{CH}_3\text{COO})_2 \cdot 2\text{H}_2\text{O}$  and KOH as precursors in methanol solution.

The growth mechanism in alcohol was observed by monitoring the absorption spectra as shown in figure 3.7. The red shift was found when the interaction time was increased, particularly at the first 3 h. This indicated that the size of ZnO was expanded corresponding to the increasing of reaction time. This phenomenon was described as following equation:

$$eE^* = eE_g^{bulk} + \frac{h^2}{8r^2} \left( \frac{1}{m_e^* m_0} + \frac{1}{m_h^* m_0} \right) - \frac{1.8e^2}{4\pi\epsilon\epsilon_0} - \frac{0.124e^4}{h^2 (2\epsilon\epsilon_0)^2} \left( \frac{1}{m_e^* m_0} + \frac{1}{m_h^* m_0} \right)^{-1} \quad 3.9$$

where the first term on the right-hand side represents for an energy gap in bulk form while the second term is a quantum energy of localization, increasing as  $r^{-2}$  for both electron and hole. The third and fourth terms are the Coulomb attraction and the solvation energy loss. The effective energy bandgap is sensitively to the particle radius in nanoscale. However, the energy band gap become the energy gap in the bulk form when the radius is higher than 20 nm.

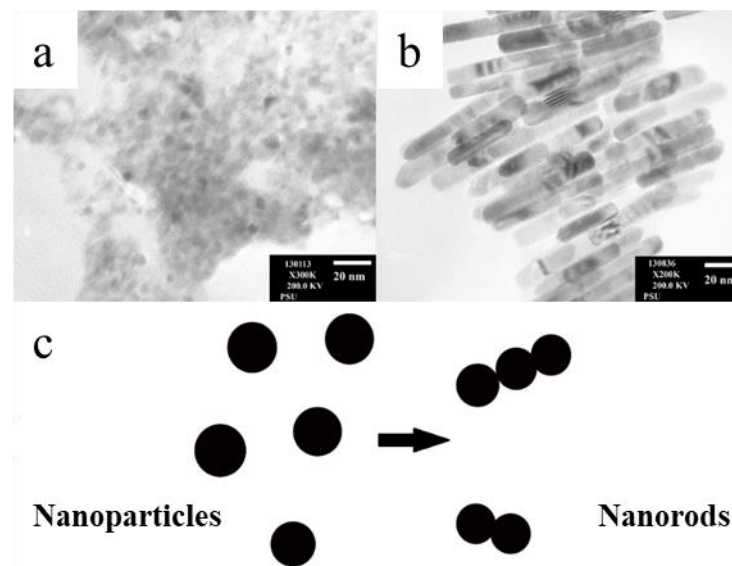


Figure 3.8 TEM image of ZnO prepared by using methanol as the solvent with reaction time a) 3 h and b) 3 days (edited from Phooplub and Muensit 2018) and c) is a sketch of mechanism from nanoparticles to nanorods.

The figure 3.8 shown ZnO nanostructures that were prepared by using methanol as a solvent, the images were derived from TEM at 200 keV. ZnO nanoparticles was obtained at the beginning stage as seen in figure 3.8a. After the reaction time was left for 3 days, the nanoparticles become nanorods with  $11.20 \pm 2.63$  nm in diameter and  $62.99 \pm 18.53$   $\mu\text{m}$  in length. Figure 3.8c is the formation mechanism from nanoparticles to nanorods according OA.

Chemical route can be applied to prepare vertical aligned nanorods on the substrate by spin coating nanoparticle on the substrate (Greene, *et al.* 2003). The reaction between 0.01 M  $\text{Zn}(\text{CH}_3\text{COO})_2 \cdot 2\text{H}_2\text{O}$  and 0.03 M NaOH in methanol was stopped at 2 h. Nanoparticles with 5 nm diameter were obtained. The nanoparticles were spun on the substrate at 3000 rpm several times. The spun substrate was preheated at  $100^\circ\text{C}$  and postheated at  $400^\circ\text{C}$  as preferred by Baruah and Dutta (Baruah and Dutta 2009). After that the substrate was immersed in the growth solution at  $90^\circ\text{C}$  to obtained vertical aligned ZnO nanorods as shown in figure 3.9. Low magnification of SEM (figure 3.9a) confirmed that the substrate was covered by average diameter  $250 \pm 50$  nm of ZnO nanorods with  $5.95$  rods/ $\mu\text{m}^2$ .

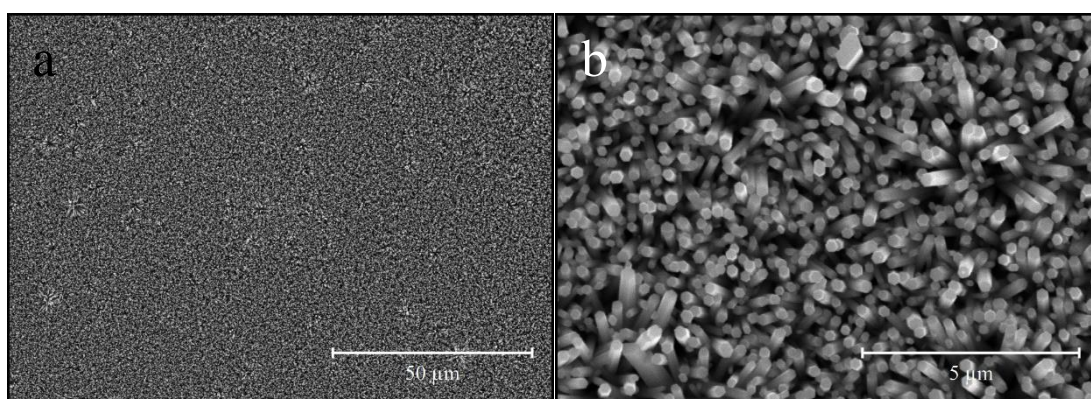


Figure 3.9. SEM image of a) low magnification and b) high magnification of vertical aligned ZnO nanorods on silicon wafer.

ZnO in microscale was also prepared by means of the OA. freestanding micro scale by dropping the nanoparticle directly to the growth solution. The expansion was depended on the reaction time.

Freestanding ZnO microrod was prepared by adaptation of the vertically aligned method. The seed solution was carried into the growth solution. After that the microrods were obtained as shown in figure 3.10.

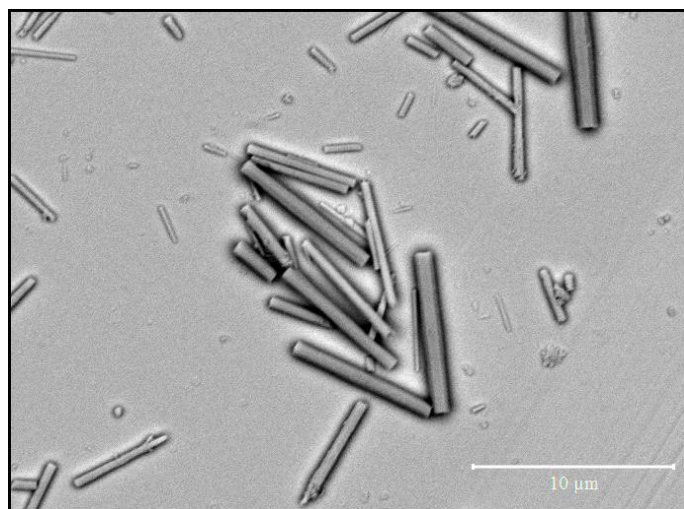


Figure 3.10 SEM image of ZnO microrods.

#### 3.4.2 Surface modification by polyelectrolytes

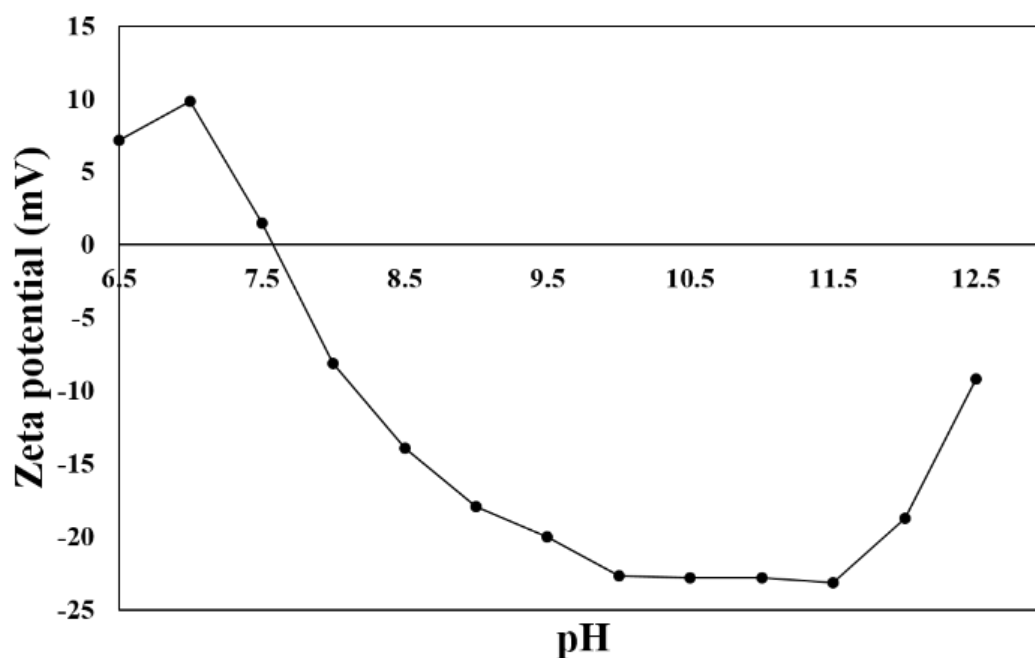


Figure 3.11. Zeta potential of ZnO in at different pH value.

The zeta potential at different pH was shown in figure 3.11. Higher value meant the higher fixed charge at the surface of the nanoparticles. Amount of 24 mV was found in the pH range 10 to 11.5. ZnO nanoparticles were dissolved when the pH value was reached to 12.5. The isolation point was found nearly to pH 7.5.

The nanorods were coated by PDDA at pH 10 to maximize the surface charge by mixing at 1:1 ratio. After the process, the coated nanorods were filled and immersed in the pH 7 buffer. The Zeta potential of coated nanorods were still positive value. This meant the surface of the nanorods were capped by PDDA completely. The coated nanorods and negative charge polyelectrolyte PSS were mixed by 1:1 ratio to switch the surface charge of nanorods. The result of the coated of nanorods was shown in figure 3.12.

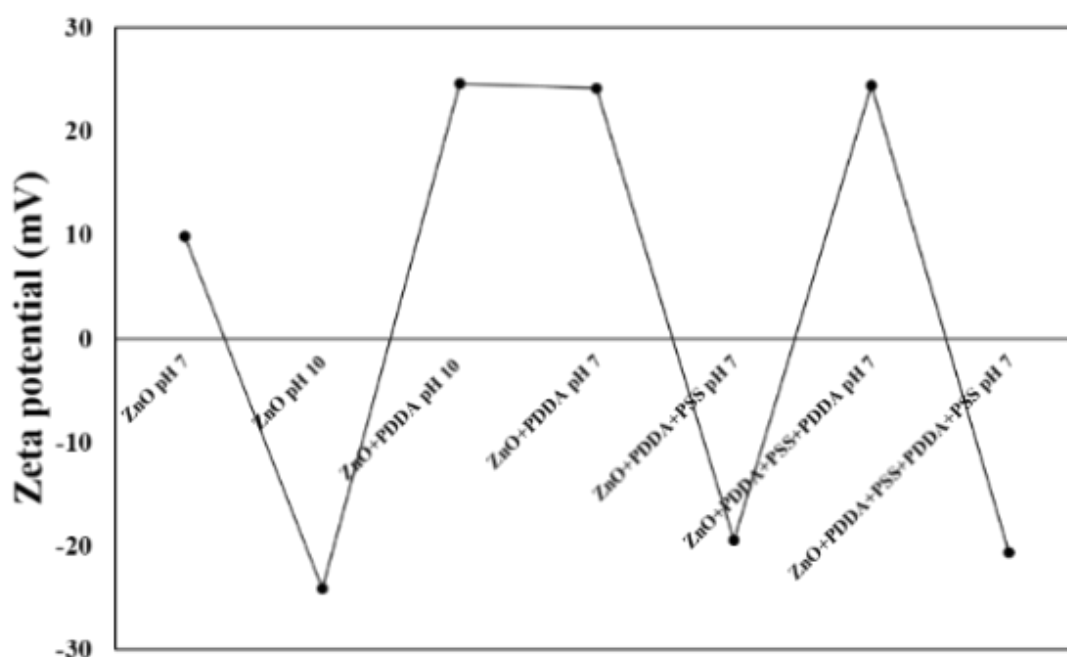


Figure 3.12. Zeta potential coated ZnO nanorods.

Figure 3.12 shown Zeta potential of coated ZnO nanorods. The resulted shown that the surface charge of ZnO nanorods were switch to positive of negative charge by coating with positive or negative polyelectrolyte. To confirm the existence of the coated layer, the nanorods was visualized by using UV-Visible and TEM.

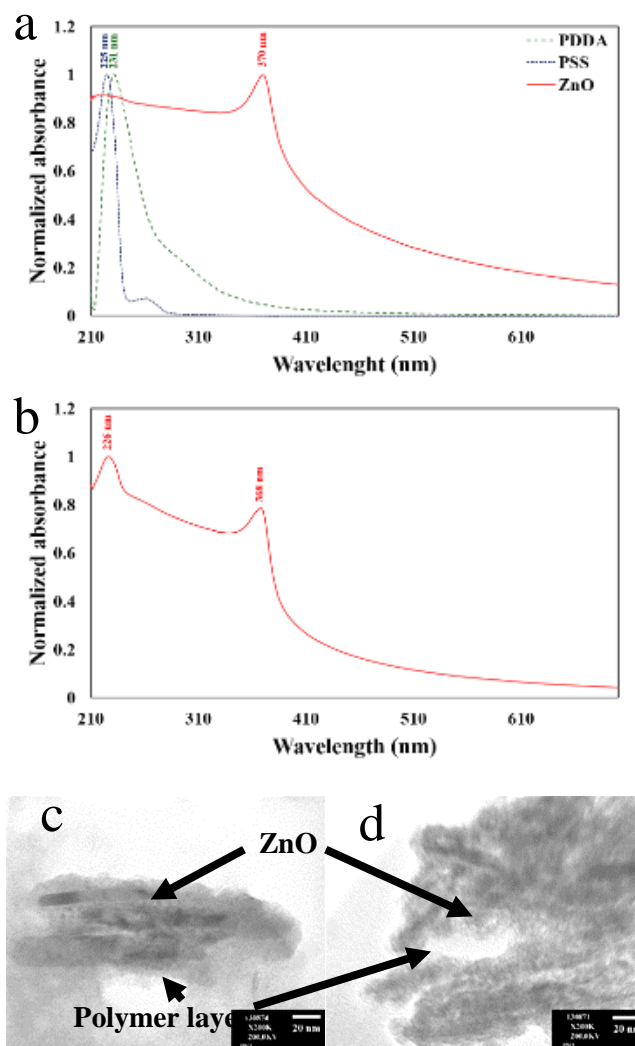


Figure 3.13 a) absorption spectra of ZnO, PDDA and PSS, b) absorption spectrum of coated nanorod c) and d) TEM image of 1 layer and 2 layers of PSS/PDDA coated ZnO, respectively.

Figure 3.13a shown absorption spectra of ZnO nanorods, PDDA and PSS. The absorption peak was observed at 370, 231 and 225 nm for ZnO nanorods, PDDA and PSS, respectively. Figure 3.13b was the absorption spectrum of the coated nanorods. The result shown the two absorption peaks at 226 and 368 nm. The first peak was combination of PDDA and PSS and the second peak were form the nanorods.

Figure 3.13c and 3.13d shown the coated layer on nanorods. The nanorods were completely covered by the polymers. The stability of ZnO nanorod and coated ZnO nanorods were test by tracking the absorption at 370 nm. The results were shown in figure 3.14.

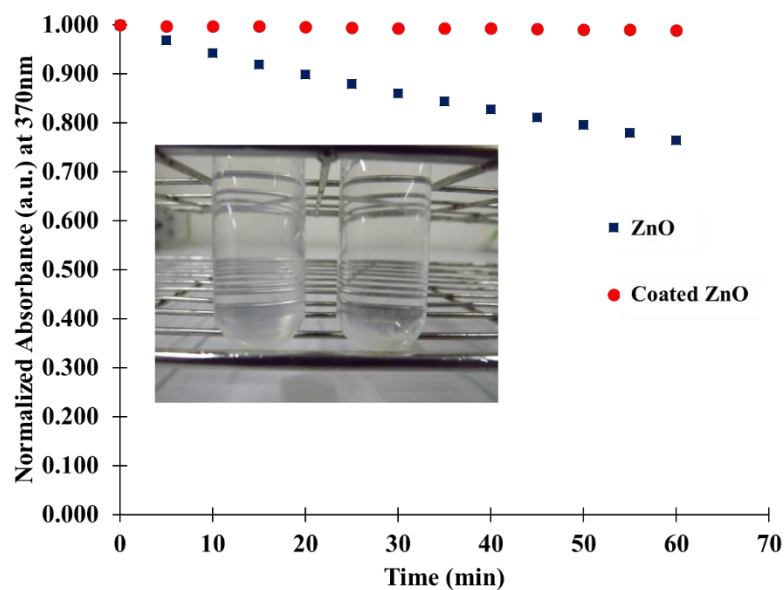


Figure 3.14. Time dependent of normalized absorbance peak of ZnO and Coated ZnO nanorods.

The absorption at 370 nm of ZnO nanorods continuously decreased in DI water. This because the decreasing of the concentration of ZnO in the solution that resulted from the sediment of the ZnO. While the absorption of the coated ZnO nanorods was still stable after 1 h because the coating layer maintained the surface charge of ZnO nanorods at high level. This implied that the coating enhanced the colloidal stage of ZnO nanorods.

### 3.5 Conclusion

Crystal growth of ZnO by chemical route was depended upon several parameters. The shape and the size of ZnO could be controlled since the nucleation process. Difference kind of participating agents and solvents affect the formation. NaOH affected the crystal structure because the size of Na ion is smaller than the O ion in ZnO crystal. This resulted to the penetration of Na ion in the crystal, while KOH did not affected the changing of ZnO crystal. The different growth rate of each crystal planes of ZnO cause the crystal growth to hexagonal structure.



The size of ZnO could be deduced by modifying the growth rate through the capping agent. Electrostatic binding between ZnO and the capping agent resulted to the slower penetration of Zn and O ion to the ZnO nuclei. The polarity of the solution was another one factor for the growth of ZnO. The nanoparticles prepared in methanol shown very smaller size than in DI water.

The charge at the surface of ZnO was depended on pH of the media. The maximum value was observed at pH 10. Application of polyelectrolyte could maintain the charge of the ZnO to maximize at pH 7.0. In addition, the appearance of polyelectrolyte enhanced the colloid stability to the ZnO in DI water.

## **CHAPTER 4**

### **ATOMIC FORCE MICROSCOPY: AN APPLICATION FOR NANOSTRUCTURE CHARACTERIZATION**

This chapter involves the applications of Atomic Force Microscopy (AFM) to probe physical properties of nanostructure materials. The measurement includes topography, nanoscale force and piezoelectric parameters which are useful in energy harvesting.

#### **4.1 Introduction**

Surface properties, for example, adhesion, bonding, surface contamination, corrosion, surface morphology, surface roughness, surface topography, failure analysis, process monitoring, surface chemistry, biological characterization, physical properties, are importance to answer research questions. The properties are useful for material processing. Many instruments and modification techniques have been developed.

AFM is one of popular technique for surface characterization. The instrument suits for investigation in nanoscale. The principle of AFM is the position of the microcantilever with a sharp tip onto the interested sample. The interaction between the tip and the sample is evaluated through the changing of cantilever properties. The invention was revealed in the early 1980s in term of scanning probe microscope (SPM). The first instrument was developed by G. Binnig and H. Rohrer. The method acquired the texture of the surface sample from the current due to the tunneling effect. However, the conductivity of the sample and the cantilever was required.

AFM was developed to overcome the limitation in 1986 by Binnig, Quate and Gerber. Even through, the lateral resolution was around 1 nm that was limited by the sharp of the tip, the conductivity independent let the technique operate on various kind of materials. The located of the cantilever tip onto the sample not only gives the topography information but also gives other physical properties, for example, electrical, magnetic, mechanical, and so on. Comparison to other famous imaging

techniques, AFM provides high contrast in vertical and more information of physical properties, while SEM and TEM give only 2D image with chemical composition. In addition, vacuum environment is required for the last two techniques. Nowadays, a lot of measurement modes have been added into the commercial AFM instrument.

This chapter focuses on the surface topography imaging, force distance curve microscope, and piezoelectric force microscope (PFM) that frequency use in the energy harvesting field.

## **4.2 Atomic force microscopy**

AFM consists of 4 parts: cantilever, detector, piezoelectric scanner and controller which work together to obtain the topography image. The basic AFM operation is started by approaching the cantilever, microcantilever with the sharp tip at the end, onto the sample until the cantilever is bent. After that, the cantilever is moved around the surface sample by piezoelectric scanner. During the operation, the surface roughness is recorded from the moving of the cantilever. The bending of the cantilever is the feedback signal to indicate the changing of surface height by application of a laser diode projected on the cantilever. The laser beam from the laser diode is focused onto the cantilever and reflected into the photodetector. All parts are controlled by the controller.

The topography images can be obtained from two modes that are static and dynamic modes. In the static mode, the bending of the cantilever is kept constant along the scanning. When the cantilever is bent more than the setting value, the cantilever is programmed to move out of the sample until the bending becomes the setting value. Whereas in the case of the bending of the cantilever is lower than the setting value, its movement will be opposite. In this mode the cantilever tip directly contacts to the sample, which can be applied both for soft and hard materials. In the dynamic mode, the cantilever is vibrated along the experiment. The changing of the magnitude of vibration is used instead of bending. This mode is suitable for soft materials because the mode is contactless. To obtain the image with high quality, each part of AFM must be considered.

### - Cantilever

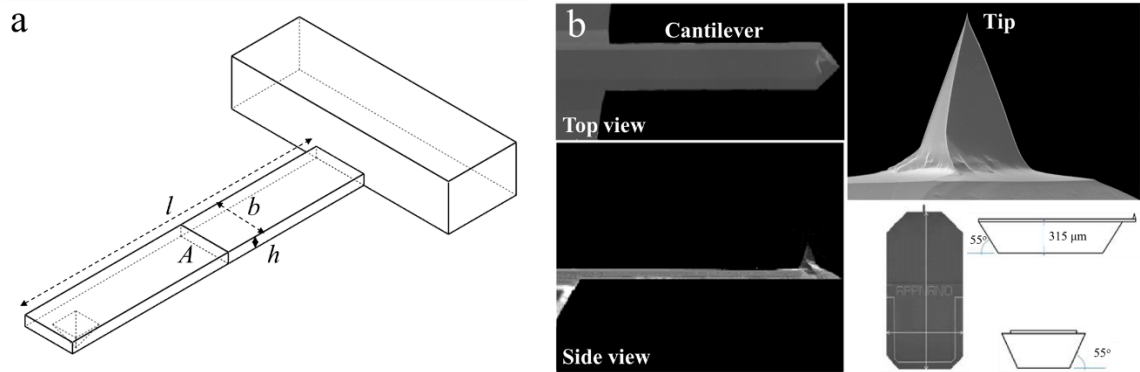


Figure 4.1. The sketched image of a) AFM cantilever and b) the photograph of ACL model (adapted from Applied NanoStructures, Inc., USA).

Cantilever is a fixed one end of constant cross-section area bar as shown in figure 4.1. Bending of the cantilever can be transverse, longitudinal or torsional mode. The transverse mode plays an important role in the AFM operation. The deformation of the cantilever in transverse mode is described by Euler–Bernoulli beam theory.

$$\frac{\partial^2}{\partial x^2} \left( EI \frac{\partial^2 w}{\partial x^2} \right) + \rho A \frac{\partial^2 w}{\partial t^2} = p \quad (4.1)$$

where,  $E$ ,  $I$ ,  $A$  and  $\rho$  are the Young's modulus, the second moment of the cross-sectional area, the cross-sectional area, and the density of the cantilever, respectively. The distributed force  $p$  is a cause of deformation in transverse direction  $w$ . In a case of free vibration, the distributed force disappeared. The equation 4.1 is a function of space and time. The solution is assumed as multiplication of space dependent  $X$  and time dependent  $\Phi$ .

For static mode, the deformation is time independent. The cross-section area is constant. The equation 4.1 is deduced as following:

$$EI \frac{\partial^4 w}{\partial x^4} = p \quad (4.2)$$

The equation of motion is obtained by determination the boundary condition of the cantilever. In the case of the external force is loaded at the free end, the equation of motion is shown as following:

$$w = \frac{Fx^2}{6EI} (3l - x) \quad (4.3a)$$

$$I = \frac{bh^3}{12} \quad (4.3b)$$

where  $l$  is the length of the cantilever. The maximum deflection at the free is shown as following:

$$\delta_{max} = \frac{Fl^3}{3EI} \quad (4.4)$$

To evaluate the equation, the equation 4.4 is compared to Hook's law equation. The spring constant  $k$  is obtained as following:

$$k_c = \frac{3EI}{l^3} \quad (4.5)$$

The spring constant determines the elasticity of the cantilever. The table 4.1 is an example of the cantilevers that used in contact mode.

Table 4.1 List of contact cantilever from Applied NanoStructures, Inc.

Code Name	Spring Constant (N/m)	Frequency (kHz)	Length ( $\mu\text{m}$ )	Width ( $\mu\text{m}$ )	Thickness ( $\mu\text{m}$ )	ROC (nm)
SHOCON	0.10	28	225	43	1.0	6
SICON	0.20	12	450	40	2.5	6

Dynamic mode, the cantilever is vibrated at the frequency nearly the natural frequency of the cantilever. The frequency is determined by the eigenfrequency as following:

$$\omega = \alpha^2 \sqrt{\frac{EI}{\rho A}} \quad (4.6)$$

where  $\alpha$  and  $\omega$  is wavelength and the eigenfrequency of the cantilever. The first mode, that is the mode with the highest amplitude of vibration, is determine by  $\alpha = 1.875$ . Table 4.3 is a cantilever for the dynamic mode.

Table 4.2 List of dynamic cantilevers from Applied NanoStructures, Inc.

Code Name	Spring Constant (N/m)	Frequency (kHz)	Length ( $\mu\text{m}$ )	Width ( $\mu\text{m}$ )	Thickness ( $\mu\text{m}$ )	ROC (nm)
ACCESS-NC	93	320	150	54	5.50	6
ACL	58	190	225	40	7.8	6
ACST	7.8	150	150	28	3	6
ACT	37	300	125	4	30	6

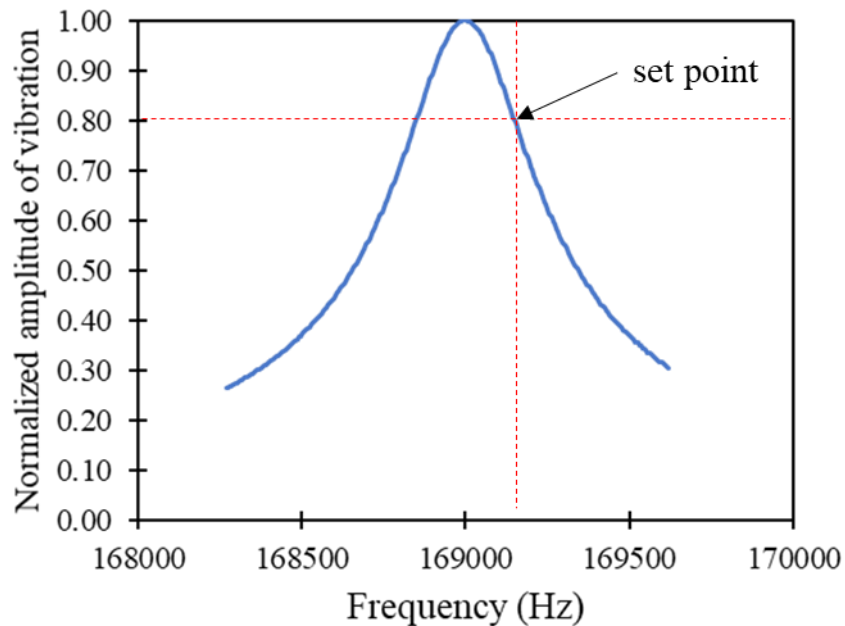


Figure 4.2. Resonant frequency of ACL cantilever model.

In the operation process, the cantilever is excited at the frequency with amount of 80% of amplitude of vibration of the resonance frequency. When the cantilever moves to the sample, the force exerts to the cantilever tip that affect shifting of the resonant frequency.

#### - Detector

There are several methods to measure the bending of the cantilever. Optical technique is found the most in conversional AFM. Laser from a laser diode is pointed to the free end of cantilever and reflected to a photodiode module. The photodiode module consists of two or four photodiodes. The bending of the cantilever is evaluated from the current level of each unit. Module of two photodiodes detects only out-of-plane deformation, while in-plane and out-of-plane are obtained for the four photodiodes. Figure 3 is the schematic of Nanosurf Easyscan2 AFM model.

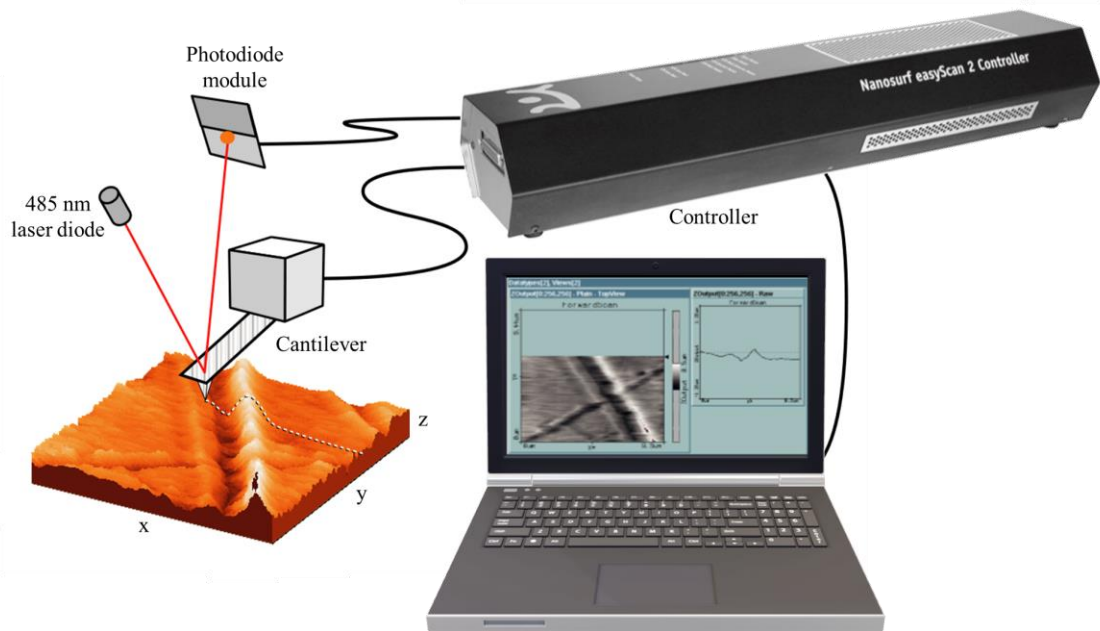


Figure 4.3. Schematic of AFM model easyscan2 (Nanosurf, Switzerland)

#### - Piezoelectric scanner

A high precision and resolution are required for AFM scanning to collect texture in nanoscale from the sample. Electromagnetic and piezoelectric scanner are candidate in the instrument. Low operation voltage and linear motion are the advantages of the electromagnetic scanner over the piezoelectric scanner. However, the speed of movement of the piezoelectric scanner make the scanner reaches to the setting position at short time and high resolution. Some models combine the advantage of the two scanners, for example, FlexAFM of Nanosurf AG consists of electromagnetic scanner in xy-plane and piezoelectric scanner in z-direction.



### -Controller

Controller is the module that control the system to image the physical properties of the sample. Feedback module is added to the controller to increase the precision of the system. the figure 4.4 is the feedback control that used in the Nanosurf easyscan2.

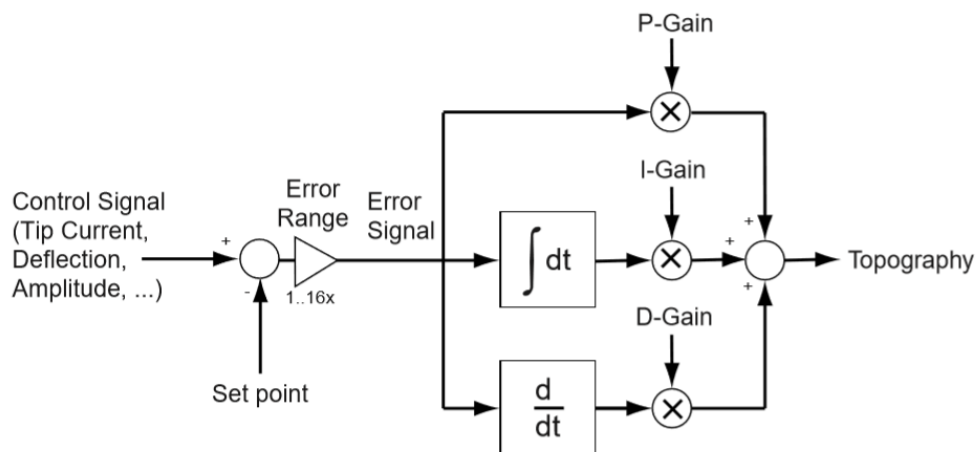


Figure 4.4. PID loop gain for Z controller in Nanosurf easyscan2 (Nanosurf, Switzerland)

A proportional–integral–derivative controller (PID) is used to control the moving of the cantilever by decision from the different of the control signal and the set value. The signal difference or error range is analyzed in term of the proportional, integral and derivative value from the set point. The feedback control then designs the command to the moving of the cantilever until the control signal equal to the set point.

In dynamic operation, the amplitude of vibration is used as the feedback signal. In the case of 50 % amplitude of vibration is set. The amplitude of vibration is kept along the scanning. When the amplitude of vibration is increased. This meant the cantilever is far from the sample. The PID control commands the cantilever to move to the sample until the amplitude of vibration come to the 50 %.

## - Topography imaging

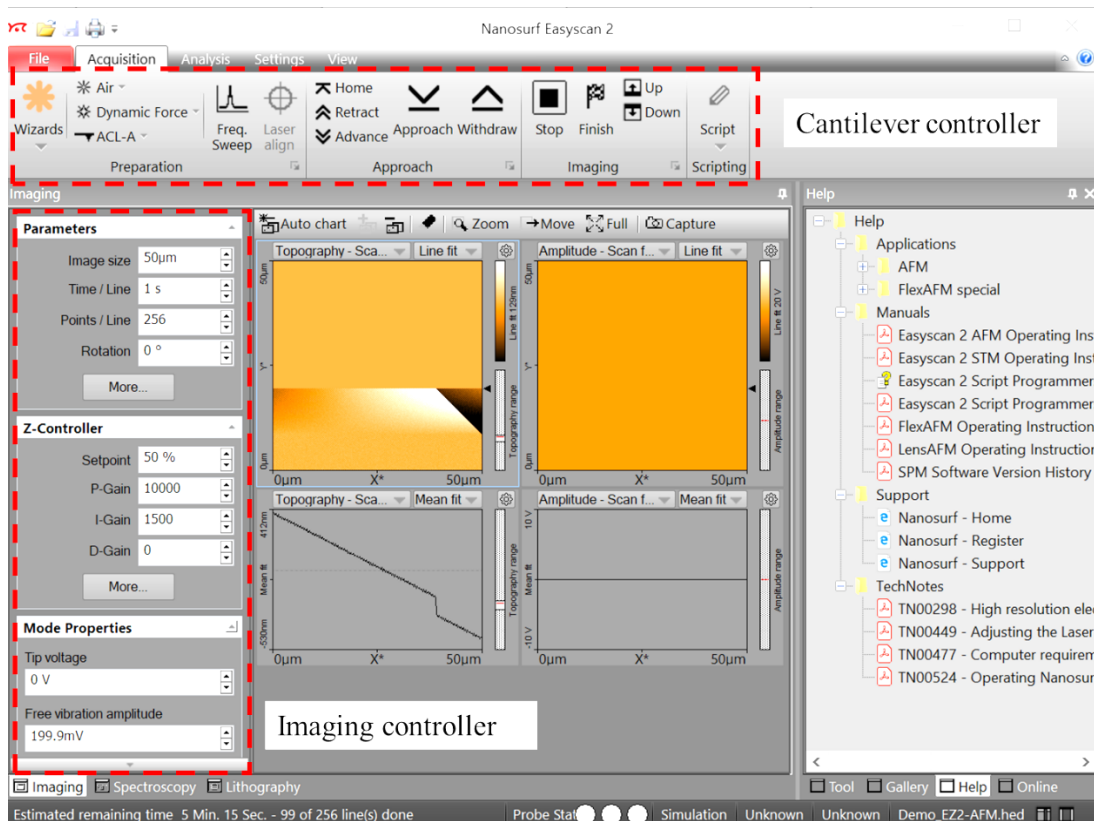


Figure 4.5. The graphic user interface (GUI) of Nanosurf easyscan 2.

Figure 4.5 is the GUI of the Nanosurf easyscan 2 for topography imaging. The GUI consists of 3 parts, cantilever controller, imaging controller setting and charges recorder from the scanning. In this thesis, the dynamic operation was elected because the tip and the sample did not directly contact, this resulted to less damage of the tip and the sample during the scanning. The high-quality imaging was obtained under optimal condition. Surface roughness of the smooth surface, particularly, glass slide or silicon wafer, were in a range of nanoscale. Higher amplitude of vibration could not detect the changing of the level in the scale. In this case, smaller as possible was preferred. In contradiction, amplitude of vibration should be enough to detect the changing of the level for the sample with high surface roughness that suited for higher amplitude of vibration.

The PID loop gain was related to the speed to set the cantilever to reach the initial state. In the case of the amplitude of the cantilever was set at the 50%. During the scan, if the cantilever was far away from the sample, the amplitude of vibration was

increased. The different signal of the amplitude of vibration was feed to the feedback loop to make the decision to move the cantilever until the amplitude of vibration become the initial state. The higher loop gain corresponded to the faster moving in Z-direction. However, noises were also amplified. The optimal condition that was the maximum loop gain with maximum signal to noise ratio was recommended. Figure 4.6 was the topography image of ZnO nanorod vertical aligned on glass slide obtained under 10000 p-gain and 1000 i-gain with 2 s line scan.

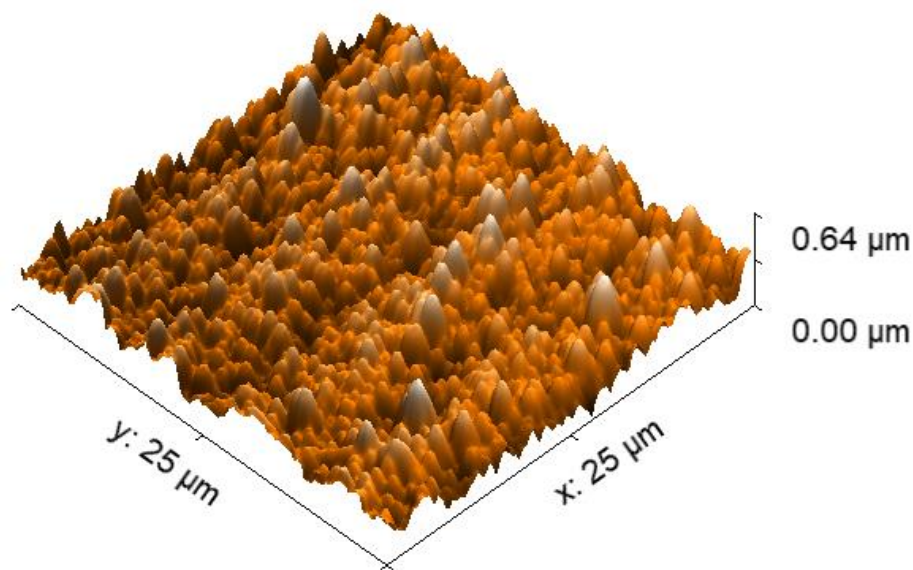


Figure 4.6. Topography image of ZnO nanorods vertical on glass slide.

### 4.3 Force displacement curve spectroscopy

Force distance curve is the probing tool for surface characterization bases on recording the force corresponding to the loading and unloading of the metallic tip onto the sample surface. The technique not only determines the interaction between them but also reveals the viscosity, lubrication thickness, and local variations in the elastic properties of the sample. The high resolution can be obtained by using the AFM based instrument.

The curve consists of three parts, the zero line, the non-contact region, and the contact region (Cappella and Dietler, 1999). The zero line is the state that the tip is far away from the surface sample. There is no interaction force that resulted to the zero value of cantilever deflection. The interaction force is overcome when the metallic

tip is closely to the surface sample. The interaction was described by the Lennard Jones interaction. When the attractive force is dominated, the tip suddenly moves to the sample surface. This phenomenon calls the jump-to-contact distance that occurred by the adhesion force.

After the region, the bending of the cantilever is dominated the repulsive force between the tip and the sample. The rate of bending is depended on the mechanical properties of the cantilever and the surface sample. The force that is exerted this regime is shown as following:

$$F = -k_c \delta_c \quad 4.7$$

where  $\delta_c$  and  $F$  are the cantilever deflection and the tip-sample force respectively. However, the curve obtained from the method is not the force-distance curve but the force displacement curve. The distance  $D$  is derived from the subtraction of the piezo scanner  $Z$  by the cantilever deflection

$$D = Z - \delta_c \quad 4.8$$

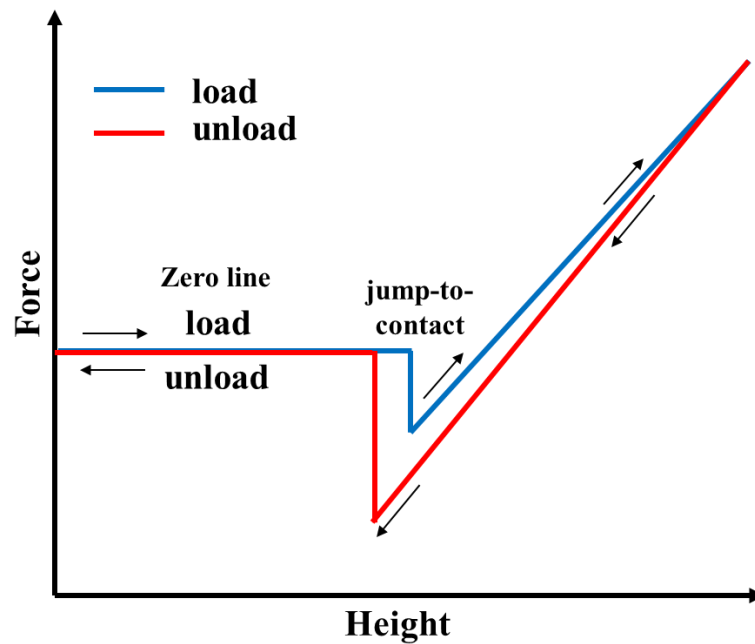


Figure 4.7. The force distance curve.

The slope of this regime is depended on the young's modulus of the materials. The higher slope indicates the higher of young's modulus. To evaluate the property, unloading curve is used because the curve is independent from plastic deformation. Young's modulus of the sample is calculated by using Hertz's contact mechanics theory. The tip apex was assumed to be a half sphere and the adhesion force between the contact area was neglected. The contact radius ( $a$ ) according to the theory was given as following:

$$a_{Hertz} = \left( \frac{RF}{K} \right)^{1/3} \quad 4.9$$

where  $R$  were the tip radius and  $K$  was the reduced elastic modulus given by

$$\frac{1}{K} = \frac{3}{4} \left( \frac{1 - \nu_i^2}{E_i} + \frac{1 - \nu_s^2}{E_s} \right) \quad 4.10$$

$E$  and  $\nu$  in (2) were Young's modulus and Poisson's ratio, respectively. Subscript  $i$  and  $s$  were the indenter and sample, respectively. Generally, the cantilever tip was made of silicon wafer that resulted to the young's modulus of the tip was greater than young's modulus of the sample. The reduced modulus could be approximated in the form

$$\frac{1}{K} = \frac{3}{4} \left( \frac{1 - \nu_s^2}{E_s} \right) \quad 4.11$$

For very small indentations, the contact radius was rewritten by  $\sqrt{RD}$ .

#### 4.4 Application of force displacement curve in energy harvesting

Scaffolds play an important role in tissue engineering. The scaffolds serve as a temporary template for cell interaction and transformation. The chemical and physical properties of the scaffold are necessary to match to the cell pathway or tissue environment. Several kinds of materials have been elected for the application, for example, biomaterials, synthesized polymers and ceramics. Collagen was discussed in

osteogenesis because it was around 95% in bone matrix. In addition, collagen along with water were substantial constituents of skin, tendon, ligament, cornea, and cartilage (Marks and Odgren 2002)

Collagen have been discussing not only basement scaffold but also as the binder of non-biomaterials and cells. A unit collagen is triple helix of two identical chains and difference one. Each chain is motif of (Gly-X-Y)<sub>n</sub> chains, where n is 337-343. Collagen molecules bond each other by hydroxyl group at the terminal. Collagen was reinforced to a lot of materials to enable multifunction to the scaffold. Metal and metal oxide are considered for antibacterial function (Sawei *et al.*, 1995). The surface is able to generate hydrogen peroxide when is immersed in the aqueous solution.

ZnO was found to be improved antibacterial function to scaffold. Amount of 10 µg/ml inhibited the growth of *S aureus* and *E coli* (Emami-Karvani and Chehrazi 2011). The activity was depended on the shape and the size of the ZnO. Nanoparticle and nanorod of ZnO shows *E coli* inhibition growth at 10 mM while 7 times concentration were required in the powder form (Tam *et al.* 2008). In addition, ZnO in scaffold effect directly to the mechanical (Phooplub *et al.* 2018).

The effect of concentration of ZnO in collagen film was tested by using force distance curve. Each of reinforce ZnO collagent film was tested a hundred time by AFM (Nanosurf Easyscan2, Nanosurf) based instrument with ACL-A (AppNano, USA) cantilever tip. The development of young's modulus by application of ZnO was reported. Content of ZnO nanorods were affected the young's modulus of the collagen by increasing from 9 to 16 GPa. In addition, the denature temperature of collagen was shift to higher temperature this resulted the Young's modulus the reinforced collagen film was independently to the temperature around room temperature to 37 °C (Phooplub *et al.* 2018).

#### **4.5 Piezoresponse Force Microscopy (PFM)**

PFM bases on contact mode of AFM. The AFM cantilever is biased by sinusoidal wave to activate the piezoelectric effect of piezoelectric materials. The piezoelectric signal was traced from the deflection of the cantilever by lock-in amplifier. The conductive cantilever tip is used in order to neglect the effect of oxide

layer forming (Morita, et. al., 1990). The schematic of the PFM is summarized in figure 4.8.

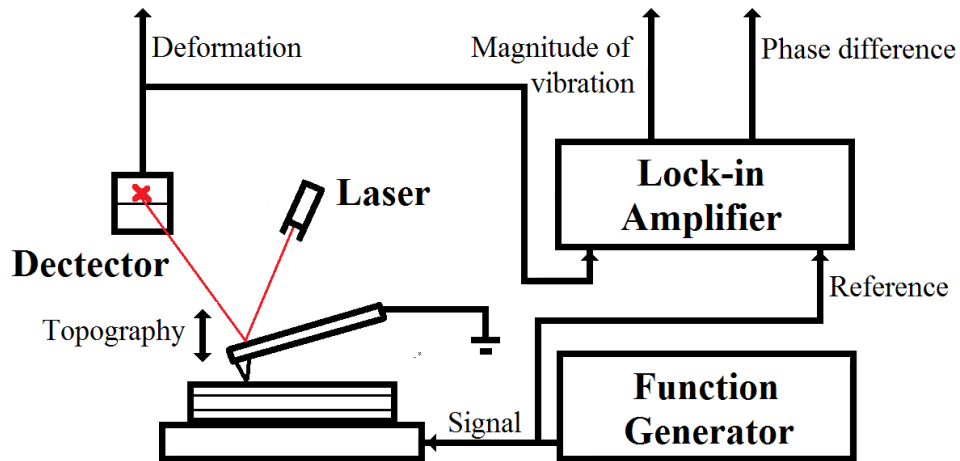


Figure. 4.8. Schematic diagram the piezoelectric force microscopy.

Because the topography and PFM image are simultaneously measured. The bias AC voltage to activate the piezoelectric effect must be higher than the topography signal. The range of 10 to 100 kHz are used. However, this range can be perturbed by the natural frequency of the cantilever, for example, SICON cantilever model in the table 4.2. The magnitude of the AC voltage is a one parameter to tune the contrast of the PFM image. Piezoelectric is linearly relation between mechanical and electrical properties. Increasing the magnitude of vibration results to the increasing of the piezoelectric vibration. The condition of frequency selection should be far always from texture of the tested surface to neglect combination of topography signal in PFM image. However, the PFM signal is depended on the piezoelectric coefficient of the materials. Sometime, Amount of 10 V AC is required for the low piezoelectric coefficient materials (Fortunato *et al.* 2018). The thickness of the sample is a one parameter that can reduced the excitation voltage. A few electrical potentials can produce up to 1 MV/m electric field for very thin sample.

The deflection of the cantilever, that consists of topography signal and piezoelectric, is analyzed by using lock-in amplifier. The signal is multiplied by the referent signal that is the AC signal for piezoelectric activation. The DC product term, that is the piezoelectric signal, is collected by application of lowpass filter.

The PFM measurement consist of two kinds of force fields involved in the observation; electrostatic and electromagnetic regimes that was analyzed by Kalinin and Bonnell (Kalinin and Bonnell, 2002). Electrostatic regime in imaging is resulted from capacitive and coulombic tip-surface interaction as following:

$$F_{cap} = \frac{1}{2}(V_{tip} - V_{loc})^2 \frac{dC_{loc}}{dz} + \frac{1}{2}(V_{tip} - V_s)^2 \frac{dC_{nl}}{dz'} \quad (4.12)$$

where,  $V_{tip}$  is the applied voltage at the cantilever tip,  $V_{loc}$  is the domain-related local potential directly below the tip,  $V_s$  is the surface potential averaged over the distance comparable to the cantilever length,  $C_{loc}$  is the local part of tip-surface capacitance, and  $C_{nl}$  is the non-local part due to the cantilever. The first term is the resultant force occurred by charge accumulation at the tip and the location of the domain below the tip. The last term is indicated the capacitance between the cantilever and the equivalent area of the test surface. The force acts as a constant background on the image. The conductance is calculated by using plane-plane geometry as following

$$\frac{dC_{nl}}{dz'} = \frac{\varepsilon A}{z'^2} \quad (4.13)$$

where,  $A$  is the effective cantilever area and  $z'$  is the gap width ( $z + \text{tip length}$ ).  $C_{loc}$  is tip-surface capacitance can be analyzed by using the image charge method and assuming that the distance between the tip-sample is very small when compares with tip radius  $R$ .  $C_{loc}$  converges to the universal dielectric limit (Lebedev, *et.al.* 1966).

$$C_{loc} = 4\pi\varepsilon_0 R \frac{\varepsilon_r - 1}{\varepsilon_r + 1} \ln\left(\frac{\varepsilon_r + 1}{2}\right) \quad (4.14)$$

Coulombic tip-surface interaction due to polarization and charge screening can be expressed by

$$E^u = \frac{(1 - \alpha)P}{\varepsilon_0(1 + \sqrt{\varepsilon_{rx}\varepsilon_{rz}})} \quad (4.15)$$



where,  $E^u$  is electric field above a partially screened ferroelectric surface,  $P$  is spontaneous polarization, and  $\alpha$  is the degree of screening.

Kalinin and Bonnell mentioned the three forces, local capacitive force  $F_{loc}$ , non- local capacitive force  $F_{nl}$ , and Coulombic force  $F_{Coul}$ , by substitution parameters in equations (4.12) – (4.15) and assumed that there was no screening effect which  $\alpha$  became zero. The results showed  $F_{Coul} < F_{nl} < F_{loc}$  by an order of magnitude. In realistic, the surface always completely screened by air resulted from the excludable coulombic contribution (Kalinin and Bonnell, 2002).

The capacitive force is derived by Hertzian' s approximation. The contact between the cantilever and the sample are perfectly elastic intermolecular force. The effective elastic modulus is modelled as series springs junction. The equation of deformation at the contact surface is become

$$w_{1\omega} = \frac{2}{3} \left( \frac{3}{4E^*} \right)^{2/3} R^{-1/3} F_0^{-1/3} F_{1\omega} \quad (4.16)$$

where,  $w_{1\omega}$  is the deformation at the first harmonic,  $E^*$  is the affected elastic modulus,  $R$  is the tip radius, and  $F$  is the applied force.  $F_0$  is the setpoint in contact AFM mode. The equation 4.16 is useful for the optimization for PFM imaging contrast.

For ferroelectric material, the effect of electromechanical is significantly affected the PFM contrast. There are two limits for theory, strong and weak indentation. The strong indentation is defined by high indentation force. The relation between the load  $P$ , indenter potential  $V$ , and indentation depths  $w$  is

$$w = \frac{a^2}{R} + \frac{2\beta}{3\alpha} V \quad (5.17)$$

$$P = \alpha \frac{a^3}{R} - \beta a V \quad (4.18)$$

where,  $\alpha$  and  $\beta$  are the material-dependent constants and  $a$  is the contact radius. Solving of the equations (4.17) and (4.18) result to surface deformation occurring by PFM operation. The application of strong-indentation has limit in a strong dielectric constant that can be break the assuming that  $V_s = V_{tip}$  (Giannakopoulous and Suresh, 1999).

Weak indentation is referred to very small contact area. The contribution of electric field cannot be neglected. Karapetian et al. shown general solution of electromechanical response of the surface by using the Green's function for a point force and charge (Karapetian *et al.*, 1999). The relation between deformation and the surface voltage is shown in equation 4.19 (Kalinin and Bonnell, 2002)

$$h = 2\pi \varepsilon_0 L(\kappa + 1)V_s \quad (4.19)$$

Even through the force between the surface and the tip affect the PFM contrast, the property of the material is still majority effected to the characterization. Piezoelectric is the third range tensor. The crystallographic orientation affect the magnitude of PFM signal ( Harnagea *et al.*, 2001) . According to the law of transformation (Nye, 1957): the relation between the material tensors and experimental coordinate is become:

$$d_{ijk} = a_{il}a_{jm}a_{kn}d_{lmn}^0 \quad (4.20)$$

where,  $d_{ijk}$  and  $d_{lmn}^0$  are the piezoelectric coefficient of the experiment and material coordinate, and  $a_{il}$  is the direction cosine that refer to Eulerian angle. In the case of hexagonal crystallography, the piezoelectric tensor consists of non-zero 5 elements. The general orientation of the crystal after rotational operation are

$$d_{33} = (d_{15}^0 + d_{31}^0)\sin^2\theta\cos\theta + d_{33}^0\cos^3\theta \quad (4.21)$$

$$d_{34} = -(d_{31}^0 - d_{33}^0 + (d_{15}^0 + d_{31}^0 - d_{33}^0)\cos 2\theta)\sin\theta\cos\psi \quad (4.22)$$

$$d_{35} = -(d_{31}^0 - d_{33}^0 + (d_{15}^0 + d_{31}^0 - d_{33}^0)\cos 2\theta)\sin\theta\sin\psi \quad (4.23)$$

where  $\theta$  and  $\psi$  are the Euler angles from x and y axes, respectively. In case of strong indentation, the deformation is dominated by  $d_{33}^0$  while the other effect provides as a minor contribution.

- ***Cantilever deflection***

The deflection of the cantilever is the major role for data interpretation. Crystal vibration can induce the cantilever deflection both normal and shear mode.

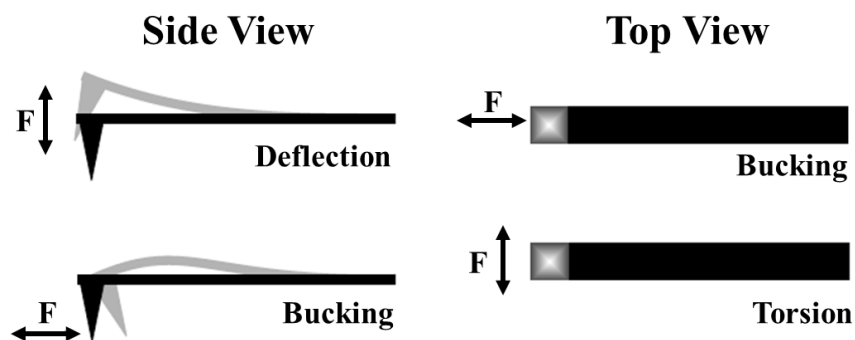


Figure 4.9. The cantilever deflection corresponding to crystal vibration (adapted from Soergel 2011)

The deflection of the cantilever according to piezoelectric crystal vibration is listed in the figure 4.9. The normal vibration of crystal induces transverse mode while the crystal shear mode can induce either torsion or bulking deflection modes. These depend on the orientation of the cantilever and the polarization of the crystal. The PFM image is categorized by two directions; out-of-plane and in-plane. Out-of-plane is derived by the optic sensor in z-direction. The signal is the combination of transverse and bulking modes. In-plane is the signal from the torsion of the cantilever. Bulking effect can be disappeared out-of-plane signal by two ways. The first way is using of the stiff cantilever and the second is rotation the sample until the bulking disappeared (Soergel 2011). The last methodology can be described by equation 4.21

and 4.22. When the angle  $\psi$  is zero, diminishing of equation 4.22 is occurred. While amount of 90 rotational angles is taken place, the equation 4.21 will be zero.

- ***PFM Signal***

Lock-in amplifier play an important role in separation of the PFM signal from the topography signal. Thee applied signal is the sinusoidal with angular frequency  $\omega_{app}$  as following:

$$V_{app} = V_{0app} \sin(\omega_{app}t + \alpha) \quad 4.24$$

The signal that is measured from the optical system is written by:

$$V_{op} = V_{pie} \sin(\omega_{app}t + \beta) + \sum_{i=1}^n V_i \sin(\omega_i t + \beta_i) \quad 4.25$$

where the first term is the PFM signal and the second term is topography signal. The multiplication of the equation 4.24 and 4.25 is

$$\begin{aligned} V_{out} = & \frac{V_{pie}V_{0app}}{2} (\cos(\beta + \alpha) + \cos(2\omega_{app}t + \beta + \alpha)) \\ & + \sum_{i=1}^n \left( \frac{V_i V_{0app}}{2} \cos((\omega_i - \omega_{app})t + \beta_i + \alpha) \right. \\ & \left. - \frac{V_i V_{0app}}{2} \cos((\omega_i + \omega_{app})t + \beta_i + \alpha) \right) \end{aligned} \quad 4.26$$

From the equation 4.26, the first term is frequency independent or DC term that is related to the amplitude of the PFM signal, the amplitude of the referent signal, and the phase different between them, while the topography signal is shift to the frequency of the referent signal. The PFM signal is collected by application of the lowpass frequency circuit to cutoff the signal at high frequency. It should be notice that the cutoff frequency should be lower than the referent signal to minimize the topography signal. For example, if the piezoelectric crystal is activated by the sinusoidal

wave at 20 kHz. The cutoff frequency should be lower than the value (Hong *et al.* 2001; Soergel 2011).

After the lowpass circuit, the signal is divided by the amplitude of the referent signal to obtain only the PFM signal with the phase shift. The PFM signal is perpendicular to the piezoelectric coefficient of the piezoelectric grain and the phase shift is correlated to the polarization direction of the piezoelectric grain as shown in the figure 4.10.

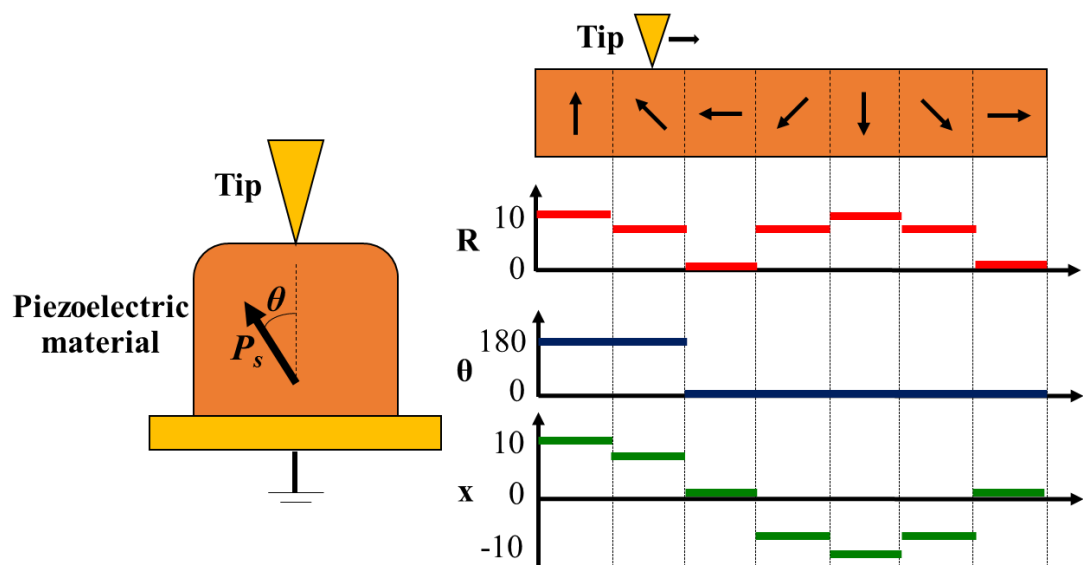


Figure. 4.10. The piezoresponse signal from lock-in-amplifier with respect to the polarization of piezoelectric grain (Editted from Soergel 2011)

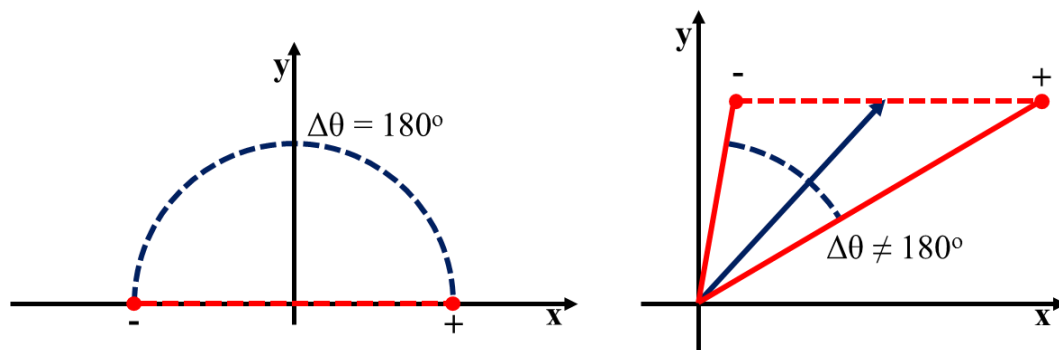


Figure. 4.11. The phase diagram of piezoresponse signal in case of with and without inherent background (Editted from Soergel 2011)

In realistic, the phase different of the signal is not completely  $180^\circ$ . This is because the inherence background(Jungk *et al.* 2008). The phenomena occur because the scan head which is a mechanically very complex entity and consequently exhibits a wealth of resonances that can be excited, resulting in a complex frequency spectrum (Soergel 2011). The effect shifts the signal from the x-plane that results to the phase different is lower than  $180^\circ$ .

#### 4.6 Application of PFM

ZnO wurtzite structure is overlap of Zn and O hexagonal structures. The distance between Zn and O molecule result to spontaneous dipole moment along the height of the hexagonal. The chapter 3 described both chemical and physical preparation of hexagonal rods. The rod structure was prepare both free standing and vertical aligned on the substrate. To analyte the piezoelectric of both cases the Euler's rotation was taken in to account. Hexagonal ZnO nanorod with  $10\ \mu\text{m}$  length analyte by using piezoelectric module in COMSOL Multiphysics software version 4.2 update 3 (COMSOL, Inc. USA). The material parameters were the same as chapter 2 table 2.4. The Euler's rotation tensor was added to the model according to the physical rotation. The boundary condition was related to the PFM measurement by grounding at the substrate and electrical voltage was applied at the top of the free end.

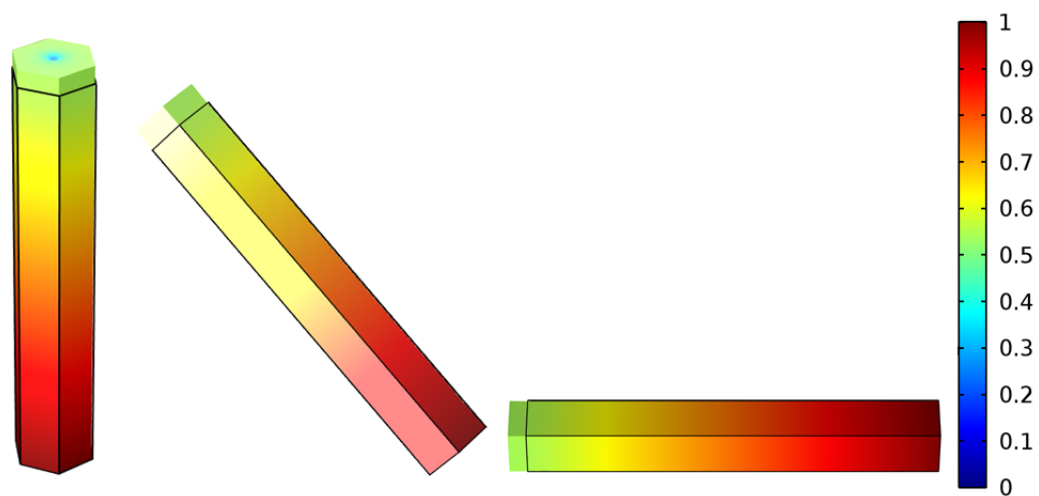


Figure 4.12. The deformation of ZnO hexagonal rod at  $0^\circ$   $45^\circ$  and  $90^\circ$  degree from z axis. The color contour indicated the normalized electrical voltage.

Figure 4.12 shown the result from the simulation. The rod was expanded in the longitudinal axis by piezoelectric effect that was independent of the rotation operation. This because the external voltage is applied at the same point that result to the average deformation was constant. However, the deformation in z-axis or  $w$  (out-of-plane signal) and y-axis (in-plane signal) or  $v$  was depended on the rotation operation. The maximum value was observed in the case of the rotation angle was zero for  $w$ . The value was decreased when the angle was increased and become zero when the axis reached to  $90^\circ$ . The results were opposite to  $v$  as shown in figure 4.13.

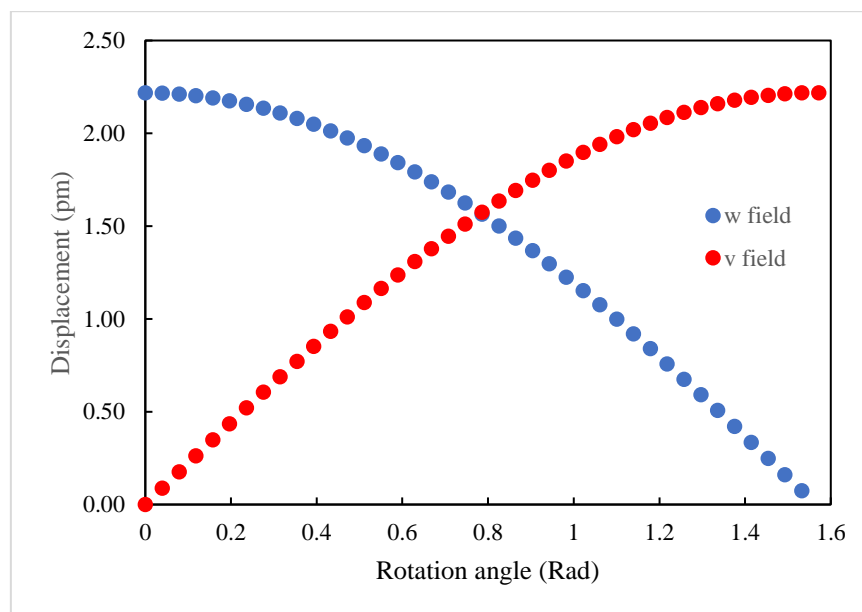


Figure 4.13. Relation between deformation and rotational angle.

The results were corresponded to equations 4.21 to 4.23. When the rotation angle was zero the equations 4.22 to 4.23 and the first term of the equation 4.21 become zero that resulted only  $d_{33}$  was observed. In the case of  $90^\circ$ , equation 4.21 was zero. The deformation was dominated by the effect of  $d_{15}^0$  or another word, when the PFM tip was located at the side of rod that lied on substrate, the applied would be induced the shear mode deformation as shown in figure 4.14.

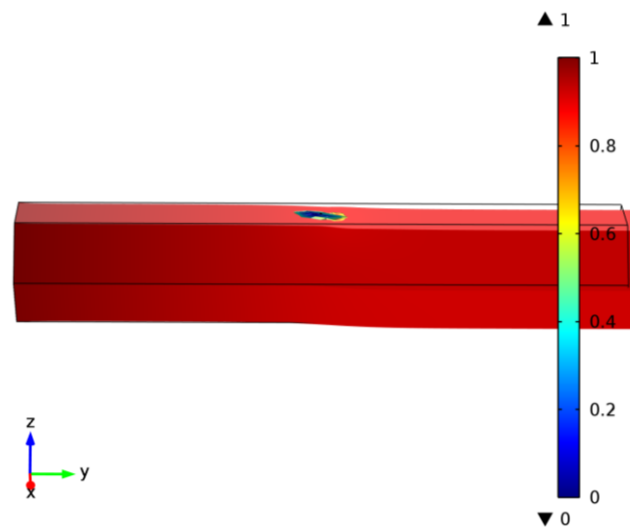


Figure 4.14. The deformation of rod when the cantilever tip was located at the middle side. The color contour indicated the normalized electrical voltage.

To compare the results, adapted AFM in the figure 4.9 was employed in this work. The on the commercial PZT bimorph. The electrode on the bimorph was removed by a polisher. The results were shown in figure 4.15. The piezoelectric effect of the material was activated by sinusoidal wave with 10 V peak. Figure 4.15a shown topography image of the PZT bimorph. Figure 4.15b to 4.15f shown piezoelectric image of the PZT bimorph with different frequency. At 20 kHz, the topography signal perturbed the piezoelectric signal resulted to the combination of the two signals in the image. The effect was able to neglect by increasing the frequency of the activated signal. From the results, the perturbation of the topography was disappeared at the frequency higher than 30 kHz.



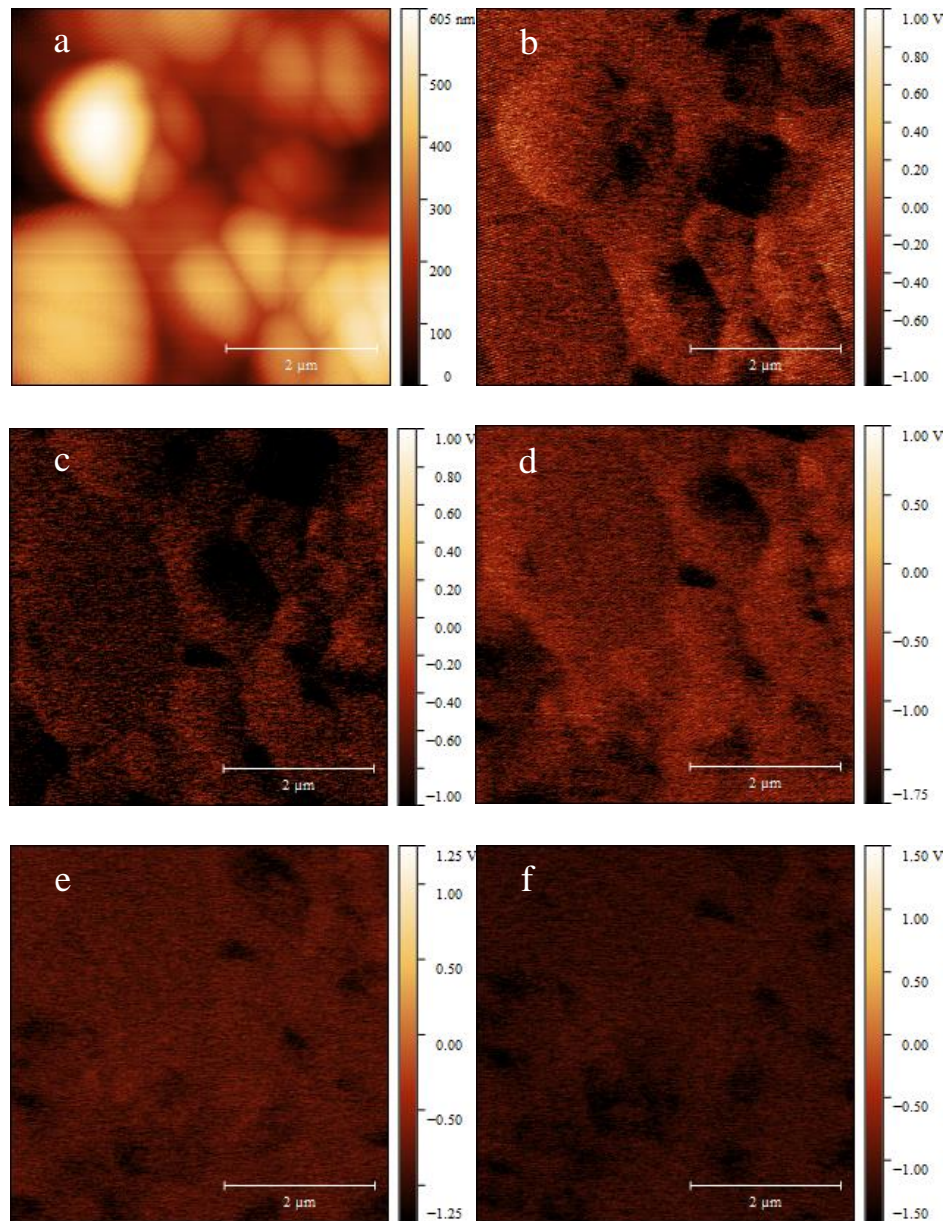


Figure 4.15. PFM characterization of commercial piezoelectric bimorph, a) topography image, b), c), d), e), and f) were PFM images of the bimorph at 20, 25, 30, 35, and 40 kHz, respectively.

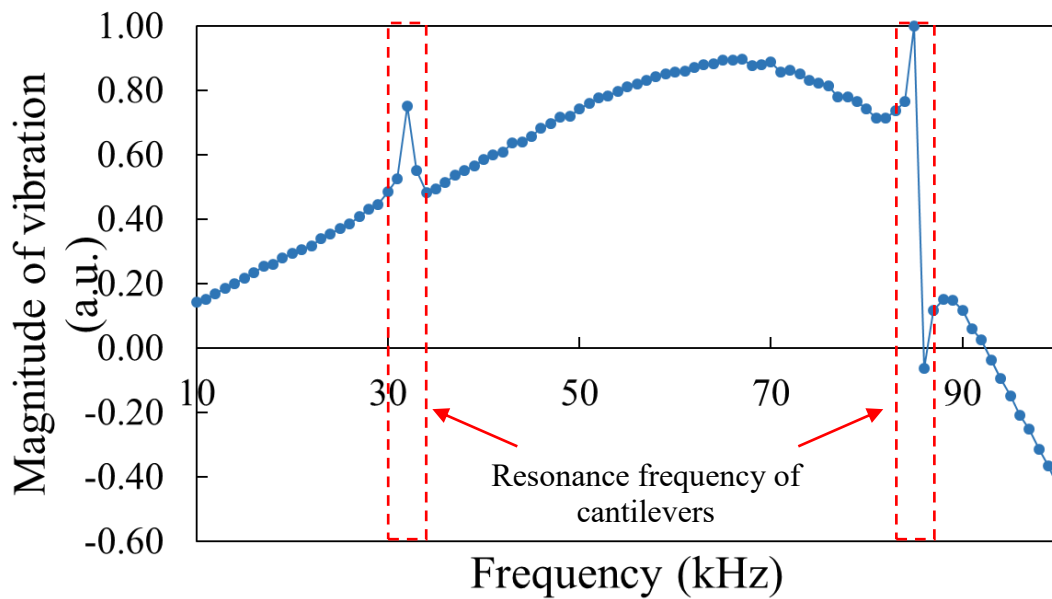


Figure 4.16. The vibration spectrum of the cantilever located on the sample.

The resonant frequency of the cantilever was the one parameter that should be considered because the signal from the resonant frequency was higher than the signal from the piezoelectric effect. Figure 4.16 was the vibration spectrum of the system. The peaks at 32 and 85 kHz were the resonant frequency of the ANSCM-PC cantilever. The resonant frequency of the model was reported around 11-18 kHz. The reason of the frequency shift was the interaction force between the cantilever tip and the sample. Then, the range of 35 to 80 kHz was from only piezoelectric signal and the response was maximum at 67 kHz.

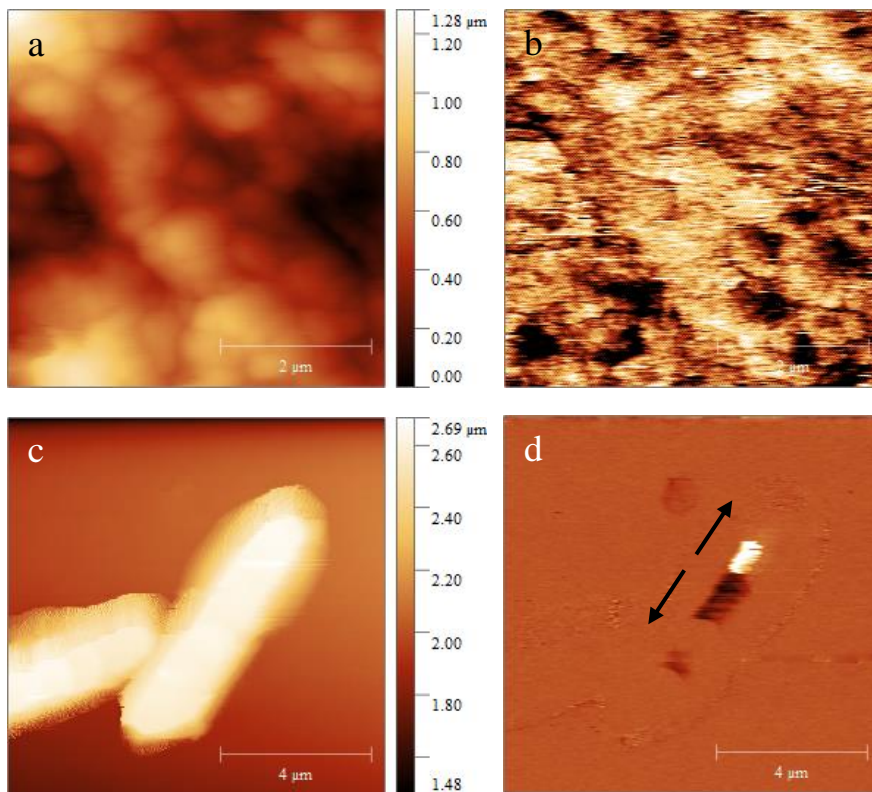


Figure 4.17. The observed a) topography image and b) PFM image of ZnO vertical aligned on the platinum coated silicon wafer. The observed c) topography image and d) PFM image of ZnO macrorods lied on the platinum coated silicon wafer. The bright and the dark represented the in-phase and out-off-phase of the PFM signal.

Figure 4.17 was the PFM image of ZnO. The prepared ZnO nanorods were piezoelectric property by without any post process, for example, stretching and poling processes. Most of piezoelectric signal for the vertical aligned ZnO nanorods were normal to the substrate. This confirmed that the growth of the ZnO by seeding method was in the c-direction. However, the result was different in the case of freestanding ZnO macrod. The two direction of dipole moment were observed in a single nanorod. This indicated that the expansion of nanorod was in two direction (Bdikin *et al.* 2010).

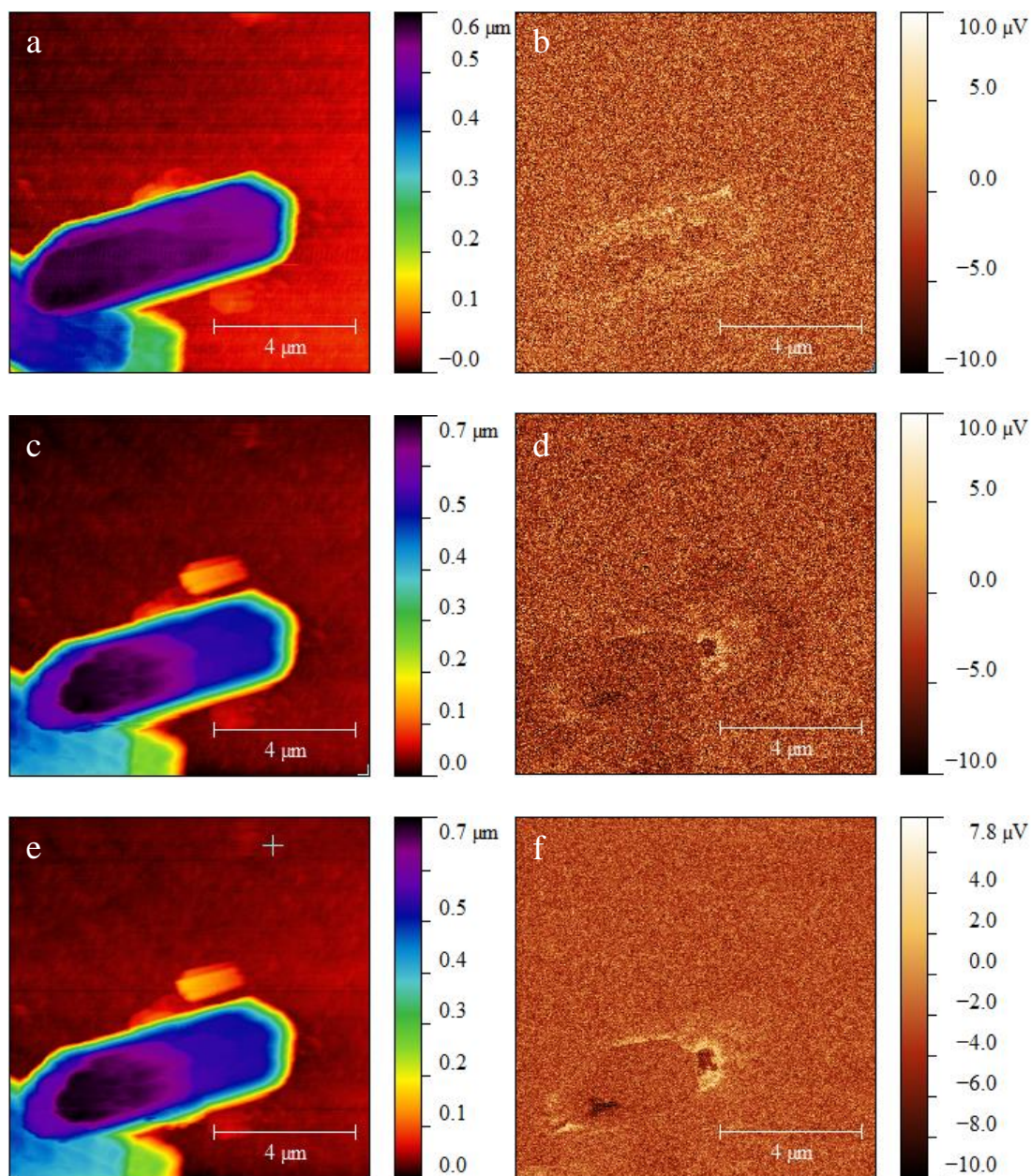


Figure 4.18. The observed topography and PFM images of ZnO macrorod with activated voltage peak a) and b) 1 V, c) and d) 3 V, e) and f) 5 V.

The effect of activated voltage was observed in case of ZnO macrorods. The activated voltage was varied from 1 to 5 V as summarized in the figure 4.18. The PFM regime and the nanograin in microrod was clearly observed at high voltage. The topography image in figure 4.18e confirmed that the microrods was occurred by the alignment of nanorods. The results indicated that, oriented attachment process not only occurred in the beginning process of the crystal growth, but also occurred in the

classical growth phase. The nanorods with the same crystallography and orientation attracted each other to form the macroscale. In case of the growth is fixed on the substrate the growth will be occurred only in (0001) direction. This different to the free-standing growth, the (000 $\bar{1}$ ) of crystal was freely, resulted to two polarizations in the single rod.

#### **4.7 Conclusions**

AFM is a surface probing technique that useful in surface characterization. The surface topography in micro to nano-scale can be evaluated by the technique. In addition, the technique can apply to study the surface properties, for example, mechanical and piezoelectric properties.

In this work, effect of ZnO on the collagen film was tested via force-distance curve base on AFM instrument. Development of the young modulus was observed when the concentration of ZnO was increased. Other that, thermal stability of reinforced was also observed when the ratio of collagen: ZnO was 4:1.

Piezoelectric property of the prepared was observed by PFM mode. The method not only shown that the prepared ZnO nanorods was piezoelectric properties but also shown polarization direction of the material.

## CHAPTER 5

### MICROPOWER ENERGY HARVESTING

This chapter shows using of composite material ZnO/P(VDF-HFP) in energy harvesting application. The different shape and size of ZnO was investigated to obtain the optimal condition to develop the harvester device. The final harvester was able to generate the maximum power in microwatt.

#### 5.1 Introduction

PVDF polymer belong to energy harvesting field since the first invention was explored. Light weight, flexibility, ability to be formed into intricate shapes, and the highest piezoelectric coefficient in the polymer group was the keys of interesting. There were two main co-polymer that were frequency used as the harvester, trifluoroethylene (TrFE) and hexafluoropropylene (HFP). Piezoelectric coefficient  $d_{33}$  of P(VDF-TrFE) was greater than PVDF for 10 pm/V but the  $d_{31}$  was lower. While P(VDF-HFP) shown stronger both  $d_{31}$  and  $d_{33}$  (Neese *et al.* 2007). This made the co-polymer P(VDF-HFP) popular for the last decade (Sukwisute, *et al.* 2013).

There were several researches improved the performance of the copolymer by doping some material. Silver nanowire P(VDF-HFP) composite thin film increased harvesting power by 159% from P(VDF-HFP) film (Wu *et al.* 2014). ZnO was also used to develop the output voltage of P(VDF-HFP) from 0.12V to 2.8 V at 2 wt% (Parangusan *et al.* 2018). From the research, the content of ZnO enhanced the piezoelectric property of the polymer. However, the information of the shape and the size of the ZnO were still uncleared. This chapter aimed to investigate the effect of different shapes and concentrations of ZnO on P(VDF-HFP) properties. Either nano-spherical or -rod composite models were compared in this chapter.

## 5.2 Energy harvester and measurement setup

The preparation process of nanoparticles (NPs), nanorods (NRs) and microrods (MRs) was published in the publication number 2 (Phooplub and Muensit, 2018). NPs, NRs and MRs were added into the P(VDF-HFP) during thin film preparation process. After casting and drying process, the composite films were obtained. To activate the piezoelectric properties of the composite film, an amount of 70 MV/m at 100°C was used to align the polarization of the piezoelectric film.

The energy harvester was constructed as shown in figure 5.1.

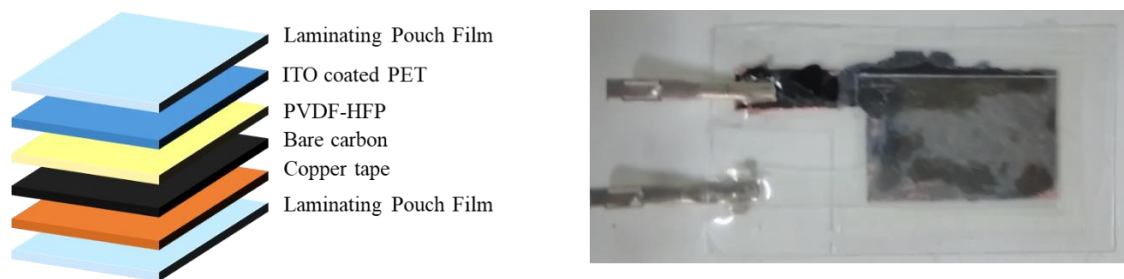


Figure 5.1. The structure of the energy harvester based ZnO P(VDF-HFP) nanocomposite (Phooplub and Muensit, 2018).

The energy harvester was tested the performance by the setup as shown in figure 5.2. The setup based on cantilever structure. The cantilever ( $135.0 \times 2.0 \times 0.5 \text{ mm}^3$ ) made of spring steel with hammer at the end was mounted on permanent magnet shaker (V201, LDS Test and Measurement, USA) that was controlled via function generator (DS340, Stanford Research System, USA). The vibration of cantilever was monitored by CMOS laser analogue sensor with controller (IA030, IA1000, KEYENCE, Japan). The cantilever was vibrated at 32 Hz along the experiment. The generated signals from piezoelectric polymer were recorded by USB data acquisition module (DAQ6002, Nation instrument, USA). All instruments were controlled via software in figure 5.3 with the source code as shown in figure 5.4.

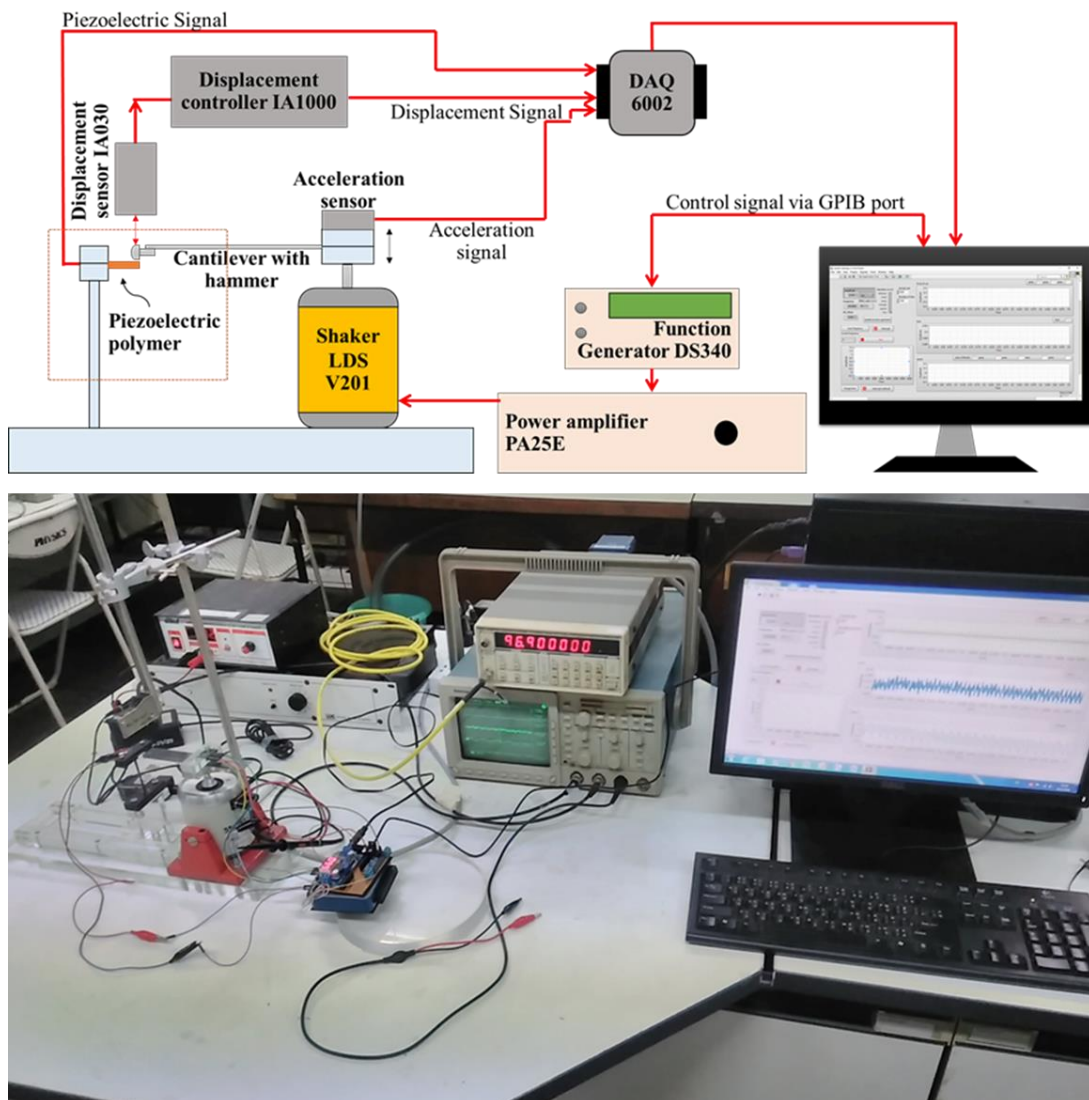


Figure. 5.2 The Energy harvesting setup.



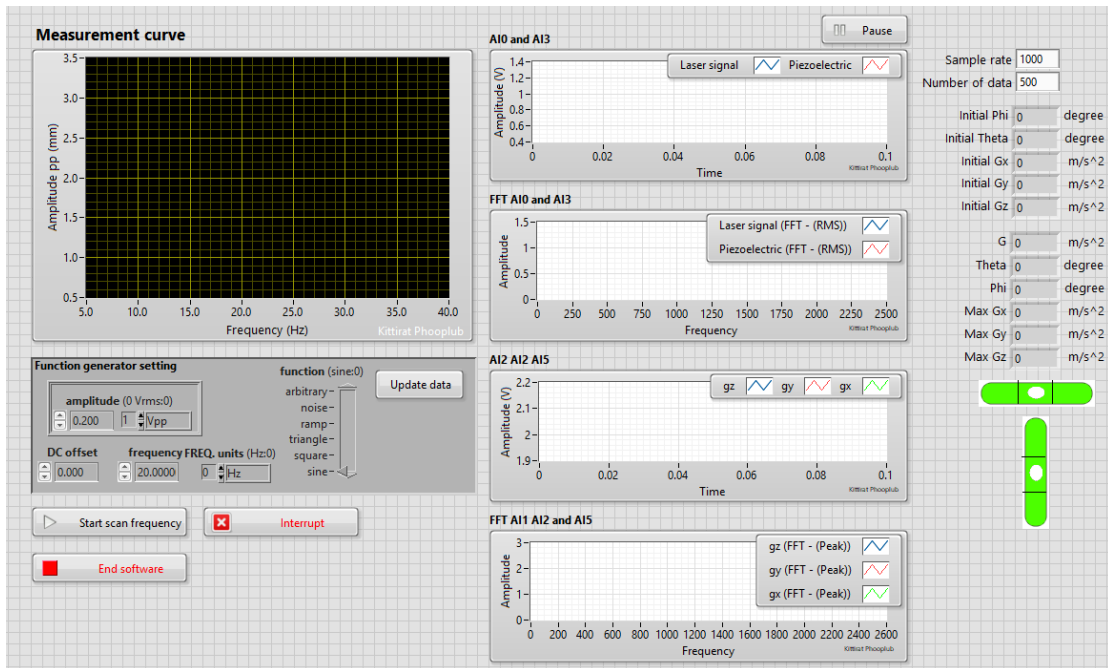


Figure. 5.3. The energy harvesting software.

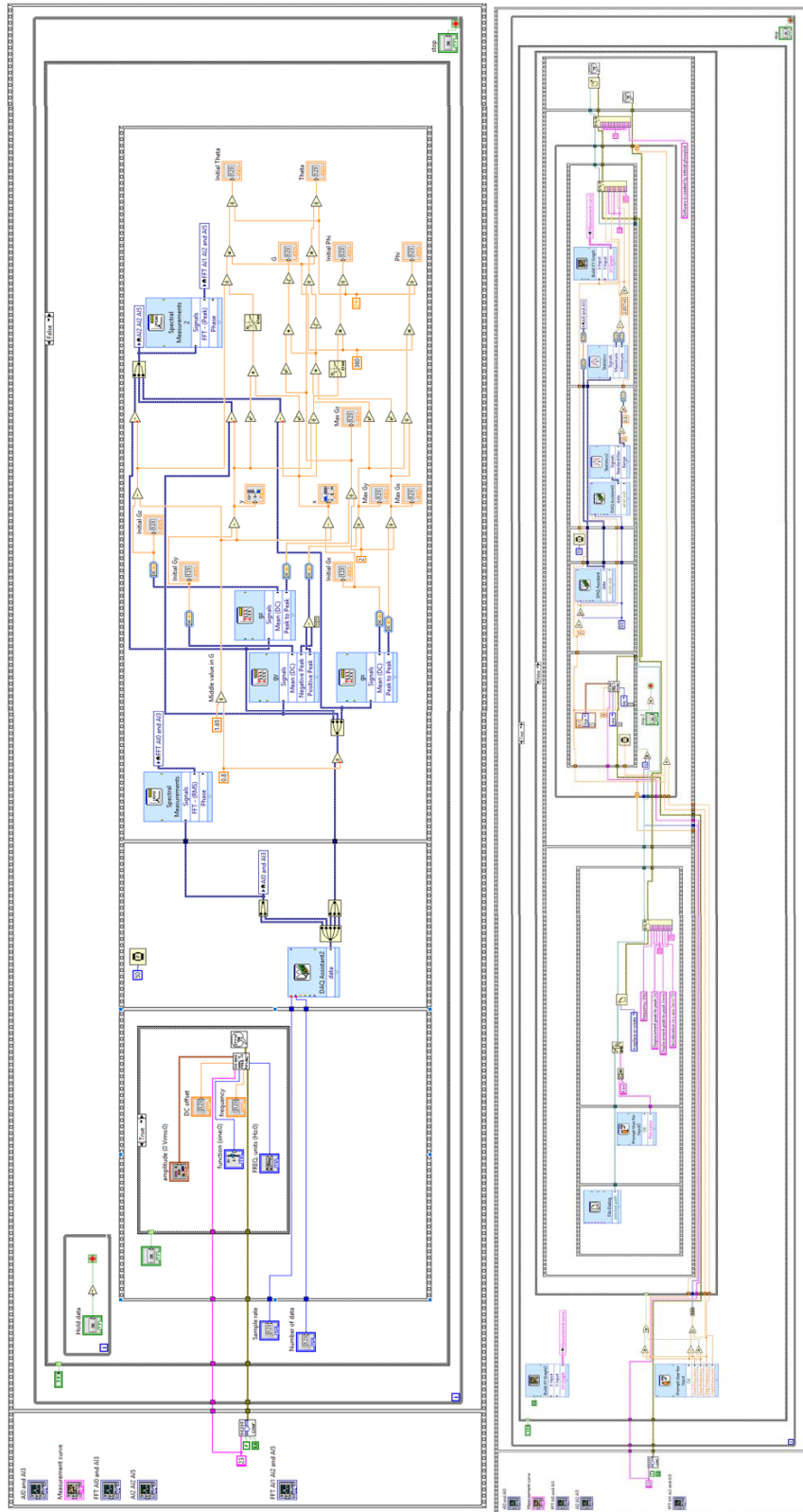


Figure 5.4. The LabVIEW source code for energy harvesting observation.

### 5.3 Effect of shape and size of ZnO to the performance of energy harvester

The physical properties of each condition were listed in the table 5.1

Table 5.1. Material properties of P(VDF-HFP) with various concentrations of ZnO of different shapes (Phooplub and Muensit, 2018)

P(VDF-HFP)		Crystallinity (%)	Electroactivity	Young's Modulus (GPa)
ZnO	Concentration (wt%)			
-	0	46.21	0.34	$1.89 \pm 0.30$
	1	46.21	0.47	$2.66 \pm 0.60$
NPs	2	46.38	0.54	$2.68 \pm 0.67$
	3	46.02	0.49	$1.80 \pm 0.25$
NRs	1	46.09	0.49	$3.24 \pm 0.36$
	2	46.26	0.51	$3.36 \pm 0.39$
	3	46.23	0.49	$2.57 \pm 0.33$
MRs	1	47.58	0.48	$3.16 \pm 0.32$
	2	47.98	0.43	$4.43 \pm 0.70$
	3	48.04	0.39	$3.42 \pm 0.41$

The resulted from the table 5.1 shown the effect of increasing of ZnO to the crystallinity of the P(VDF-HFP). At the low concentration, the apparent of ZnO enhanced the crystallinity of the P(VDF-HFP). When the concentration of ZnO more than 2 wt%, the crystallinity of the composite film was decreased. The electroactivity that was the  $\beta$ -phase fraction evaluate from FT-IR and young's modulus shown the same trend. This because the concentration 3 wt% caused the agglomeration of the particles.

To evaluate the performance, the harvester was mounted on to the setup in Figure 5.2. The shaker was set to reach the acceleration at 15 g with amplitude of vibration at the hammer for 0.8 cm at the 32Hz frequency. The open circuit voltage output of each sample was summarized in figure 5.6a. The optimum condition was 2, 3 and 4 wt% for NRs, MRs, and NPs, respectively. NRs showed enhancement of voltage output for 170%. The reason the NRs obtained the higher performance when compared with others was because the NRs had more surface area than MRs. In addition, the electroactive phase of NRs was higher than the others. The NRs 2 wt% enhanced the maximum power from 0.349 to 1.119  $\mu\text{W}$ . Other that, the optimum resistance was also reduced from 2 M $\Omega$  to 700 k $\Omega$  as seen in figure. 5.6b.

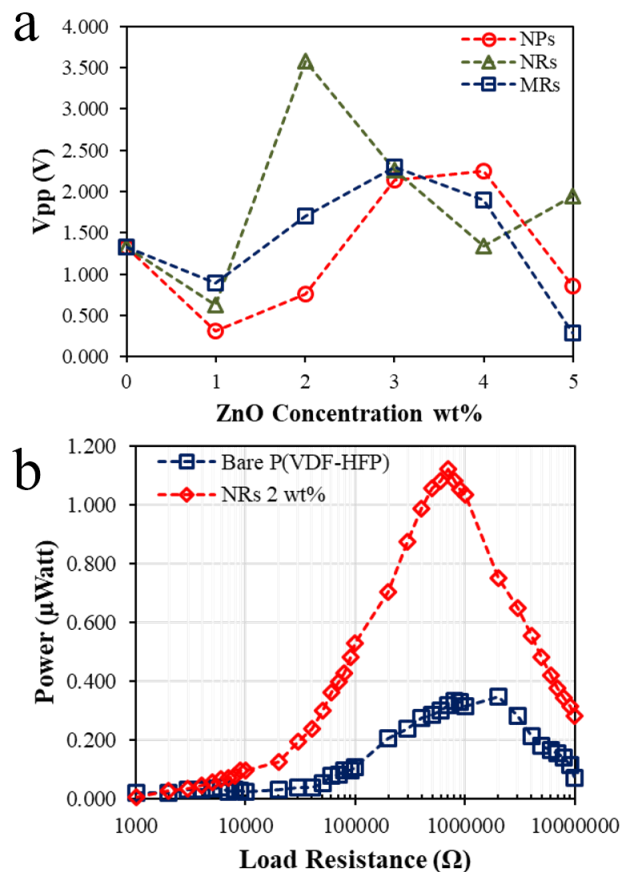


Figure. 5.5 Curves of a) Open-circuit voltage output with different concentrations and forms of ZnO b) Obtained power with respect to the load resistance compared between bare P(VDF-HFP) and P(VDF-HFP) with 2 wt% NRs ZnO (Phooplub and Muensit, 2018).

The possibility to implement the nanocomposite film was tested with commercial energy harvesting circuit LTC3588-1 (Linear Technology). The operation voltage of the circuit was set to 1.8 V. The signal generated by 2wt% NPs appeared after bridge rectifier circuit as seen in Figure. 5.6 but could not activate the buck-boost converter circuit which resulted to disappear of the signal at the output. This contrasted to piezoelectric PZT that could activate able to supply all parts of the circuit board. However, the level of the generated voltage was able to use as a trigger to wake up the extreme low power microcontroller PIC16LF1455 (Microchip, USA) which took the power consumption for 25 nW. This will be beneficial for the use of alarm system for unexpected vibration, for example, earthquake.

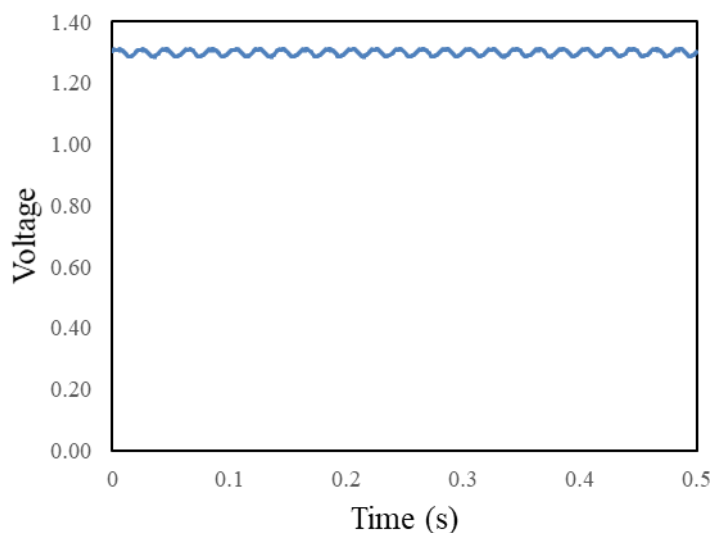


Figure 5.6. Piezoelectric signal of 2 wt% NRs condition after rectified.

#### 5.4. Conclusion

Mechanical, electrical and electromechanical properties are necessary for energy harvesting application. The configuration and concentration of ZnO to P(VDF-HFP) were tested to evaluate the possibility in the application. ZnO showed an enhancement of all properties of the P(VDF-HFP) at low concentration. MRs showed the best mechanical reinforcement, while NPs showed slightly better electroactive phase and dielectric properties. However, electroactive phase of P(VDF-HFP) was

dropped at higher ZnO concentration. In application of energy conversion by means of piezoelectric generator, NRs showed the highest performance to convert mechanical strain to electrical voltage. This is due to the higher surface area than MRs, that directly affected the induced internal strain, and better performance in terms of reinforcement than NPs. The better condition of NRs was found at 2wt%. The generated power could be enhanced by filled NRs to the output power 170% which was enough to activate low power electronic devices.

## CHAPTER 6

### CONCLUSIONS

This work has predicted by using the Finite Element Analysis for the ZnO nanorods and nanobelt that can effectively deliver the captured surrounding energy to convert into useful energy. Then ZnO nanorods have been successfully synthesised by hydrothermal reaction and possess the wurtsite phase as characterized by the XRD.

In the field of smart polymers, ZnO of different forms, i.e. nanoparticles (NPs), nanorods (NRs), and microrods (MRs) has been incorporated into a matrix of PVDF. After the polymer has been activated by the poling field of 70 MV/m at 90°C for 10 min, the ZnO has slightly changed the degree of crystallinity of the polymers and clearly increased the elasticity to the best value in the case of inserted MRs. P(VDF-HFP) reinforced with ZnO of 2 wt% NRs shows the best performance as a microsource of the energy of about 1  $\mu$ W.

For the insertion of ZnO into Collagen type I, ZnO significantly develops Young's modulus from 9 GPa to 18 GPa and keep the collagen elastic against ambient temperature. Infinitesimal movements which are extremely hard to measure are able to observe in this work because of the PFM mode based on the AFM facility. Without such measurement setup it is hard to suggest that nanoscale ZnO is good candidate for collagen reinforcement which is crucial for tissue engineering technology.

Finally, the possibility of using synthesized ZnO nanomaterials which is piezoelectric has been demonstrated for energy capture process in the present work. Although the observed electrical energy is tiny when compared to other forms of renewable energy, however, it can possibly be delivered to some ultra-low power electronic devices, acting as bone growth accelerator and wound healing etc.

#### **Suggestions for future work**

Key points that can be further developed are 1) the level of surrounding energy source 2) energy transfer mechanism 3) piezoelectric materials themselves. If these are effectively fulfilled, the high-performance piezoelectric energy harvester can be obtained.

## References

- Ainsworth, BE. Haskell, WL. Herrmann, SD. Meckes, N. Bassett JR. DR., Tudor-Locke, C. Greer, JL. Vezina, J. Whitt-Glover, MC. Leon AS. 2011 Compendium of physical activities: a second update of codes and met values. *Medicine & Science in Sports & Exercise*. **43**(8):1575–81.
- Allen, JJ. Techet, AH. Kelso, RM. Smits, AJ. 2001 Energy Harvesting Eel. *14<sup>th</sup> Australasian Fluid Mechanics Conference*
- Baruah, S. Dutta, J. 2009. Hydrothermal growth of ZnO nanostructures. *Science and Technology of Advanced Materials*. **10**(1):013001
- Bateman, L. 1962 The Chemistry and Physics of Rubber-Like Substances. *Maclaren*
- Bdikin, I. Silibin, M. Ayouchi, R. Schwarz, R. Gavrilov, S. Gracio, J. Kholkin, A. L. 2010. Local electromechanical properties of ZnO thin films and micro crystals. *MRS Proceedings*, 1256
- Carlotti, G. Socino, G. Petri, A. Verona, E. 1987 Acoustic investigation of the elastic properties of ZnO films. *Applied Physics Letters* **51**(23):1889-1891
- Cui, S. Dai, Z. Tian, Q. Liu, J. Xiao, X. Jiang, C. Wu, W. Roy, VAL. 2016. Wetting properties and SERS applications of ZnO/Ag nanowire arrays patterned by a screen printing method. *Journal of Materials Chemistry C*. **4**(6): 6371-6379
- Degen, A. Kosec, M. 2000. Effect of pH and impurities on the surface charge of zinc oxide in aqueous solution. *Journal of the European Ceramic Society*. **20**(6) :667-673
- Deminets, LN. Kostomarov, DV. Kuzmina, IP. 2002. Chemistry and Kinetics of ZnO Growth from Alkaline Hydrothermal Solutions. *Inorganic Materials*. **38**(2) 124–131
- Emami-Karvani, Z. Chehrazi, P. 2012. Antibacterial activity of ZnO nanoparticle on Gram-positive and Gram-negative bacteria. *African Journal of Microbiology Research* **5**(12):1368-1373



- Fang, HB. Liu, JQ. Xu, ZY. Dong, L. Wang, L. Chen, D. Liu, Y. 2006. Fabrication and performance of MEMS-based piezoelectric power generator for vibration energy harvesting. *Microelectronics Journal*, **37**(11), 1280-1284.
- Fang, M. Liao, Q. Wang, J. Qin, L. Zhong, C. Zhang, D. 2018. Self-adaptive piezoelectric ceramic vibration system based on asymmetric piezoelectric cantilever for energy harvesting. *International Journal of Applied Ceramic Technology*. **15**(6):1268-1276
- Fortunato, M. Chandraiahgari, CR. Bellis, GD. Ballirano, P. Sarto, F. Tamburrano, A. Sarto MS. 2018. Piezoelectric effect and electroactive phase nucleation in self-standing films of unpoled PVDF nanofilm, *Nanomaterials*. **8**:743
- Gao, PX. Song, J. Liu, J. Wang, ZL. 2006. Nanowire piezoelectric nanogenerator on plastic substrates as flexible power sources for nanodevices. *Advanced Material*. **19**(1): 67-72
- Gao, PX. Wang, ZL. 2004. Substrate atomic-termination-induced anisotropic growth of ZnO nanowires/nanorods by the VLS process. *Journal of Physical Chemistry B*. **108**(23): 7534-7537
- Giannakopoulos AE. Suresh, S. 1999. Theory of indentation of piezoelectric materials *Acta Mater*. **47**:2153
- Greene, LE. Law, M. Goldberger, J. Kim, F. Johnson, JC. Zhang, Y. Saykally, RJ. Yang, P. 2003. Low-temperature wafer-scale production of ZnO nanowire arrays. *Angewandte Chemie International Edition*. **42**:3031–3034
- Greene, LE. Law, M. Tan, DH. Montano, M. Goldberger, JG. Somorjai Yang, P. 2005 Route to Vertical ZnO Nanowire Arrays Using Textured ZnO Seeds. *Nano Letters* **5**: 1231-1236.
- Hamada, T. Ito, A. Fujii, E. Chu, D. Kato, K. Masuda, Y. 2009. Preparation of single-crystalline ZnO film on ZnO-buffered  $\alpha$ -plane sapphire by chemical bath deposition. *Journal of Crystal Growth*. **311**: 3687-3691

- Harnack, O. Pacholski, C. Weller, H. Yasuda, A. Wessels, J M. rectifying behavior of electrically aligned ZnO nanorods. *Nano Letters*. **3**(8): 1097-1101
- Hong, S. Woo, J. Shin, H. Jeon, JU. Pak, YE. Colla, EL. Setter, N. Kim, E. No, K. 2001. Principle of ferroelectric domain imaging using atomic force microscope *Journal of Applied Physics* **89**:1377–1386
- Hu, Y. Zhang, Y. Xu, C. Zhu, G. Wang, ZL 2010 High-output nanogenerator by rational unipolar assembly of conical nanowires and its application for driving a small liquid crystal display. *Nano Letters*, **10**(12):5025–5031
- Huang, HM. Wu, Y. Feick, H. Tran, N. Weber, E. Yang, P. 2001. Catalytic growth of zinc oxide nanowire by vapor transport. *Advanced Material*. **13**(2):113-116
- Ikeda, T. 1990 Fundamentals of piezoelectricity, *Oxford Science*
- Israelachvili, JN. 2011. Intermolecular and surface forces. *Elsevier Inc.*
- Jeong, JS. Lee, JY. Investigation of initial growth of ZnO nanowires and their growth mechanism. *Nanotechnology*. **21**: 475603
- Jungk, T. Hoffmann, ´A. Soergel, E. 2008. Impact of the tip radius on the lateral resolution in piezoresponse force microscopy *New Journal of Physics*. **10** 013019
- Kalinin, SV. Bonnell, DA. 2002. Imaging mechanism of piezoresponse force microscopy of ferroelectric surfaces. *Physical Review B*. **65**:125408
- Karapetian, E. Sevostianov, I. Kachanov, 1999 Mag. Point force and point electric charge in infinite and semi-infinite transversely isotropic piezoelectric solids. *Philosophical Magazine B* **80**( 3)
- Khan, F. Sassani, F. Stoeber, B. 2014. Nonlinear behaviour of membrane type electromagnetic energy harvester under harmonic and random vibrations. *Microsystem Technologies* **20**(7):1323–1335.
- Kim, H. Priya, S. Stephanou, H. Uchino. K. 2007. Consideration of Impedance Matching Techniques for Efficient Piezoelectric Energy Harvesting.

*IEEE Transactions on Ultrasonics, Ferroelectrics, and Frequency Control* **54**:1851–9.

- Kumra, KM. Mandal, BK. Naidu, EA. Sinha, M. Kumar, KS. Reddy, PS. 2013. Synthesis and characterization of flower shaped zinc oxide nanostructures and its antimicrobial activity. *Spectrochimica Acta, Part A: Molecular and Biomolecular Spectroscopy*. **104**:171–174.
- Lebedev, NN. Skal'skaya, IP. Ya., S. 1966. Uflyand, Problems in Mathematical Physics *Pergamon*
- Lee, CY. Tseng, TY. Li, SY. Lin, P. 2003. Growth of zinc oxide nanowires on silicon (100). *Tamkang Journal of Science and Engineering*. **6**(2):127-132
- Lei, A. Xu, R. Borregaard, LM. Guizzetti, M. Tomsen EV. 2012. Homogeneity analysis of a MEMS-based PZT thick film vibration energy harvester manufacturing process. *Procedia Engineering*. **47**:554-557
- Leissa, AW. Qatu, MS. 2011. Vibration of Continuous Systems. *McGraw Hill Professional*
- Lifshitz, IM. Slyozov, VV. 1959. Kinetics of diffusive decomposition of supersaturated solid solutions. *Journal of Experimental and Theoretical Physics* **8**: 331–339
- Lifshitz, IM. Slyozov, VV. 1961. The kinetics of precipitation from supersaturated solid solutions *Journal of Physics and Chemistry of Solids* **19**: 35–50
- Liu, B. Zeng, HC. 2003. Hydrothermal Synthesis of ZnO Nanorods in the Diameter Regime of 50 nm. *Journal of the American Chemical Society*. **125** (15):4430–4431
- Marks Jr, SC. Odgren PR. 2002 Chapter 1 - Structure and Development of the Skeleton Bilezikian, JP. Raisz LG. Rodan GA. (ed.) *Principles of Bone Biology*. *Elsevier Inc.*
- Miao, P. Mitcheson, P. Holmes, A. Yeatman, E. Green, T. Stark, B. 2006 MEMS inertial power generators for biomedical applications. *Microsystem Technologies* **12**(10):1079–1083.

- Nakashima, K. Iwami, M. Hiraki, A. 1975. Low temperature diffusion of Au into Si in the Si(substrate)-Au(film) system. *Thin Solid Films*, **25**:423-430
- Neese, B. Wang, Y. Chu, B. Ren, K. Liu, S. Zhang, QM. Huang, C. West, J. 2007. Piezoelectric responses in poly(vinylidene fluoride/hexafluoropropylene) copolymers. *Applied Physics Letters*. **90**(24):242917
- Nye, JF. 1957. Physical Properties of Crystals Their Representation by Tensors and Matrices. *Oxford University Press*
- Ostwald, W. 1901. Blocking of Ostwald ripening allowing long-term stabilization *Zeitschrift für Physikalische Chemie*. **37**: 385–390
- Parangusan, H. Ponnamma, D. Al-Maadeed, MAA 2018. Stretchable Electrospun PVDF-HFP/Co-ZnO Nanofibers as Piezoelectric Nanogenerators. *Scientific Reports*, **8**(1)
- Penn, RL. Banfield, JF 1998. Imperfect oriented attachment: dislocation generation in defect-free nanocrystals. *Science* **281**(5379): 969–971
- Phooplub, K. Meesane, J. Muensit, N. 2018. Development of Young's modulus for collagen thin films reinforced with ZnO nanorods probed by Atomic force microscopy. *Biomedical Physics & Engineering Express* **4**(5): 055022
- Phooplub, K. Muensit, N. 2018. Electro-mechanical properties of poly(vinylidene fluoride-hexafluoropropylene) reinforced with zinc oxide nanostructure. *Micro&Nano Letters* **13**(8): 1063-1067
- Rahman, A. and Hoque, Md. E. 2013. Harvesting Energy from Sound and Vibration. *International Conference on Mechanical, Industrial and Materials Engineering 2013*.
- Rahman, Md A. Lee, BC. Phan, DT. Chung, GS. 2013 Fabrication and characterization of highly efficient flexible energy harvesters using PVDF–graphene nanocomposites. *Smart Materials and Structures*. **22**(8)

- Rivera, A. Mazady, A. Anwar, M. 2015. Optimized Growth of ZnO Nanowires and Nanorods Using MOCVD. *International Journal of High Speed Electronics and System*. **24**:1520014
- Roundy, S. Wright, PK. 2004. A piezoelectric vibration based generator for wireless electronics. *Smart Materials and Structures*. **13**:1131-1142
- Roundy, S. Wright, PK. Rabaey, JM. 2003 Energy scavenging for wireless sensor networks. *Springer*
- Sawai J, Igarashi H, Hashimoto A, Kokugan T, and Shimizu MJ, 1995 Evaluation of growth inhibitory effect of ceramics powder slurry on bacteria by conductance method. *Journal of Chemical Engineering of Japan*. **28**(3): 288-293
- Soergel, E. 2011. Piezoresponse force microscopy (PFM). *Journal of Physics D: Applied Physics*. **44**(46)
- Sukwisute, P. Muensit, N. Soontaranon, S. Rugmai, S. 2013. Micropower energy harvesting using poly(vinylidene fluoride hexafluoropropylene). *Applied Physics Letters*. **103**(6):063905
- Sultana, S. Miran, MS. Mollah, MYA. Rahman, M. 2008. Effect of solvent on the growth kinetics of zinc oxide nanoparticle. *Journal of Bangladesh Chemical Society*. **22**(2):129-138
- Sun, XM. Chen, X. Deng, ZX. Li, YD. 2003 A CTAB assisted hydrothermal orientation growth of ZnO nanorods. *Materials Chemistry and Physics*, **78**, 99–104
- Suwanboon, S. Amornpitoksuk, P. Muensit, S. 2010. Enhancement of Optical Bandgap and Luminescent Characteristics of One-dimensional ZnO Nanoparticles. *Journal of Ceramic Processing Research*. **11**(4): 419-424

- Tam, KH. Djurišić, AB. Chan, CMN Xi, YY. Tse, CW. Leung, YH. Chan, WK. Leung, FCC. Au, DWT. 2008. Antibacterial activity of ZnO nanorods prepared by a hydrothermal method. *Thin Solid Films*. **516**(18): 6167-6174
- Tiwari, V. Srivastava, G. 2016 Enhanced dielectric and piezoelectric properties of 0–3 PZT/PVDF composites. *Journal of Polymer Research* **23**:38
- Trolier-McKinstry, S. Muralt, P. 2004. Thin film piezoelectrics for MEMS. *Journal of Electroceramics* **12**(1–2):7-17
- Wagner, C. 1961. Theorie der Alterung von Niederschlägen durch Umlösen (Ostwald-Reifung) *Zeitschrift für Elektrochemie* **65**: 581–591
- Wagner, RS. Ellis, WC. 1964. Vapor-Liquid-Solid mechanism of single crystal growth. *Applied Physics Letters*. **4**(89):89-90
- Wang, ZL. Chen, J. Lin, L. 2015 Progress in triboelectric nanogenerators as a new energy technology and self-powered sensors. *Energy & Environmental Science* **8**(8):2250–2282.
- Wang, ZL. Song, J. 2006. Piezoelectric nanogenerators based on zinc oxide nanowire arrays. *Science*. **312**(5771): 242-246
- Webb, P. 1992. Temperatures of skin, subcutaneous tissue, muscle and core in resting men in cold, comfortable and hot conditions. *European Journal of Applied Physiology* **64**(5):471–476
- Williams, CB. Yates, RB. 1996. Analysis of a micro-electric generator for microsystems. *Sensors and Actuators A: Physical* **52**(1–3):8-11
- Wu, L. Huang, G. Hu, N. Fu, S. Qiu, J. Wang, Z. Ying, J. Chen, Z. Li, W. Tang, S. 2014. Improvement of the piezoelectric properties of PVDF-HFP using AgNWs. *RSC Adv*. **4**(68):35896–35903.
- Wu, L. Wu, Y. LU, W. 2005. Preparation of ZnO Nanorods and optical characterizations. *Physica E*. **28**: 76–82

- Wu, L. Yuan, W. Hu, N. Wang, Z. Chen, C. Qiu, J. Ying, J. Li, Y. 2014. Improved piezoelectricity of PVDF-HFP/carbon black composite films. *Journal of Physics D: Applied Physics* **47**(13)
- Yang, P. Yan, HQ. Mao, S. Russo, R. Johnson, J. Saykally, R. Morris, N. Pham, J. He, RR. Choi, HJ. 2002. Controlled growth of ZnO nanowires and their optical properties. *Advanced Functional Materials* **12**:323-331
- Yang, R. Qin, Y. Li, C. Zhu, G. Wang, ZL 2009 Converting Biomechanical Energy into Electricity by a Muscle-Movement-Driven Nanogenerator. *Nano Letters*. **9**(3):1201-1205
- Yu, Q. Li, L. Li, H. Zhu, P. 2011. Synthesis and properties of boron doped ZnO nanorods on silicon substrate by low-temperature hydrothermal reaction. *Applied Surface Science*. **257**(14):5984-5988
- Zeng, YJ. Ye, ZZ. Xu, WZ. Zhu, LP. Zhao, BH. 2005. Well-aligned ZnO nanowires grown on Si substrate via metal–organic chemical vapor deposition. *Applied Surface Science*. **250**:280–282
- Zhao, MH. Wang, ZL. Mao, SX. 2004. Piezoelectric Characterization of Individual Zinc Oxide Nanobelt Probed by Piezoresponse Force Microscope. *Nano Letter* **4** (4):587–590
- Zhao, QX. Klason, P. Willander, m. 2007. Growth of ZnO nanostructures by vapor–liquid–solid method. *Applied Physics A*. **88**(1):27-30
- Zhou, M. Al-Furjan, MSH. Zou, J. Liu, W. 2018. A review on heat and mechanical energy harvesting from human – Principles, prototypes and perspectives. *Renewable and Sustainable Energy Reviews* **82**: 3582–3609

**APPENDIX**



**Publication I**

**Development of Young's Modulus for Collagen Thin Films Reinforced with ZnO  
Nanorods Probed by Atomic Force Microscopy**

**Phooplub K., Meesane J., Muensit N.**

Research Paper

## Biomedical Physics & Engineering Express



### PAPER

# Development of Young's modulus for collagen thin films reinforced with ZnO nanorods probed by Atomic force microscopy

RECEIVED  
14 May 2018

REVISED  
8 August 2018

ACCEPTED FOR PUBLICATION  
14 August 2018

PUBLISHED  
28 August 2018

Kittirat Phooplub<sup>1</sup>, Jirut Meesane<sup>2</sup> and Nantakan Muensit<sup>1,3</sup>

<sup>1</sup> Department of Physics, Prince of Songkla University, Songkhla, 90110, Thailand

<sup>2</sup> Biological Materials for Medicine, Faculty of Medicine, Prince of Songkla University, Songkhla, 90110 Thailand

<sup>3</sup> Center of Excellence in Nanotechnology for Energy, Prince of Songkla University, Songkhla, 90110 Thailand

E-mail: [nantakan.m@psu.ac.th](mailto:nantakan.m@psu.ac.th)

**Keywords:** collagen, AFM, tissue engineering, nanomaterial, elasticity, ZnO

### Abstract

Zinc Oxide (ZnO) nanorods have been prepared and proposed for collagen Type I reinforcement. The insertion of ZnO has been confirmed by an x-ray Diffraction pattern. A nano-indentation technique implemented through an Atomic Force Microscopy has been effectively handled to probe a mechanical behavior of soft tissue like collagen. Measurements at different temperatures for collagen thin films filled with different amounts of ZnO reveals that ZnO significantly develops Young's modulus from 9 GPa to 18 GPa. Without ZnO, the temperature increment leads to the dehydration of pure collagen while the reinforced ones were still elastic for cell growth. ZnO-reinforced collagen has, therefore, been improved both inherent rigidity and its stability against ambient temperature. The finding in this work suggests that nanoscale ZnO is good candidate for collagen reinforcement which is crucial for tissue engineering technology.

### 1. Introduction

Development of a synthetic scaffold to mimic extracellular matrix (EMC) for a particular cell is a mature rule in tissue engineering. The synthetic EMC acts as a temporary house with a desirable chemical and mechanical support for cell growth and tissue regeneration [1]. Owing to most organic tissues consists of collagen, collagen-based scaffold has been attractive in the field of tissue engineering for years. A triple helical of tropocollagen (length of 300 nm and diameter of 1.5 nm) with residue side-chain allows the molecule construction to a complex structure not only fibril network but also 3-dimensional hydrogel [2].

Generally, a scaffold has no inherent rigidity and has potential for antigenicity [3]. Enhancement of antibacterial function is necessary and incorporating with inorganic materials has been promoted. Amongst metal oxide dopants, ZnO is popular for antimicrobial activity on a broad spectrum of bacteria and, therefore, often used in tissue engineering [4–7]. The activity is effective when nanomaterial is incorporated due to a higher active area [8].

Nanostructures of ZnO are prepared by several methods, for example, vapor-liquid-solid (VLS) [9],

metalorganic chemical vapour deposition (MOCVD) [10], chemical method [11]. Chemical method is preferred due to its operation at low temperature and the structure of ZnO is controlled via concentration of reagent and capping agent [11]. The size of ZnO is also reduced by using low polarity solvent, for example alcohol [12]. However, a scaffold derived from reinforced collagen likely changes in its mechanical properties, in particular, elastic modulus [13]. The mechanical stability of reinforced scaffold is affected by the denatured temperature of a collagen which is close to human-body temperature [14, 15]. ZnO-reinforced collagen whose mechanical properties has been rarely investigated is, in turn, focused in this work. In particular, the elastic modulus at temperatures below and close to a temperature of cell environment has been studied with an only chosen methodology, i.e., nano-indentation via the use of Atomic Force Microscope (AFM). This is because conventional techniques based on direct manipulation and visual observation to determine the mechanical properties are not applicable to coated films, thin film on substrate fibrils of nanoscale dimensions. A few techniques have been reported to accommodate the nanoscale measurements such as direct tensile tests with a microelectromechanical system [16], three-point bending tests of a

suspended fiber [17]. For an AFM, it is a surface probing technique to impose a load by moving a cantilever with a sharp tip at its end to approach and retract on very small scale area [18] whereas a nano-indenter apparatus is capable of extended nanomechanical experiments for elastic analysis of biological materials [19]. Previous work on adapted indenter-AFM instrument is, for example, collagen fibril attached between the surface and a tip of an AFM [18], soft tissue collagen-chitosan [20], and living cells [21]. Nano-indentation based AFM thus offers an indentation force-distance data observed by AFM to correlate with the extracted elastic property of soft tissue on a stiff substrate as carried out in this work.

## 2. Materials and methods

### 2.1. Preparation of reinforced collagen thin film

The collagen was originated from calf skin (Sigma Aldrich). It was dissolved in acetic acid for  $1 \text{ mg mL}^{-1}$  at room temperature and left for 3 h to be a stock. The ZnO nanorods were prepared accordingly to the method of Harnack [22]. The crystallization of ZnO was observed by the Transition Electron Microscope (TEM, JEOL JEM-2010, Japan) that the particles were dropped on a formvar coated copper grid. Crystal structure of ZnO was confirmed by x-ray Diffractometer (X'Pert MPD, PHILIPS, Netherlands). The experimental peak positions were compared with the standard JCPDS files and the Miller indices were indexed to the peaks. The stock of collagen was diluted in the phosphate buffer to  $100 \mu\text{g mL}^{-1}$  and mixed with the nanorods at of the 1, 2.5, 5, 10, 25, 50, 75,  $100 \mu\text{g mL}^{-1}$  concentration before being dropped on a clean glass substrate. The mixture was kept at  $4^\circ\text{C}$  for 15 h to let the collagen fibrils complete their formation. The coated glasses were rinsed with deionized water several times and dried in an incubator at room temperature.

### 2.2. Topography observation

For topography observation, the AFM was working with tapping mode with 1–0.3 Hz line scan with 30% setpoint to get the information at low roughness and to make sure that the tip and the sample did not contact to each other. The spring constant of the used point-probe A-CLA (AppNano, USA) was approximately  $54 \text{ N m}^{-1}$  with  $<10 \text{ nm}$  tip radius. The force-displacement was performed in spectroscopy mode with  $0.33 \text{ nm}$  in Z scanner direction. The force volume ( $10 \times 10$  points) were acquired on an area of  $20 \times 20 \mu\text{m}^2$  each. The measurement on the homogeneous material before and after experiment was performed to make sure that the physical properties of cantilever tip had no sensible change.

### 2.3. Nano-indentation measurement

Elastic modulus was evaluated by using nano-indentation technique through an AFM (Nanosurf

Easyscan2, Nanosurf) and fitting the obtained force-distance curve to Hertz's theory. For the force-distance relationship, the cantilever was approaching to and withdrawing from the sample with constant moving step and the deflection is recorded corresponding to the moving that is known as a force-distance curve. The curve is roughly divided into three parts: (i) the zero line, the tip is located far away from the sample; (ii) the jump to contact, the position that the interaction between the tip and the sample is suddenly occurred that is induced by attractive forces; (iii) the contact line, the regime that the cantilever is bent according to the stiff of the sample. The third zone is used to analyse the mechanical property of the material.

In the case of a stiff sample, the deformation  $D$  is assumed by subtraction of piezo-displacement  $Z$  and the deflection  $\delta$ . The force exerted by the cantilever was given by the Hooke's law,  $F = -k_c \delta$ . Principally, Young's modulus of a material is able to calculate by using Hertz contact mechanics theory [22]. According to nano-indentation based technique, it requires no sample preparation prior to mechanical testing such as tension test for which dogbone samples must be cut or machined. The adapted technique is, however, not capable to represent a post-yield behavior although the collagen is elastic. The infiltration of ZnO to enhance the stiffness is investigated in this work, but its correlation to the post-yield mechanical behavior is still unsolved. In order to quantify nanomechanical properties for all the collagen samples, an isotropic assumption is used. The tip apex is assumed to be a half sphere and the adhesion force between the contact area is neglected. The limitation of the present technique is depended on the maximum force/depth range, material dimension and probe geometries [19]. Hence, the contact geometry is assumed to be axisymmetric, smooth and continuous. The contact radius ( $a$ ) according to the theory is given as

$$a_{\text{Hertz}} = \left( \frac{RF}{K} \right)^{1/3} \quad (1)$$

where  $R$  is the tip radius and  $K$  is the reduced elastic modulus given by

$$\frac{1}{K} = \frac{3}{4} \left( \frac{1 - \nu_i^2}{E_i} + \frac{1 - \nu_s^2}{E_s} \right) \quad (2)$$

$E$  and  $\nu$  in (2) are Young's modulus and Poisson's ratio, respectively. Subscript  $i$  and  $s$  are referred the indenter and sample, respectively. When  $E_i \ll E_s$ , particularly in the case of silicon AFM tip and biological sample, the reduced modulus can be approximated in the form

$$\frac{1}{K} = \frac{3}{4} \left( \frac{1 - \nu_s^2}{E_s} \right) \quad (3)$$

For very small indentations the contact radius  $a$  can be rewritten as  $\sqrt{RD}$ . Mathematical fitting of (2) is suitable for bulk film, for example, glass or thick film polymer. In the case of multilayer thin film, the relation between  $D^{3/2}$  and  $F$  is not linearity. Several

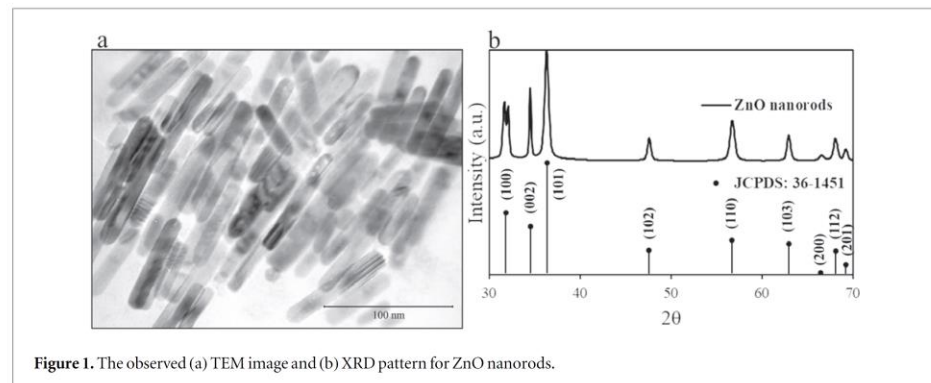


Figure 1. The observed (a) TEM image and (b) XRD pattern for ZnO nanorods.

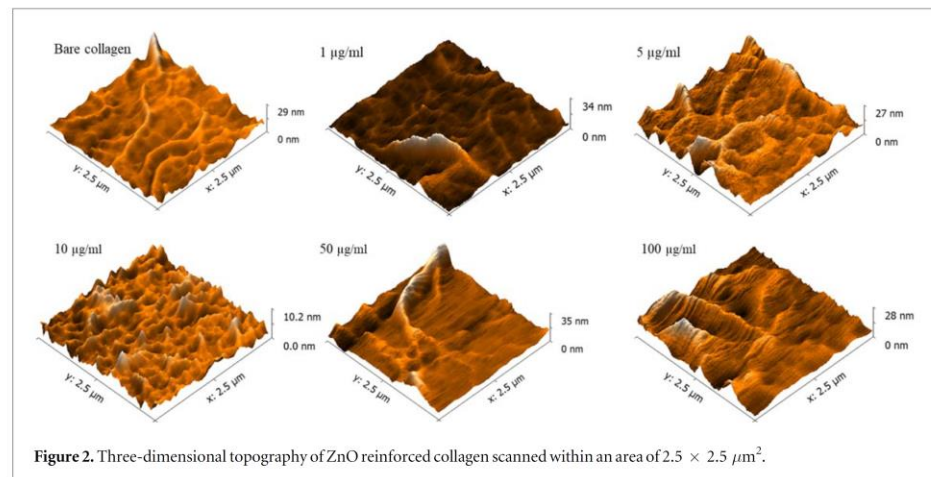


Figure 2. Three-dimensional topography of ZnO reinforced collagen scanned within an area of  $2.5 \times 2.5 \mu\text{m}^2$ .

researchers have paid attention to improve the model to match the data. Doener and Nix [23] have described the calculation of reduced elastic moduli of the double layer system by application of weighting factor,  $\exp(-\alpha t/D)$ . The parameter  $\alpha$  is used by means of interactions at the interfaces. For reduced elastic modulus, Gao [24] has used the vibrational theory to determine the mechanical property. The weighting function of Gao is depended on two parameters, the thickness of the material layer and the Poisson's ratio. However, the presence of exponential and too many arbitrary parameters are quite complicated to evaluate the reduced elastic modulus. The function proposed by Cappella is chosen in this work [25]. The force-displacement curve at the contact zone is divided by two regimes, the polymer and the substrate regimes. The fitting  $D^{3/2}$  function is yielded by the combination of the two regimes that is

$$D_2^3(\delta) = (\beta F - \epsilon) + \sqrt{\alpha^2 F^2 - 2\epsilon(\beta - \gamma)F + \epsilon^2} \quad (4)$$

The first term is corresponded to the deformation dominated by the substrate while the square root term

is the sample's deformation. At the contact point, (4) is reduced to  $\alpha\delta$  that  $\alpha$  is the slope at the sample zone. When (4) is taken the limit to infinity value, it becomes

$$(\beta + \alpha) \left[ F - \frac{\epsilon}{\alpha} \left( 1 - \frac{\gamma}{\beta + \alpha} \right) \right]. \quad \text{An intersection}$$

between two limits is occurred at  $F_c = \frac{\epsilon}{\alpha}$  that is used to determine the interaction between the sample and the substrate. In the case of  $F \ll F_c$ , the curve is in the sample zone, while the reduced modulus at the  $F \gg F_c$ , is dominated by the substrate. The reduced elastic modulus of the sample is obtained from the slope of the asymptotes at the sample zone from

$$\alpha = \frac{k_c}{\sqrt{RK}} \quad (5)$$

From (5),  $K$  is obtained and (3) is then used to evaluate the Young's modulus of the sample.

### 3. Results and discussion

Figure 1 shows the morphology of ZnO after 3 days of 11 nm in diameter and 63 nm in length. Crystallization

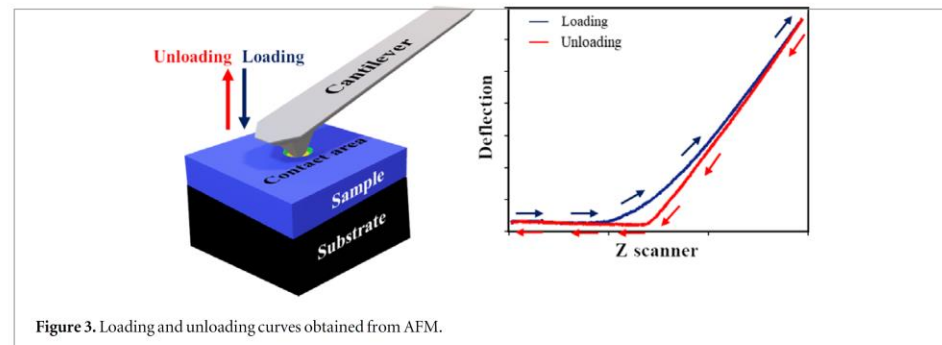


Figure 3. Loading and unloading curves obtained from AFM.

consisted of two processes: nucleation growth and oriented attachment. In the beginning, nucleation was occurring via co-precipitating of two salt species resulted to appear of ZnO nuclei. ZnO in the solution was adsorbed to the nuclei that affected the size increasing. Due to the nucleation growth is an entropic driven process, the crystals with lower size than the average value in the solution were dissolved as a bulk solution and adsorbed by the bigger size. The particles were attached each other to form nanorods [

27]. The XRD pattern of the ZnO prepared was shown in figure 1(a). All the peaks, at 31.82, 34.54, 36.42, 47.59, 56.71, 62.92, 66.47, 68.10, and 69.22 corresponding to the (100), (002), (101), (102), (110), (103), (200), (112), and (201) crystalline planes confirmed that the synthesized materials were ZnO with wurtzite phase. The diffraction peaks agreed well with the JCPDS data, confirming that there are no any other characteristic peaks other than ZnO. In order to calculate the crystalline size ( $D$ ) of the prepared powder, the value of full width at half maximum (FWHM) for the obtained diffraction peaks was used in the known Debye–Scherrer equation following

$$D = \frac{K\lambda}{\beta \cos \theta} \quad (6)$$

where  $K$ ,  $\lambda$ ,  $\beta$  and  $\theta$  are the shape factor, the x-ray wavelength, FWHM of the diffraction peak and the Bragg diffraction angle, respectively. The estimated particle size using Debye–Scherrer equation for all recorded diffraction lines emerges that the investigated ZnO powder in nano-size is 14 nm for the maximum peak at (101) and 35 nm at (002) that corresponds to the length of nanorods [26].

By using the tapping mode the images were taken by 35% of the amplitude of vibration and 0.15 to 0.25 Hz for line scan, and with a 0.34 nm resolution of z scanner. The images of all dried specimen taken from the mixture were as shown in figure 2.

Each collagen unit,  $(\text{Gly-X-Y})_n$  chains and  $n$  is 337–343, is normally 5 nm in diameter and 300 nm in length. From figure 2, without ZnO the fibril collagen with an average diameter of  $127 \pm 24$  nm and a root mean square roughness of 7.8 nm was observed. The

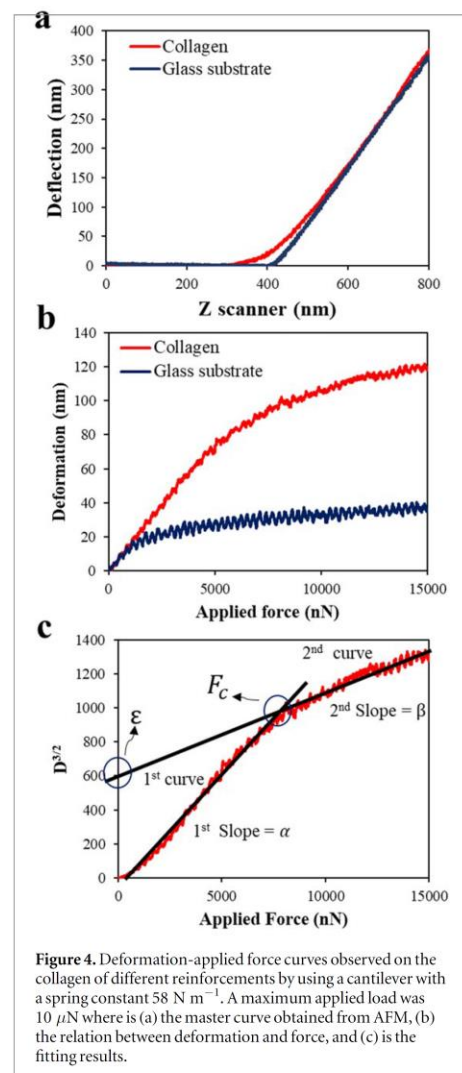
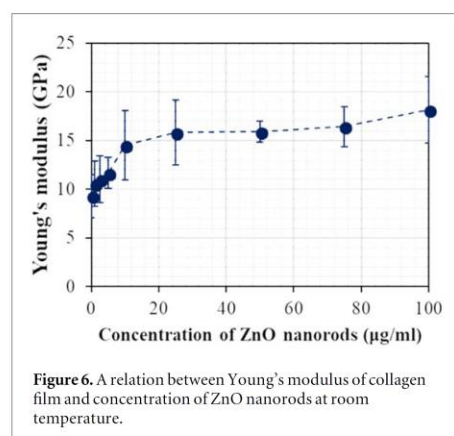
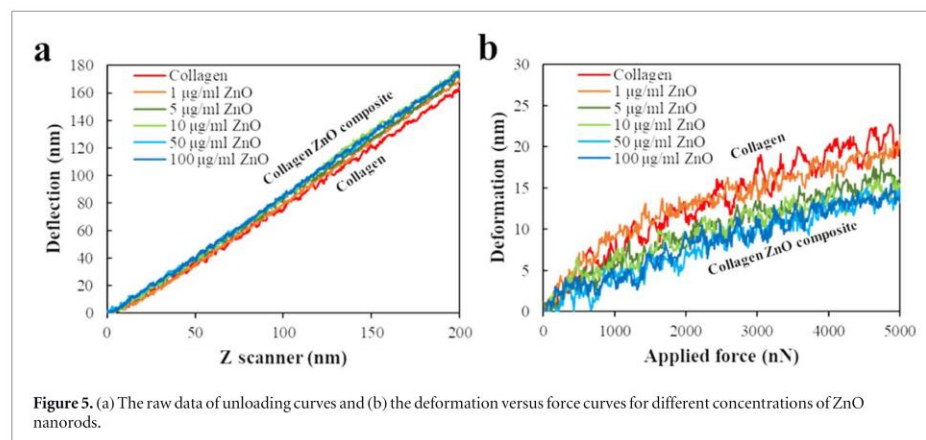


Figure 4. Deformation-applied force curves observed on the collagen of different reinforcements by using a cantilever with a spring constant  $58 \text{ N m}^{-1}$ . A maximum applied load was  $10 \mu\text{N}$  where is (a) the master curve obtained from AFM, (b) the relation between deformation and force, and (c) is the fitting results.

collagen fibril was getting larger with its largest roughness only at the lowest ZnO: collagen ratio. The collagen unit-collagen unit and the collagen unit-substrate



interactions played an important role for fibril formation in the mixture. Hydrogen bonds at the terminal of the collagen let the collagen bond each other while the charge of the molecule affected the collagen-substrate interaction. The ion in the solution, in particular, potassium ions, resulted in a decrease in charge affinity of the collagen molecules toward their surface [27]. Then, the collagen molecule was favored to bond each other in the solution than to the glass surface. The following investigations were carried out at a room temperature of 23 °C. The AFM tip was approached the reinforced collagen with measurement frequency 0.2 Hz scan interval time of 4 s at 0.34 nm/step. The measurement was also done at 1.0 Hz and showed no difference of the obtained data. The force-displacement curve which is a relation between the force exerted by the cantilever tip and the deformation of the sample obtained after a calibration. The sensitivity, which is a relationship between an electrical signal from photodiode and the deflection of the

cantilever was calibrated by approaching the cantilever onto a certain sample, i.e., a glass slide. The obtained sensitivity of the measurement was  $7.80 \times 10^{-7} \text{ m V}^{-1}$ .

Figure 3 shows the loading and unloading curves obtained from the AFM measurements. The loading curve indicated the deflection when the cantilever was approached to the sample while the unloading was obtained during withdrawal processes. In the case of deep indentation (tip radius  $\ll$  indentation depth), the loading curve possibly affect both elastic and plastic deformations. The unloading curve is preferred because at the initial state the plastic deformation can be omitted [20]. The effect is clearly seen in figure 3 that the load and unloading results were not overlapping. Then the unloading was taken into account. Afterwards, a hundred of the force-displacement curves were collected from each film as shown in figure 4. Figure 4(a) shows the curve obtained from the instrument, plotting between the deflection of the cantilever and the movement of the cantilever in the Z axis. The curve for collagen film and glass slide were due to a difference in Young's modulus. The deflection of the cantilever was rapidly increased when the cantilever was close to the glass substrate. The collagen was slightly changed at the beginning and when the force exerted with the higher magnitude the curve became the same for both cantilever and glass. The deflection within this zone was only from the bending of the cantilever. After subtracting the displacement of the cantilever, the deformation of the sample was clearly obtained. The applied force plotted in figure 3(b) was evaluated and the relationship was found to obey the Hertz's theory. To determine the reduced modulus given in (4), the curve was substitutive with a plot of  $D^{2/3}$  and the force relationship as shown in figure 4(c). The curve with two zones in figure 4(c),  $F_c$  indicates the boundary between the collagen film

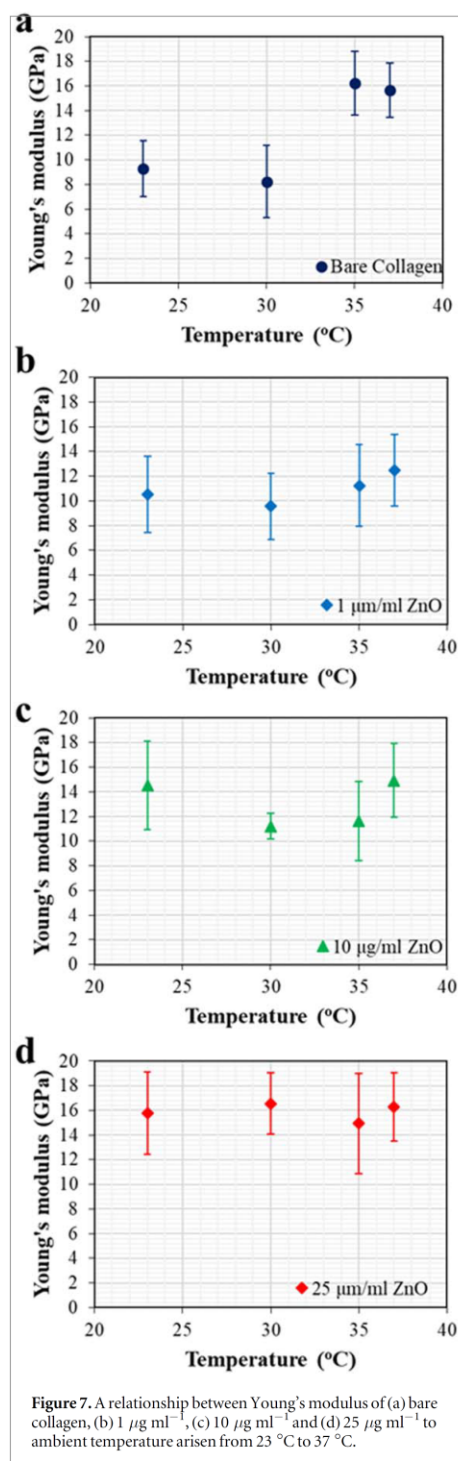
of the first layer zone (1th curve) and the substrate of the second layer zone (2nd curve). The slope in the first zone was used to calculate the reduced modulus of the collagen. By using (3) and the Poisson's ratio of 0.5 for the collagen samples as in the case of the polymer [20], Young's modulus was evaluated. Furthered study at higher temperature was carried out by the use of the thermoelectric Peltier module. The measurement was thermally kept at a constant temperature for an hour before probing the sample.

Referring to nanomechanical characterization using nano-indentation based AFM as mentioned earlier, instead of superimposing the stress-strain curves for the collagen of different reinforcements, the results were as shown in figure 5. In figure 5(b) each curve was derived from the raw data at the contact zone obtained from the AFM in figure 5(a). The curve with smaller slope in figure 5(b) was correlated to a stiffer sample. These indentation responses were repeatable and inferred to each other for with and without ZnO. Further increasing ZnO nanorods is beneficial to promote the stiffness but different collagen dimension is necessary. For given samples and probe geometry, an optimal maximum load was  $10 \mu\text{N}$  as seen in figure 4. Further applied load increment is able to cause the deformation of the substrate.

ZnO nanorods have taken part in the development of Young's modulus of collagen film as seen in figure 6. Initially, Young modulus's of collagen film was  $9.29 \pm 2.24 \text{ GPa}$ . Large scattered data was likely related to the collagen dimension with respect to the tip radius. When the collagen was large enough, the magnitude of errors was relatively low. Sources of errors possibly arisen from surrounding vibrations which was not completely isolated during the AFM operation.

Finally, the effect of surrounding temperatures on Young's modulus was done by using a thermal stage with a temperature sensor (TMP36, Analog Device, USA) directly glued on the sample. The force-distance curves were done at 23, 30, 35, and 37 °C. Based on the force-displacement approach the modulus was evaluated and plotted as a function of temperatures in figure 7.

Without ZnO, the temperature increments significantly affected Young's modulus of pure collagen. An increase from  $9.29 \pm 2.24 \text{ GPa}$  to  $16 \pm 2.24 \text{ GPa}$  was mainly caused by increasing temperature from 23 to 37 °C as seen in figure 7(a), resulting in the dehydration of the sample [20]. The reduction of water content in bone tissue has lead to an increase in Young's modulus. [28]. From figures 7(b) and (c), similar fluctuations of Young's modulus between 23 to 37 °C were found in the samples with relatively small ZnO concentration. When incorporation with  $25 \mu\text{g ml}^{-1}$  ZnO the value of about 16 GPa was smoothly observed for the mentioned temperature range. Further increasing ZnO concentration with respect to present collagen-substrate configuration was not recommended as discussed earlier. The



denaturation temperature ( $T_d$ ) for pure collagen is about 39 °C and the collagen incorporated with nanoparticles has been reported to shift the  $T_d$  to

higher temperature [29]. A similar trend was found when the collagen was reinforced with 10% Al<sub>2</sub>O<sub>3</sub> and there was a shift of T<sub>d</sub> from 39 to 43 °C [30]. The addition of ZnO nanorods thus keeps the collagen elastic through its wider range of temperature which is beneficial for wound healing [31].

#### 4. Conclusions

ZnO nanorods have been prepared and proposed for collagen Type I reinforcement. The insertion of ZnO has been characteristically confirmed by an x-ray Diffraction pattern. A nano-indentation technique implemented through the AFM was applicable for thin film like soft tissue on a stiff substrate. The force-distance relationships obtained from the collagen surface and the AFM tip were fitting to Hertz's theory to evaluate Young's modulus of the collagen. Young's modulus of pure collagen has been increased from 9 to 16 GPa with increasing temperature from 23 to 35 °C. With Zn addition, the value has been increased from 9 to 18 GPa. The findings in this work suggest that nanoscale ZnO is the good candidate for collagen reinforcement.

The authors would like to acknowledge the financial supports from the Royal Golden Jubilee PhD Program under Grant No. PhD/0034/2553, the Department of Physics, Center of Excellence in Nanotechnology for Energy (CENE), the Institute of Biomedical Engineering, Faculty of Medicine and the Graduate School, Prince of Songkla University, Hat Yai, Songkhla, Thailand. The authors are grateful to Prof. Dr Andrei L Kholkin, University of Aveiro, Portugal for his advice on the AFM technique.

#### ORCID iDs

Jirut Meesane  <https://orcid.org/0000-0002-6242-818X>

Nantakan Muensit  <https://orcid.org/0000-0003-3026-9687>

#### References

- [1] Migliarese C and Motta A 2013 Scaffolds for tissue engineering: biological design, materials, and fabrication (Singapore: Pan Stanford Publishing Pte. Ltd) pp 223–62
- [2] Gelse K, Pöschl E and Aigner T 2003 Collagens—structure, function, and biosynthesis *Adv. Drug. Deliv. Rev.* **55** 1531–46
- [3] Glowacki J and Mizuno S 2007 Collagen scaffolds for tissue engineering *Biopolymers*. **89** 338–44
- [4] Sawai J, Igarashi H, Hashimoto A, Kokugan T and Shimizu M J 1995 Evaluation of growth inhibitory effect of ceramics powder slurry on bacteria by conductance method *Chem Eng Jpn.* **28** 288–93
- [5] Sawai J, Shoji S, Igarashi H, Hashimoto A, Kokugan T, Shimizu M and Kojima H 1998 Hydrogen peroxide as an antibacterial factor in zinc oxide powder slurry *J. Femtosec. Stud. Rel.* **86** 521–2
- [6] Zhang L, Ding Y, Povey M and York D 2008 ZnO nanofluids—A potential antibacterial agent *Prog. Nat. Sci.* **18** 939–44
- [7] Shalumon K T, Anulekha K H, Nair Sreeja V, Nair S V, Chennazhi K P and Jayakumar R 2011 Sodium alginate/poly(vinyl alcohol)/nano ZnO composite nanofibers for antibacterial wound dressings *Int. J. Biol. Macromol.* **49** 247–54
- [8] Padmavathy N and Vijayaraghavan R 2008 Enhanced bioactivity of ZnO nanoparticles—an antimicrobial study *Sci. Technol. Adv. Mater.* **9** 035004
- [9] Zhao Q X, Klason P and Willander M 2007 Growth of ZnO nanostructures by vapor–liquid–solid method *Appl. Phys. A* **88** 27–30
- [10] Perillat-Merceroz G, Jouneau P H, Feuillet G, Thierry R, Rosina M and Ferret P 2010 MOCVD growth mechanisms of ZnO nanorods *J. Phys.: Conf. Ser.* **209** 012034
- [11] Baruah S and Dutta J 2009 Hydrothermal growth of ZnO nanostructures *Sci. Technol. Adv. Mater.* **10** 013001
- [12] Voigt M, Klaumunzer M, Tiem H and Peukert W 2010 Detailed analysis of the growth kinetics of ZnO nanorods in methanol *J. Phys. Chem.* **114** 6243–6
- [13] Kane R J, Weiss-Bilka H E, Meagher M J, Liu Y, Gargac J A, Niebur G L, Wagner D R and Roeder R K 2015 Hydroxyapatite reinforced collagen scaffolds with improved architecture and mechanical properties *Acta Biomaterialia* **17** 16–25
- [14] Yang L, Werf K O, Fittie C F C, Binnink M L, Dijkstra P J and Feijen J 2008 Mechanical properties of native and cross-linked type I collagen fibrils *Biophys. J.* **94** 2204–11
- [15] Bozec L and Odlyha M 2011 Thermal denaturation studies of collagen by microthermal analysis and atomic force microscopy *Biophys. J.* **101** 228–36
- [16] Eppell S J, Smith B N, Kahn H and Ballarini R 2006 Nanomeasurement with micro-devices: mechanical properties of hydrated collagen fibrils *J. Roy. Soc. Interface.* **3** 117–21
- [17] Xu W, Mulhern P J, Blackford B L, Jericho M H and Templeton I 1994 A new atomic-force microscopy technique for the measurement of the elastic properties of biological materials *Scanning Microsc.* **8** 499–506
- [18] Graham J S, Vomund A N, Phillips C L and Grandbois M 2004 Structural changes in human type I collagen fibrils investigated by force spectroscopy *Exp. Cell Res.* **299** 335–42
- [19] Constantinides G, Kalcioğlu Z, McFarland M, Smith J F and Van Vliet K J 2008 Probing mechanical properties of fully hydrated gels and biological tissues *J. Biomech.* **41** 3285–9
- [20] Zhu Y, Dong Z, Wejinya U C, Jin S and Ye K 2011 Determination of mechanical properties of soft tissue scaffolds by atomic force microscopy nanoindentation *J. Biomech.* **44** 2356–61
- [21] Thomas G, Burnham N A, Camesano T A and Wen Q 2013 Measuring the mechanical properties of living cells using atomic force microscopy *J. Vis. Exp.* **76** 50497
- [22] Hertz H and Reine J 1881 On the contact of elastic solids *Angew. Math.* **92** 156–71
- [23] Doerner M F and Nix W D 1989 A method for interpreting the data from depth-sensing indentation instruments *J. Mater. Res.* **1** 601–9
- [24] Gao H, Chiu C H and Lee J 1992 Elastic contact versus indentation modeling of multi-layered materials *Int. J. Solids Structures* **29** 2471–92
- [25] Cappella B and Silbernagl D 2007 Nanomechanical properties of mechanical double-layers: A novel semiempirical analysis *Langmuir* **23** 10779–87
- [26] Ocakoglu K, Mansour S A, Yildirimcan S, Al-Ghamdi A A, El-Tantawy F and Yakuphanoglu F 2015 Microwave-assisted hydrothermal synthesis and characterization of ZnO nanorods *Spectrochim. Acta A* **148** 362–8
- [27] Narayanan B, Gilmer G H, Tao J, Yoreo J J D and Ciobanu C V 2014 Self-assembly of collagen on flat surfaces: the interplay of collagen–collagen and collagen–substrate interactions *Langmuir* **30** 1343–50
- [28] Liever W B, Poljsak A S, Waldman S D and Pilkey A K 2010 Effects of dehydration-induced structural and material



- changes on the apparent modulus of cancellous bone *Med. Eng. Phys.* **32** 921–5
- [29] Srivatsan K V, Lakra R, Sai K P and Kiran M S 2016 Effect of bimetallic iron:zinc nanoparticle on collagen stabilization *J. Mater. Chem. B* **8** 1437–47
- [30] Mandal A, Farhan Md K and Sastry T P 2016 Effect of reinforced Al<sub>2</sub>O<sub>3</sub> nanoparticles on collagen nanobiocomposite from chrome-containing leather waste for biomedical applications *Clean Techn Environ Policy*. **18** 765–73
- [31] Paunica-Panea G, Fica A, Marin M M, Marin S, Albu M G, Constantin V D, Dinu Pirvu C, Vuluga Z, Corobea M C and Ghica M V 2016 New collagen-dextran-zinc oxide composites for wound dressing *J. Nanomater.* **2016** 5805034
- [32] Harnack O, Pacholski C, Weller H, Yasuda A and Wessels J M 2003 Rectifying behavior of electrically aligned ZnO nanorods *Nano Lett.* **3** 1097–101
- [33] Ethayaraja M and Bandyopadhyaya R 2007 Mechanism and Modeling of Nanorod Formation from Nanodots *Langmuir* **23** 6418–23

**Publication II**

**Electro-mechanical properties of poly(vinylidene fluoride-hexafluoropropylene)  
reinforced with zinc oxide nanostructure**

**Phooplub K., Muensit N.**

Research paper

## Electro-mechanical properties of poly(vinylidene fluoride-hexafluoropropylene) reinforced with zinc oxide nanostructure

Kittirat Phooplub<sup>1,2</sup>, Nantakan Muensit<sup>1,2</sup> ✉

<sup>1</sup>Department of Physics, Faculty of Science, Prince of Songkla University, Songkhla 90110, Thailand

<sup>2</sup>Center of Excellence in Nanotechnology for Energy (CENE), Prince of Songkla University (PSU), Hat Yai 90112, Thailand

✉ E-mail: nantakan.m@psu.ac.th

Published in Micro & Nano Letters; Received on 20th February 2018; Revised on 31st March 2018; Accepted on 9th April 2018

The piezoelectric poly(vinylidene fluoride-hexafluoropropylene) (P(VDF-HFP)) has been incorporated with zinc oxide (ZnO) of different forms, i.e. nanoparticles (NPs), nanorods (NRs), and microrods (MRs). The polymer has been activated the piezoelectric phase with the poling field of 70 MV/m at 90°C for 10 min. ZnO of various particle types is grown into piezoelectric wurtzite. The addition of ZnO has slightly changed the degree of crystallinity of the polymers and clearly increased the elasticity to the best value in the case of inserted MRs. The electroactive phase of the polymer-based film has been enhanced at 2 wt% of ZnO for both NPs and NRs cases. The dielectric constant of the films increased with ZnO concentration. Finally, a cantilever beam structure with the patch of P(VDF-HFP) reinforced with ZnO of 2 wt% NRs shows the best performance as a microsource of the energy of about 1  $\mu$ W. Development of micropower energy harvesting in P(VDF-HFP) with ZnO NRs has been substantially and highly promising to power small-scale electronics.

**1. Introduction:** A ceramic mixed in a host polymer has been manufactured to achieve good flexibility and high electroactivity for years [1–3]. The coupling between mechanical and electrical properties, i.e. piezoelectric effect existed in the active phases of ceramic and a polymer matrix has been gained much attention for various applications such as transducers, actuators and so on [4–6]. Recent progress in low-power, wireless microelectronic devices have raised an increased interest in harvesting energy using piezoelectric polymers due to view points of material engineering and economic conditions [7]. Amongst piezoelectric polymers, poly(vinylidene fluoride) (P(VDF)) has been widely studied, including its two copolymers, i.e. P(VDF)-hexafluoropropylene (P(VDF-HFP)) and PVDF-trifluoroethylene. So far, there have been only a few reports on piezoelectric P(VDF-HFP) which is relatively good mechanically response to an electrical stimulus and much cheaper than P(VDF) [8]. Various fillers such as graphene, carbon black, and lead zirconate titanate including zinc oxide (ZnO) have been used to reinforce a polymer. This work focuses on ZnO which is often available in a field of anti-bacterial agent [9, 10] but not as a piezoelectric filler. There have also previous reports on ZnO nanowire in energy harvesting applications [11–13] but a few types of research are reported about its implementation on the electro-mechanical properties of a P(VDF-HFP) composite [14]. In this work, piezoelectric ZnO of different particle types which are nanoparticles (NPs), nanorods (NRs), and microrods (MRs) have been comparatively investigated their effect on the piezoelectric P(VDF-HFP). This is to extend the materials into an application as a microsource of energy which is an important issue for our future outlook. Since both materials are piezoelectric, and polymers generally suffer from relatively low piezoelectric coefficients. Developing a guideline to this problem is of useful for scientific and engineering viewpoint.

### 2. Materials and methods

**2.1. Preparation of ZnO nanostructures:** ZnO NPs and NRs were synthesised according to Harnack *et al.* [15]. The powder of zinc acetate dihydrate ( $\text{Zn}(\text{CH}_3\text{COO})_2 \cdot 2\text{H}_2\text{O}$ ,  $\geq 98\%$ , Sigma-Aldrich) of 29.5 g was dissolved in 125 ml methyl alcohol (J.T. Beaker) and 14.8 g of potassium hydroxide (KOH, 85%, Merck) was separately dissolved in 65 ml methyl alcohol ( $\text{CH}_3\text{OH}$ , 99%,

J.T. Baker). The solutions were mixed at 60°C. NPs were obtained after 3 h while it took three days to obtain NRs. The solutions were rinsed several times with methyl alcohol. MRs were prepared by adapting the method of Greene *et al.* [16]. A seeding solution was prepared by mixing of 0.01 M  $\text{Zn}(\text{CH}_3\text{COO})_2 \cdot 2\text{H}_2\text{O}$  and 0.03 M sodium hydroxide (NaOH, 98%, Sigma-Aldrich) in methyl alcohol. The mixture was stirred at 60°C for 2 h. The seeding solution of 1 ml was then injected into the mixture of 25 mM zinc nitrate hydrate ( $\text{Zn}(\text{NO}_3)_2 \cdot x\text{H}_2\text{O}$ , 99.999%, Sigma-Aldrich) and 25 mM hexamethylene tetramine (HMTA, 99%, Sigma-Aldrich) in deionised water at 90°C. The solution was stirred for 3 h. Afterwards, the solution was cooled down to room temperature, the precipitated ZnO was filtered and calcined at 600°C to obtain ZnO MRs.

**2.2. Preparation of P(VDF-HFP) thin films:** P(VDF-HFP) powder (Solef 11010/1001, 90:10 wt%, Solvay Solexis) dissolved in N,N-dimethylformamide (DMF, 99%, Sigma-Aldrich) with a weight fraction of 250 mg/ml was prepared. The solution was stirred at 40°C for 2 h. After that, the solution was kept at room temperature (18°C) until all air bubbles disappeared. The solution was casted on a glass substrate by using an adjustable film applicator (H.J. Unkel Limited) and dried at 90°C for 2 h. To exhibit the piezoelectricity, the films were undergone the constant electric fields of about 70 MV/m at 90°C for 10 min [8]. To assemble the piezoelectric films an indium tin oxide coated polyethylene terephthalate (ITO-PET, 60  $\Omega$ /square, Sigma-Aldrich) was used as a top electrode and a copper tape with carbon ink was underneath. The samples were then enamelled by a thermoplastic film at 130°C.

**2.3. Characterisation of ZnO formation and AFM measurement:** All the synthesised ZnO were imaged by using either transmission electron microscope (TEM, JEM-2010, JEOL Ltd.) or scanning electron microscope (SEM, FEI Quanta 400). The distribution of NPs in P(VDF-HFP) matrix was visualised by using a backscattering mode of the SEM. X-ray diffraction pattern and crystallinity of the polymer films were evaluated by using X-ray diffractometer (X'Pert MPD, Philips, the Netherlands).

Functional groups of the polymer were studied via a Fourier transform infrared spectrometer (FT-IR, LUMOS 70, Bruker).

P(VDF-HFP) has molecular formula as  $(-\text{CH}_2\text{CF}_2-)_x[-\text{CF}_2\text{CF}(\text{CF}_3)-]_y$ . The electroactive fraction is able to evaluate from an absorption at  $840\text{ cm}^{-1}$  which is assigned to a mixed mode of  $\text{CH}_2$  rocking and  $\text{CF}_2$  asymmetric stretching vibration of electroactive  $\beta$ -phase, and in-plane bending of as-received  $\alpha$ -phase at  $776\text{ cm}^{-1}$  [17]. By using (1), the fraction can be calculated from the following equation:

$$F_{EA} = \frac{A_\beta}{\left(\frac{K_\beta}{K_\alpha}\right)A_\alpha + A_\beta} \quad (1)$$

where  $K_\alpha$  and  $K_\beta$  are the absorption coefficients at the respective wavenumber whose the values are  $6.1 \times 10^4$  and  $7.7 \times 10^4\text{ cm}^2\text{ mol}^{-1}$  [18], respectively.

Elastic modulus was evaluated by using nanoindentation technique through an Atomic Force Microscope (AFM, Nanosurf Easyscan2, Nanosurf) and fitting the obtained force–distance curve to Hertz's theory [19]. A contact between the cantilever tip and a sample was mannered as a half sphere placed on a flat surface. A relationship between contact area and elastic modulus is given by

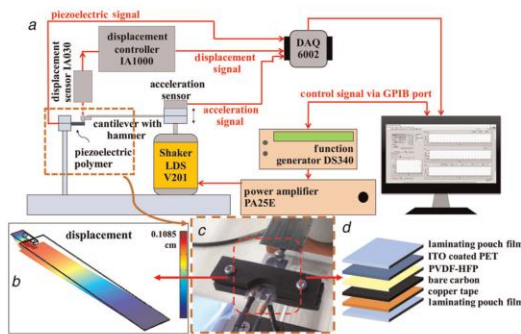
$$a_{\text{Hertz}} = \left(\frac{RF}{K}\right)^{1/3} \quad (2)$$

where  $R$  is the tip radius,  $F$  is the applied force through the cantilever tip,  $a_{\text{Hertz}}$  is the contact radius related to  $Z$  scanner and deflection of the cantilever by  $a_{\text{Hertz}} = \sqrt{R(Z - \delta)}$  and  $K$  is the reduced elastic modulus given by

$$\frac{1}{K} = \frac{3}{4} \left( \frac{1 - \nu^2}{E} + \frac{1 - \nu_i^2}{E_i} \right) \quad (3)$$

where  $E$  and  $\nu$  are elastic modulus and Poisson's ratio, respectively. The sharp tip apex ( $<10\text{ nm}$ ) is for approaching a polymer. Before using to observe the deformation of the cantilever, the laser sensor of the AFM has been calibrated by approaching the cantilever to a glass surface [20]. The system sensitivity is  $7.82 \times 10^{-7}\text{ m/V}$ .

2.4. Characterisation of the electro-mechanical properties: A dielectric constant for all the polymer-based films was measured by using LCR Meter (IM 3533, HIOKI) with dielectric test fixture probe (16451B, Agilent). The ability for energy harvesting of the film was tested by using the setup shown in Fig. 1.



**Fig. 1** Energy harvesting setup  
 a Schematic view of the setup for piezoelectric energy harvesting  
 b Chosen configuration consists of a cantilever beam as a hammer and piezoelectric harvester at the free end of the beam  
 c Photograph of the beam configuration  
 d Physical structure of piezoelectric harvester

An energy harvester of cantilever beam structure is chosen in this work due to its simplicity to implement at a low operating frequency ( $<100\text{ Hz}$ ). The beam was fixed at one end and another was free. The equation of motion for transverse vibration and eigenfrequency to describe the mechanism of a uniform cross-sectional cantilever beam of length  $l$  is derived from the Euler–Bernoulli theorem as given by

$$w(x, t) = \Phi(t)X(x) \quad (4)$$

$$\Phi(t) = D_1 \sin \omega t + D_2 \cos \omega t \quad (5)$$

$$X(x) = C_1 \left( \sin \alpha x + \frac{C_2}{C_1} \cos \alpha x + \frac{C_3}{C_1} \sinh \alpha x + \frac{C_4}{C_1} \cosh \alpha x \right) \quad (6)$$

$$(\alpha l)^2 = \omega^2 \sqrt{\frac{\rho A}{EI}} \quad (7)$$

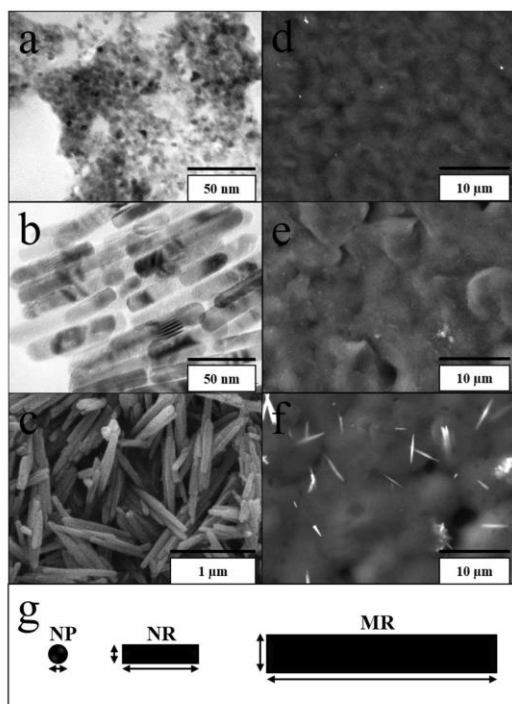
where  $w$  is the deformation of the beam. The constants  $C$  and  $D$  can be obtained by the application of boundary conditions and normalisation. Equation (7) is a corresponding non-dimensional frequency for a solution depending mainly on the dimension of the beam. A location to patch a piezoelectric polymer onto the beam maximising energy conversion was done by using a finite element analysis (FEA) through the COMSol Multiphysics software (COMSOL 4.2 Update 3, USA). P(VDF) and its material property [21] was used as a piezoelectric device in the simulation. In the model, the piezoelectric film was sandwiched by a plastic film of the density of  $1380\text{ kg/m}^3$  and an elastic modulus of  $2\text{ GPa}$ . A configuration that generated a higher mechanical strain of the polymer was chosen.

A cantilever ( $135.0 \times 2.0 \times 0.5\text{ mm}^3$ ) made of spring steel with a hammer at the end was mounted on a permanent magnet shaker (V201, LDS Test, and Measurement) that was controlled via function generator (DS340, Stanford Research System). A vibration of the cantilever was detected by a CMOS laser analogue sensor with a controller (IA030, IA1000, KEYENCE). The cantilever was vibrated at  $32\text{ Hz}$  with  $15\text{ g m/s}^2$  acceleration along the experiment. The generated signals from piezoelectric polymer were recorded by USB data acquisition module (DAQ6002, Nation instrument). All instruments were controlled via LabVIEW software package (LabVIEW 2013, Nation instrument).

### 3. Results and discussion

3.1. ZnO formation in the P(VDF-HFP) matrix: The SEM images of different forms of synthesised ZnO were shown in Fig. 2. The NPs in Fig. 2a have an average diameter of  $6.25 \pm 1.20\text{ }\mu\text{m}$  with an aspect ratio of 1. Some of the NPs have fused along their identical crystal faces and formed the oriented chains into the NRs. Subsequently formed NRs in Fig. 2b are  $11.20 \pm 2.63\text{ nm}$  in diameter and  $62.99 \pm 18.53\text{ }\mu\text{m}$  in length with an aspect ratio of 5.62. The MRs in Fig. 1c, respectively, have average length and diameter of  $606 \pm 166\text{ nm}$  and  $71 \pm 16\text{ nm}$  with an aspect ratio of 8.53. Most MRs dispersed randomly in the matrix. In case of NPs and NRS, the bright spots of the visualised mode are bigger than the particle size caused by the agglomerated particles.

3.2. Properties of the P(VDF-HFP) film with and without ZnO: XRD patterns of ZnO doped P(VDF-HFP) were shown in Fig. 3. The semi-crystalline structure with  $\alpha$ -phase of the bare P(VDF-HFP) was confirmed by the diffraction peaks at  $2\theta = 18.2^\circ, 20.0^\circ, 26.6^\circ,$  and  $38.0^\circ$ , corresponding to the (100), (020), (110), and (021) crystalline planes [14], respectively. With ZnO dopants, their diffraction peaks appeared at  $31.82, 34.54,$  and  $36.42$ , corresponding to the (100), (002), and (101) of wurtzite ZnO [22].



**Fig. 2** Morphology of synthesised ZnO  
*a* TEM image of ZnO NPs  
*b* TEM image of ZnO NRs  
*c* SEM image of MRs. The distribution of NPs in a polymer matrix was shown by means of backscattering mode of SEM;  
*d* NPs,  
*e* NRs,  
*f* MRs  
*g* Sketch depicted for each nanostructure

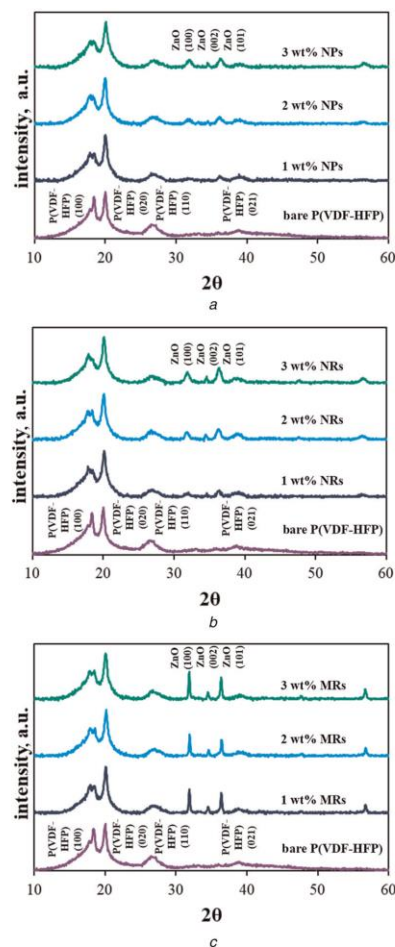
The percentage of crystallinity of semi-crystalline P(VDF-HFP) was given by (8) and the calculations for all cases were collected in Table 1

$$\% \text{crystallinity} = \frac{A(\text{peak})}{A(\text{total})} \times 100 \quad (8)$$

where  $A$  is an intensity at  $2\theta$ .

Fig. 4 shows the absorption spectra in the range of infrared, that corresponding to the mode of vibration of chemical bonding, via FT-IR. The absorption bands at 489, 614, 766, 795, 855, and 976  $\text{cm}^{-1}$  indicated the  $\alpha$ -phase of PVDF, while 840  $\text{cm}^{-1}$  acted as a characteristic of the  $\beta$ -phase [18]. The addition of ZnO in P(VDF-HFP) decreased the absorption peak of the  $\beta$ -phase in MRs. The relative fraction of  $\beta$ -phase or the electroactivity has its maximum value at 2 wt% for both NPs and NRs inserted.

The material elasticity of the polymer-based composites is much better when compared with the bare polymer. The elastic modulus value is the best at 2 wt% for each particle type. However, the concentration  $>2$  wt% may cause the agglomeration of the particles. This can be inherent internal defects that most pronounced in the case of NPs and resulted in a decrease in the elastic modulus. The highest elasticity occurred in the MRs type. This implies that the sample consisted of well-bonded particles so that the applied stress between particles and matrix effectively transferred.



**Fig. 3** XRD patterns of the P(VDF-HFP) films with different concentrations and forms ZnO

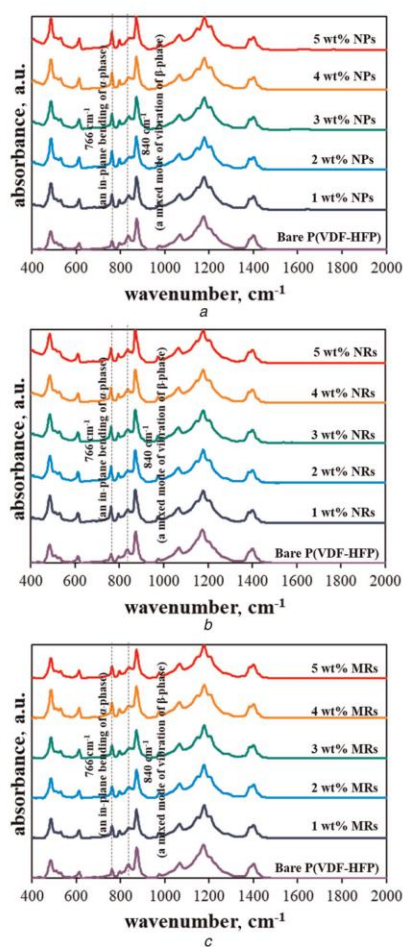
*a* NPs  
*b* NRs  
*c* MRs

Table 1 summarises the material properties for different amounts of NPs, NRs, and MRs ZnO. The polymer-based films with NRs and MRs have slightly higher crystalline phase and larger elastic modulus compared with NPs. The best value for the active phase derived from the addition of ZnO was found in 2 wt% NRs of ZnO.

**3.3. Electro-mechanical properties:** Plots of the dielectric constant of the samples measured at room temperature in a range of frequency between 1 and 20,000 Hz were shown in Fig. 5. The values increased with respect to the ZnO fractions and decrease with increments of the frequency. The phenomenon derived by nanoscale dimension has been described by Yamada *et al.* [23]. Spherical-like structure with high surface area possesses higher dielectric constant. This has been proved by the zeta potential (ZetaPALS, Brookhaven). A resulted potential of  $25.78 \pm 1.83$  mV at the zeta layer of NPs indicated the existence of a lot of fixed charges at the prepared films. This implies that the NRs and NPs increase the capacitance of the polymer, leading to the enhancement of the dielectric constant of the films.

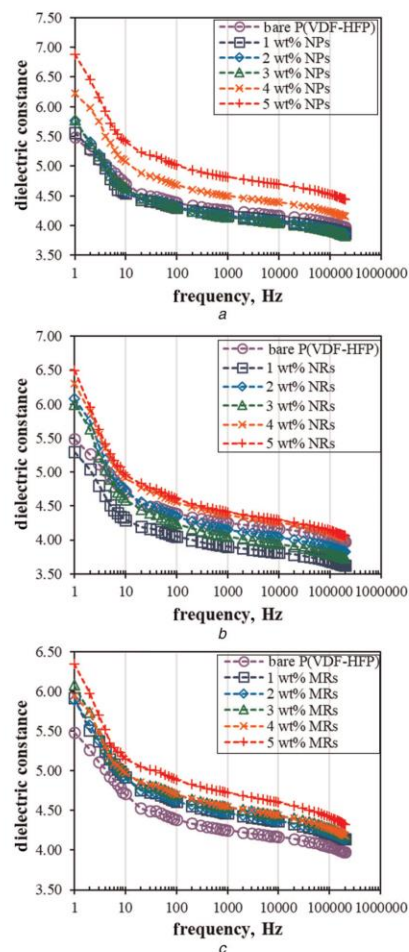
**Table 1** Material properties of P(VDF-HFP) with various concentrations of ZnO of different shapes

P(VDF-HFP)		Crystallinity, %	Electro-activity	Elasticity, GPa
ZnO	Concentration, wt%			
—	0	46.21	0.34	1.89 ± 0.30
NPs	1	46.21	0.47	2.66 ± 0.60
	2	46.38	0.54	2.68 ± 0.67
	3	46.02	0.49	1.80 ± 0.25
NRs	1	46.09	0.49	3.24 ± 0.36
	2	46.26	0.51	3.36 ± 0.39
	3	46.23	0.49	2.57 ± 0.33
MRs	1	47.58	0.48	3.16 ± 0.32
	2	47.98	0.43	4.43 ± 0.70
	3	48.04	0.39	3.42 ± 0.41

**Fig. 4** FT-IR spectrum of the P(VDF-HFP) films with different concentrations and forms ZnO

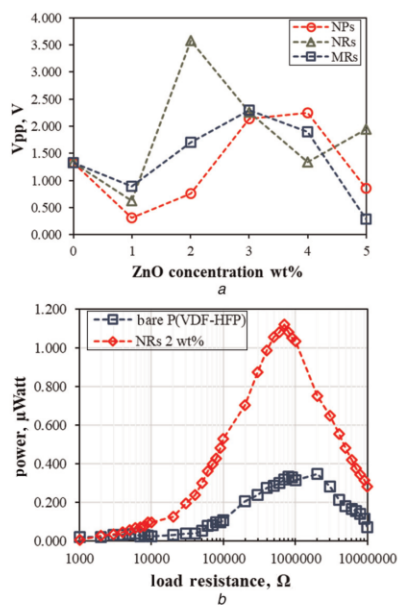
a NPs  
b NRs  
c MRs

The open-circuit voltage output of each sample was summarised in Fig. 6a. The optimum condition was 2, 3, and 4 wt% for NRs, MRs, and NPs, respectively. From the results, the 2 wt% NRs

**Fig. 5** Plots of dielectric constant as functions of frequency for P(VDF-HFP)NPs with ZnO

a NPs  
b NRs  
c MRs

inserted sample is a choice for power harvesting test. From Fig. 6b, the AC power of the bare P(VDF-HFP) was only 0.35  $\mu$ W while 2 wt% NRs in P(VDF-HFP) reached 1.12  $\mu$ W.



**Fig. 6** Curves of  
 a Open-circuit voltage output with different concentrations and forms of ZnO  
 b Obtained power with respect to the load resistance compared between bare P(VDF-HFP) and P(VDF-HFP) with 2 wt% NRs ZnO

The optimum resistance was reduced accordingly from 2 MΩ to 700 kΩ. For a piezoelectric material under cyclically applied force, the figure-of-merit or the product of piezoelectric ( $d_{31} \times g_{31}$ ) coefficients is perpendicular to generating power [8]. This means that the P(VDF-HFP) matrix inserted with 2 wt% NRs ZnO has developed the energy harvesting performance for a given configuration. As the cantilever was vibrated at 32 Hz, the polymer composite is able to harvest on low vibration level.

**4. Conclusion:** The P(VDF-HFP) has been incorporated with ZnO of different forms, i.e. NPs, NRs, and MRs. The polymer has been activated the piezoelectric phase with the poling filed of 70 MV/m at 90°C for 10 min. ZnO of various particle types is grown into piezoelectric wurtzite. The addition of ZnO has slightly changed the degree of crystallinity of the polymers and clearly increased the elasticity to the best value in the case of inserted MRs. The electroactive phase of the polymer-based film has been enhanced at 2 wt% of ZnO for both NPs and NRs cases. The dielectric constant of the films increased with ZnO concentration. Finally, a cantilever beam structure with the patch of P(VDF-HFP) reinforced with ZnO of 2 wt% NRs shows the best performance as a microsource of the energy of about 1 µW. Development of micropower energy harvesting in P(VDF-HFP) with ZnO NRs has been substantially and highly promising to power small-scale electronics.

**5. Acknowledgments:** The authors acknowledge the financial supports from the Royal Golden Jubilee Ph.D. Program under

grant no. PHD/0034/2553, the Department of Physics, and the Graduate School, Prince of Songkla University, Hat Yai, Songkhla, Thailand. The authors thank Prof. Dr. Andrei Kholkin for sharing their knowledge on the AFM technique. Thanks to Ms. Sirirat Ouiganon for helping hands.

## 6 References

- [1] Kawai H.: 'The piezoelectricity of poly(vinylidene fluoride)', *Japan J. Appl. Phys.*, 1969, **8**, pp. 975
- [2] Ikeda T.: 'Fundamental of piezoelectricity' (Oxford Science Publications, New York, 1990)
- [3] Das-Gupta D.K.: 'Ferroelectric polymers and ceramic-polymer composites' (Tran Tech Publ, Zurich, 1994)
- [4] Whatmore R.W.: 'Pyroelectric ceramics and devices for thermal infra-red detection and imaging', *Ferroelectrics*, 1991, **118**, pp. 241–259
- [5] Uchino K.: 'Ferroelectric devices' (Marcel Dekker, New York, 2000)
- [6] Phempomsakul Y., Muensit S., Guy I.L.: 'Determination of piezoelectric and pyroelectric coefficients and thermal diffusivity of 1–3 PZT/epoxy composites', *IEEE Trans. Dielect. Electr. Insul.*, 2004, **11**, (2), pp. 280–285
- [7] Beeby S.P., Torah R.N., Tudor M.J.: 'A micro electromagnetic generator for vibration energy harvesting', *J. Micromech. Microeng.*, 2007, **17**, p. 1257
- [8] Sukwisute P., Muensit N., Soontaranon S., *ET AL.*: 'Micropower energy harvesting using poly(vinylidene fluoride hexafluoropropylene)', *Appl. Phys. Lett.*, 2013, **103**, p. 063905
- [9] Zhang L., Ding Y., Povey M., *ET AL.*: 'Zno nanofluids – a potential antibacterial agent', *Prog. Nat. Sci.*, 2008, **18**, (8), pp. 939–944
- [10] Shalumon K.T., Anulekha K.H., Nair Sreeja V., *ET AL.*: 'Sodium alginate/poly(vinyl alcohol)/nano ZnO composite nanofibers for antibacterial wound dressings', *Int. J. Biol. Macromol.*, 2011, **49**, pp. 247–254
- [11] Xu S., Qin Y., Xu C., *ET AL.*: 'Self-powered nanowire devices', *Nat. Nanotechnol.*, 2010, **5**, pp. 366–373
- [12] Zhu G., Yang R., Wang S., *ET AL.*: 'Flexible high-output nanogenerator based on lateral ZnO nanowire array', *Nano Lett.*, 2010, **10**, pp. 3151–3155
- [13] Hu Y., Lin L., Zhang Y., *ET AL.*: 'Replacing a battery by a nanogenerator with 20 V output', *Adv. Mater.*, 2012, **24**, pp. 110–114
- [14] Parangusan H., Ponnamma D., Ali S.M., *ET AL.*: 'Stretchable electrospun PVDF-HFP/Co-ZnO nanofibers as piezoelectric nanogenerators', *Sci. Rep.*, 2018, **8**, p. 754
- [15] Harnack O., Pacholski C., Weller H., *ET AL.*: 'Rectifying behavior of electrically aligned ZnO nanorods', *Nano Lett.*, 2013, **3**, pp. 1097–1101
- [16] Greene L.E., Law M., Goldberger J., *ET AL.*: 'Low-temperature wafer-scale production of ZnO nanowire arrays', *Angew. Chem. Int. Ed.*, 2003, **42**, pp. 3031–3034
- [17] Gregorio R., Cestari M.: 'Effect of crystallization temperature on the crystalline phase content and morphology of poly(vinylidene fluoride)', *J. Polym. Sci. B. Polym. Phys.*, 1994, **32**, pp. 859–870
- [18] Martinsa P., Lopesa A.C., Lanceros-Mendoza S.: 'Electroactive phases of poly(vinylidene fluoride) determination, processing and applications', *Prog. Polym. Sci.*, 2014, **39**, pp. 683–706
- [19] Hertz H.: 'On the contact of elastic solids', *J. Reine. Angew. Math.*, 1881, **92**, pp. 156–171
- [20] Cappella B., Silbernagl D.: 'Nanomechanical properties of mechanical double-layer: a novel semiempirical analysis', *Langmuir*, 2007, **23**, pp. 10779–10787
- [21] Jain A., Prashanth K.J., Sharma A., *ET AL.*: 'Dielectric and piezoelectric properties of PVDF/PZT composites: a review', *Polym. Eng. Sci.*, 2015, **55**, (7), pp. 1589–1616
- [22] Özgür Ü., Alivov Y.I., Liu C., *ET AL.*: 'A comprehensive review of ZnO materials and devices', *J. Appl. Phys.*, 2005, **98**, p. 041301
- [23] Yamada T., Ueda T., Kitayama T.: 'Piezoelectricity of a high-content lead zirconate titanate/polymer composite', *J. Appl. Phys.*, 1982, **53**, (6), p. 4328

**Publication III**

**Low-dimensional Piezoelectric Materials for Nanoenergy Scavenging**

**Phooplub K., S. Suwanboon, P. Amornpitoksuk, Muensit N.**

Proceeding





## Low-dimensional Piezoelectric Materials for Nanoenergy Scavenging

K. Phooplub<sup>a</sup>, S. Suwanboon<sup>b</sup>, P. Amornpitoksuk<sup>c</sup>, N. Muensit<sup>a,d,\*</sup>

<sup>a</sup> Department of Physics, Prince of Songkla University, Songkhla, 90112, Thailand

<sup>b</sup> Department of Materials Science and Technology, Prince of Songkla University (PSU), Songkhla, 90112, Thailand

<sup>c</sup> Department of Chemistry, Prince of Songkla University (PSU), Songkhla, 90112, Thailand

<sup>d</sup> NANOTEC Center of Excellence at Prince of Songkla University (PSU), Songkhla, 90112, Thailand

\*nantakan.m@psu.ac.th

### Abstract :

Energy scavenging, which is a process of capturing ambient mechanical energy and converting it into useable electricity, with low-dimensional materials has been demonstrated in this work. Hence, ZnO material is of interest due to it has high potential in several applications including piezoelectric. The ZnO used in the analysis in this work has been produced by the chemical reactions through the low temperature process, which is easily controlled its crystallographic structure. Its related piezoelectric coefficients are the  $d_{33}$ ,  $d_{31}$  coefficients. From the finite element analysis for nanorod and nanobelt of ZnO material, it is possible to capture a vibration surrounding them and deliver a corresponding output voltage in a range of 200-400 mV. For a suitable load impedance, the harvested power is able to feed some ultra-low power electronics such as biomedical sensors. Small-scale power harvesting systems with suitable energy scavenging designs that incorporating a low-dimensional structure are, therefore, promising as well as challenging.

**Keywords:** Energy scavenging ;Energy harvesting; Piezoelectric; One-dimensional; Quasi-one-dimensional, Zinc oxide

### Introduction

Novel technologies relating to scavenging energy from ambient vibrations such as noise and vibration have been developed for about a decade [1,2]. In these technologies, traditional ferroelectric materials have been used because their coupling between mechanical and electrical properties can be done through the piezoelectric activity. In a similar period of time, low-dimensional structures of various materials have been discovered and systematically studied for various compositions and shapes [3]. The low-dimensional materials have been reported to have high potential application in optics, optoelectronics, catalysis, field effect transistor, ultrasensitive and piezoelectric. However, their applications in energy scavenging yet have not been extensively explored. This work thus aims to demonstrate the behaviour of a low-dimensional material which is piezoelectric and the possibility of using the material to convert the mechanical deformation into the electrical energy that can be delivered to some ultra-low power electronic devices. Functional oxide-based nanostructures such as nanorod and nanobelt of zinc oxide (ZnO) have been chosen for a demonstration. This is because ZnO has unique properties which are semiconductor, piezoelectric and compatible with biological environment. Nanostructures of zinc oxide can be synthesised by several methods such as vapour liquid-solid method [4], metal-organic chemical vapour deposition [5] and chemical method [6-9]. The ZnO used in the analysis in

this work has been produced by the chemical reactions through the low temperature process, which is easily controlled its crystallographic structure, shapes and related properties [8].

### Modeling and Constitutive Equations

The crystallographic structure of interest of ZnO in this work is wurtzite, whose most familiar piezoelectric elements are the  $d_{33}$  and  $d_{31}$  coefficients [10]. Hence, the direct piezoelectric effect, where the electrical polarization is produced by the applied mechanical stress [11], is for the case.

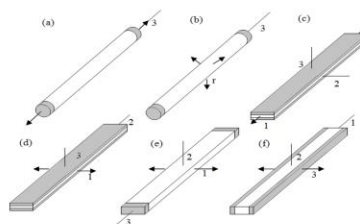


Fig. 1. Modes of vibrations (a) length-extensional and (b) radial-dilatational for a rod, and (c) length-extensional, (d) width-extensional-1, (e) width-extensional-2 and (f) width-extensional-3 for a nanobelt. (Redrawn from [11] with permission of the publisher.)

In order to understand the behaviour of the ZnO nanostructures under the application of a mechanical



stress, possible modes of vibrations of a structure are considered. From the illustrations in Fig.1, the coupling between mechanical and electrical properties can be expressed for one-dimensional and quasi-one-dimensional structures by Eqs.(1) and (2), respectively as [11]:

$$k_p^2 = \frac{2}{1 + \sigma'} \frac{d_{31}^2}{c_{33}^E \epsilon_{33}^E} \quad (1)$$

$$k_{31}^2 = \frac{e_{31}^2}{\tilde{c}^E \epsilon^{*WT}} \quad (2)$$

In the equations,  $k^2$ ,  $d$ ,  $e$ ,  $c$  and  $\epsilon$  are the electromechanical coupling coefficient, piezoelectric charge coefficient, piezoelectric stress coefficient, elastic stiffness and permittivity, respectively.  $\sigma$  in Eq.(1) is defined by  $c_{12}^E / c_{11}^E$ . For the direct piezoelectric effect, The first number in the subscript denotes the direction of an applied mechanical stress while the second the electrical displacement which is directly related to the output electric field.

The finite element analysis (FEA) was performed using the software program, COMSOL Multiphysics [12]. In the FEA, the nanorod of (approx.) 100 nm in its diameter and 3 $\mu$ m in length [9] was clamped on its end and a stationary force of 100 nN was applied on the free-end (see Fig.1 (b)). For the nanobelt, a similar size to the nanorod was taken and the width of 50 nm was used in the calculation (see Fig.1 (e)).

### Numerical Results and Discussion

For the applied force of 100 nN captured by the nanorod and nanobelt of the dimensions mentioned above, potential distribution are as shown in Fig.2. and Fig.3, respectively.

From the analyses performed on the ZnO nanorod and ZnO nanobelt, absolute values of the output voltage are 0.2274 V and 0.3768 V, respectively. It is length-extensional mode of vibration for the nanorod and width-extensional-2 for the nanobelt that are most desirable for the energy scavenging process.

By using the FEA used in this work, we are able to study for other types of low-dimensional materials such as ZnS nanobelt. It was found that the output electric potential is 0.0717 V. These results indicated that the efficiency of energy scavenging depends on the shape of nanostructures, material parameters, electrodes and modes of vibration and power sources surrounding the energy harvester.

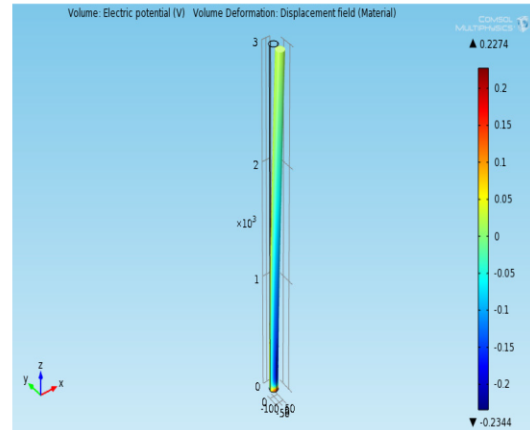


Fig. 2. The FEA analysis displays a potential distribution along the clamped nanorod of 100 nm in its diameter and 3 $\mu$ m in length at an applied force of 100 nN.

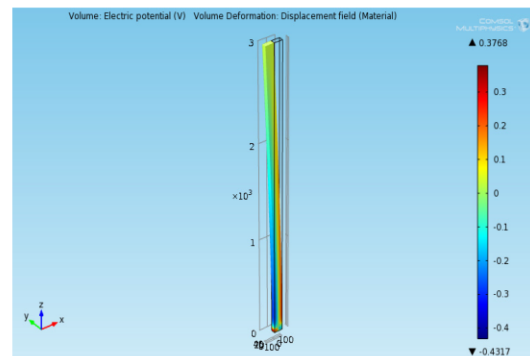


Fig. 3. The FEA analysis displays a potential distribution along the y-direction of the nanobelt of 100 nm in its diameter, 3 $\mu$ m in length and the width of 50 nm at an applied force of 100 nN.

For commercial electronic devices of ultra-low power consumption such as implantable medical devices (IDMs), a power to miniaturize the device is in the range of 30  $\mu$ W to 10 mW at the load impedances of 0.5 to 100 k $\Omega$  [13]. With these load impedances, the nanorod used in our analyzation is capable of delivering the power of about 0.52  $\mu$ W whereas it is 1.42  $\mu$ W for the nanobelt. However, these are a simple case used in the calculations. In reality, a single nanostructure is not possible to deliver enough useful electrical energy. Further designs of energy scavenging system incorporating the nanostructures are being studied.

### Conclusions

Energy scavenging with low-dimensional materials is possible as demonstrated in this work. Potential distribution along the nanorod and nanobelt of ZnO



Proceedings of the 4<sup>th</sup> International Conference on Nanostructures (ICNS4)  
12-14 March, 2012, Kish Island, I.R. Iran

material showed that we could obtain the output voltage approximately of 200-400 mV. However, in order to use them for smart miniaturized systems, a suitable design of a piezoelectric vibration structure with appropriate electrode patterns is necessary.

[12] PSU-Grid, 2011.

[13] Y. Yang, X. J. Wei, J. Liu, Suitability of a thermoelectric power generator for implantable medical electronic devices, *J. Phys. D: Appl. Phys.*, Vol.40 (2007), 5790-5800.

### Acknowledgment

The authors thank the Thailand Research Fund through the Royal Golden Jubilee Ph.D.Program (Grant No.PHD/0034/2553) and the National Nanotechnology Center (NANOTEC), NSTDA, Ministry of Science and Technology through its network at the PSU.

### References

- [1] S. Priya, D. J. Inman, *Energy Harvesting Technologies*, 2009, Springer Science+Business Media, USA
- [2] N. Muensit, ed. *Energy harvesting with piezoelectric and pyroelectric materials*, 2011, Trans Tech Publications Ltd, Switzerland.
- [3] Z. L. Wang, *Piezoelectric nanostructures: From growth phenomena to electric nanogenerators*, *MRS Bulletin*, 32 (2007),109-116
- [4] R. S. Wagner, W. C. Ellis, Vapor-liquid-solid mechanism of single crystal growth, *Appl. Phys. Lett.* 4(1964) ,89
- [5] Z. Zhu, Self-organized growth of II-VI wide bandgap quantum dot structures, *Phys. Status Solidi*, b 202(1997), 827
- [6] Z. Li, Y. Xiong, Y. Xie, Selected-control synthesis of ZnO nanowires and nanorods via a PEG-Assisted Route, *Inorg. Chem.*, 42(2003), 8105-8109
- [7] O. Harnack, C. Pacholski, H. Weller, A. Yasuda, J. M. Wessels, Rectifying behavior of electrically aligned ZnO nanorods, *Nano Lett.*, Vol. 3 No. 8 (2003),1097-1101
- [8] S. Suwanboon, P. Amornpitoksuk, S. Muensit, Enhancement of optical bandgap and luminescent characteristics of one-dimensional ZnO nano particles, *Journal of ceramic processing research*, Vol. 11 No.4(2010),pp. 419-424
- [9] S. Suwanboon, P. Amornpitoksuk, P. Bangrak, A. Sukolrat, N. Muensit, The dependence of optical properties on the morphology and defects of nanocrystalline ZnO powders and their antibacterial activity, *Journal of ceramic processing research*, Vol. 11 No.5(2010),pp. 547-551
- [10] H. Morkoç, Ü. Özgür, *Zinc Oxide*, 2009, Wiley-VCH, 1-2,59-60,Germany
- [11] T. Ikeda, *Fundamentals of Piezoelectricity*, 1990, Oxford Science, 107-113, USA.

**Publication IV**

**Small-Scale Energy Harvesting With Low-Dimensional Piezoelectric**

Muensit N., **Phooplub K**

Proceeding

## Small-Scale Energy Harvesting With Low-Dimensional Piezoelectrics

Supasarote Nantakan Muensit and Kittirat Phooplub

Physics Department, Science Faculty and Center of Excellence in Nanotechnology for Energy (CENE), Prince of Songkla University  
 (PSU), Songkhla, Thailand

Email (contact person) : nantakan.m@psu.ac.th

### ABSTRACT

This work has used a simple wet chemical method for obtaining free-standing zinc oxide or ZnO nanostructures. The starting agents and the chemistry of the interaction were chosen to produce wurtzite ZnO which is good piezoelectric. Ultra-low force is necessary to use to produce mechanical deformation of the nanorods. The output voltage is theoretically analysed that it could be generated by a static force of the order of 20-100nN applied normal to the cross-sectional surface of the ZnO nanorod. Increasing the number of nanorods of different lengths and small diameters implies that a set of these ZnO piezoelectrics are possible to use as a nanogenerator. In addition, owing to its biodegradability it is suitable for integration with implantable medical devices having none of input electric field.

### INTRODUCTION

Desire in self-powered electronic devices is one of the reasons in increasing worldwide researches in energy harvesting (Muensit, 2011). Energy harvesting or scavenging is a conversion of ambient energy into electrical energy in order to power small electronic devices, making them self-sufficient and less dependent on fossil fuels. General idea underlying energy harvesting research is the extraction of electrical energy from the operating environment (Hurlebaus and Gaul, 2006). There are several power generating methods using ambient environment energy, including thermal gradient, solar energy and vibration energy. Among these methods, vibration energy harvesting has attracted much attention because it provides high power density compared to others. In addition, sources of vibration can be sought everywhere (Roundy *et al.*, 2005).

Several techniques can be used in vibration energy conversion processes, e.g., electrostatic, electromagnetic, piezoelectric. Hence, piezoelectric approach is a priority because it yields a stable energy density and is independent from external power supply. It couples between a mechanical deformation and an electric field. If the first is applied, the latter is developed and vice versa.

Piezoelectricity exists in a material lacking of crystal symmetry. This characteristic results in having a number of dipole moments and a non-zero polarization in the material which is attractive in energy harvesting/scavenging applications. So far, most piezoelectric materials which have been fabricated and reported are, for example, lead zirconate titanate (PZT) ceramics, ferroelectric polymer sheets. The electromechanical properties of these materials are higher when they have been prepared with low-dimensional forms such as 2D thin film, 1D nanorod, nanowire or quasi-1D nanobelt, including nanodot (Zhao *et al.*, 2004). For the PZT, there have been several efforts to fabricate it into a higher-surface-area form by producing PZT fibers and nanorods in order to develop higher electromechanical properties (Sodano, 2003; Chen *et al.*, 2010). Nanostructures of several II-V compounds such as zinc oxide (ZnO) or III-V semiconductors like gallium nitride (GaN) have also gained attraction. There have been reports on ZnO nanorods as one of the most interesting candidates in energy scavenging process (Wang *et al.*, 2006; Lin *et al.*, 2011). Zhao *et al.* (2004) has reported on the ZnO nanobelt having a piezoelectric coefficient of 14.3-26.7 pC/N while the ZnO bulk has 9.93 pC/N.

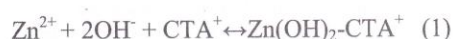
Several techniques have been developed in the synthesis and formation of these one-dimensional materials. These techniques are, i.e., spontaneous growth, template-based synthesis, electrospinning, a top-down lithography etc. One of the spontaneous growth technique, i.e., vapor-liquid-solid (VLS) method is first discussed by Wagner and Ellis during the 1960s. Controllability of aspect ratio of ZnO nanorods and vertical alignment of the nanorods are the advantages of the method. In kinetic energy scavenging, controllable aspect ratio and alignment of the nanorods are the main requirements.

Owing to the biocompatibility and biodegradation of ZnO, this work prepares the nanostructure of piezoelectric ZnO by wet chemical process. This method is relatively simple and rapid. This work then aims to identify theoretically an external forces/stresses to develop a potential voltage within the prepared ZnO. This ZnO piezoelectrics will lead to the piezoelectric nanogenerator and possible integration with implantable medical unit.

## MATERIALS AND METHODS

### Materials

The wet chemical approach (Suwanboon, 2010) is used for obtaining free-standing ZnO nanorods as described below. All chemical agents were reagent grade. Dissolved NaOH 6.4 g in distilled water 1 mL and stir in room temperature 10 minutes until a 1 h. Added 0.02 mole of  $Zn(CH_3COOH)_2 \cdot 2H_2O$  in the solution and stir at 70°C for 3h. At this step the precipitates were formed. The rod-like ZnO particles with half of a micrometer in diameter were normally obtained. In order to decrease the diameter of the rods to be 100 nm or less, the stabilizing agent such as cetyltrimethylammonium bromide (CTAB) of 0.02 mol was added in the solution before adding  $Zn(CH_3COOH)_2 \cdot 2H_2O$ . Afterwards, filtered and rinsed with methanol and distilled water several times. Finally, calcined at 600°C in air about 1 h. The chemical reaction of ZnO, CTAB and NaOH were shown in equations (1)-(3).



### Characterization

The structural and phase formation were identified by an X-ray diffractometer (XRD, X'Pert MPD, Philips). The morphological study was evaluated by a scanning electron microscope (SEM, JSM-5800LV, JEOL).

### Equations

The principles of piezoelectric generator involve an interaction between the mechanical and electrical properties. Equations (4) and (5) are the expressions for the direct and converse piezoelectric effects, respectively.

$$D = eS + \epsilon^S E \quad (4)$$

$$T = c^E S - eE \quad (5)$$

Where  $D$ ,  $S$ ,  $E$ ,  $T$ ,  $e$ ,  $\epsilon^S$  and  $c^E$  are electric flux density, mechanical strain, electric field, mechanical stress, piezoelectric constant, dielectric constant at constant mechanical strain and elastic compliance at constant electric field, respectively. In this work, the converse effect plays important role.

A relation between induced displacement and electrical voltage of the material was investigated by using a finite element analysis (FEA). In the analysis, the voltage is generated by a static force of the order of 20-100 nN acting upon the cross-sectional surface of the nanorod.

## RESULTS AND DISCUSSION

From Figure 1, the XRD diffraction pattern of the ZnO has hexagonal of wurtzite unit cell. When compares with other two phases, i.e. rocksalt and zinc blende, wurtzite is most focused due to it has all the effective piezoelectric coefficients, i.e.  $e_{31}$ ,  $e_{33}$  (Özgüret *et al.*, 2005).

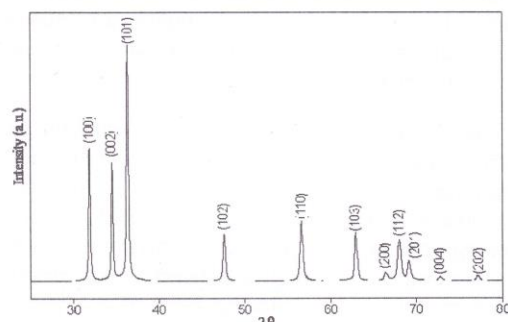


Figure 1. XRD patterns of calcined ZnO.

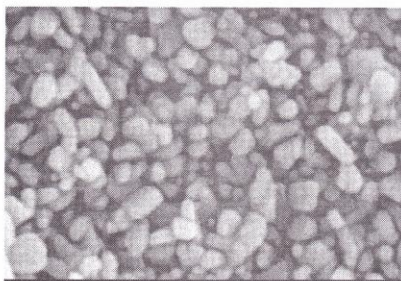


Figure 2. A SEM image of calcined ZnO.

Figure 2 shows a mixture of ZnO of different shapes. The formation of columnar or rod-like structure of ZnO could be more with a careful preparation. Average crystallite size of the columnar is 340 nm in length and 100 nm in diameter for 0.02 mole CTAB. It was found that if the higher concentration of the CTAB was used the thinner the columnar was and the nanorods of different lengths were obtained.

#### Simulation results

The nanorods of different lengths were used in the simulations. Due to ultra-low dimension of the nanorod, the ultra-low force is necessary. Figure 3 shows an example of the ZnO rod with 350 nm in length and 100 nm in diameter which generates an average output voltage of 0.05 V under a normal force of 20 nN. Figure 4 presents the overall FEA results from the rods of different lengths. A deformation (compression) of the rod in terms of its mechanical displacement is displayed for various lengths of the nanorod. The higher the displacement is the higher the output voltage generated by the rod. This analysis still valid when

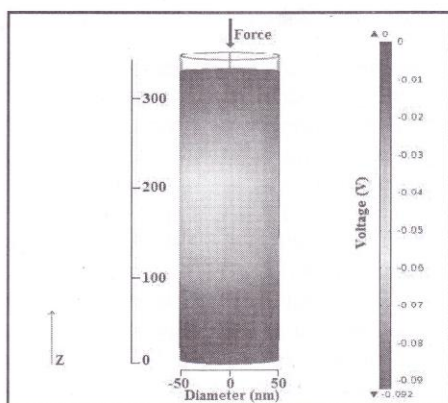


Figure 3. Distribution of a voltage generated along a nanorod under an applied force.

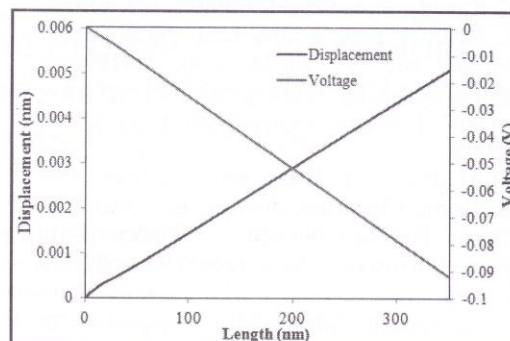


Figure 4. Mechanical displacement vs various lengths of the nanorods in comparison with an output voltage.

the applied force was raised to 100 nN and the output voltage reached 0.228 V.

#### CONCLUSION

This work has used a simple wet chemical method for obtaining free-standing zinc oxide or ZnO nanostructures. The starting agents and the chemistry of the interaction were chosen to produce wurtzite ZnO which is good piezoelectric. Ultra-low force is necessary to use to produce mechanical deformation of the nanorods. The output voltage is theoretically analysed that it could be generated by a static force of the order of 20-100 nN applied normal to the cross-sectional surface of the ZnO nanorod. Increasing the number of nanorods of different lengths and small diameters implies that a set of these ZnO piezoelectrics are possible to use as a nanogenerator.

#### ACKNOWLEDGEMENT

The Royal Golden Jubilee (RGJ) Ph.D. Fellowship, Thailand Research Fund (TRF), Ministry of Science & Technology, Bangkok and Research Grant from PSU Graduate School, and Center of Excellence in Nanotechnology for Energy, PSU have been gratefully thanks by the authors.

#### REFERENCES

- 1 N. Muensit, "Energy Harvesting Materials" in *Energy Harvesting with Piezoelectric and Pyroelectric* ed. N. Muensit, (Trans Tech Publications Ltd., Switzerland, 2011)

- Small-scale Energy ...  
Supasarote and kittirat*
- 2 S. Hurlebausa and L. Gaul, "Smart structure dynamics". *Mech. Syst. Signal. Pr.*20, 255–281 (2006)
  - 3 S. Roundy, E. S. Leland, J. Baker, E. Carleton, E. Reilly, E. Lai, B. Otis, J. M. Rabaey, P. K. Wright and V. Sundararajan, "Improving power output for vibration-based energy scavengers" *Pervasive Computing*4(1), pp. 28–36 (2005)
  - 4 M. H. Zhao, Z. L. Wang, and S. X. Mao, "Piezoelectric Characterization of Individual Zinc Oxide Nanobelt Probed by Piezoresponse Force Microscope" *Nano Letters*4(4), 587-590 (2004)
  - 5 H A. Sodano, "Macro-Fiber Composites for Sensing, Actuation and Power Generation", *Mechanical Engineering, Virginia Polytechnic Institute, United States of America.* (2003)
  - 6 X. Chen, S. Xu, N. Yao and Y. Shi, "1.6 V Nanogenerator for Mechanical Energy Harvesting Using PZT Nanofibers" *Nano letters* 10, 2133–2137 (2010)
  - 7 Z. L. Wang and J. Song, "Piezoelectric Nano generators Based on Zinc Oxide Nanowire Arrays" *Science*312, 242-245 (2006)
  - 8 L. Lin, C. H. Lai, Y. Hu, Y. Zhang, X. Wang, C. Xu, R. L. Snyder, L.,J. Chen and Z. L. Wang, "High output nanogenerator based on assembly of GaN nanowires" *Nanotechnology*22, 475401-475405 (2011)
  - 9 S. Suwanboon, P. Amornpitoksuk and S. Muensit, "Enhancement of Optical Bandgap and Luminescent Characteristics of One-dimensional ZnO Nanoparticles" *J. Ceram. Process. Res.*11(4), 419-424 (2010)
  - 10 PSU-Grid, 2011.
  - 11 Ü. Özgür, Ya. I. Alivov, C. Liu, A. Teke, M. A. Reshchikov, S. Doğan, V. Avrutin, S.-J. Cho And H. Morkoç, "A Comprehensive Review OF ZnO Materials AND Devices" *J. Appl. Phys.* 98, 041301(1-103) (2005)



## VITAE

**Name** Mr. Kittirat Phooplub

**Student ID** 5410230001

### **Educational Attainment**

<b>Degree</b>	<b>Name of Institution</b>	<b>Year of Graduation</b>
Bachelor of Science (Physics) (First Class Honors)	Prince of Songkla University	2010

### **Scholarship Awards during Enrolment**

1. The Royal Golden Jubilee (RGJ) Ph.D. Programme (PHD/0034/2553) from The Thailand Research Fund (TRF).
2. The Graduate School Research Support Funding for Thesis 2011 from Faculty of Science, Prince of Songkla University.

### **List of Publications and Proceedings**

#### **Publications**

1. **Phooplub, K.** Meesane, J. Muensit, N. 2018. Development of young's modulus for collagen thin films reinforced with ZnO nanorods probed by atomic force microscopy. *Biomedical Physics & Engineering Express* **4**(5): 055022
2. **Phooplub, K.** Muensit, N. 2018. Electro-mechanical properties of poly(vinylidene fluoride-hexafluoropropylene) reinforced with zinc oxide nanostructure. *Micro&Nano Letters* **13**(8): 1063-1067

#### **Proceedings**

1. **Phooplub, K.** Suanboon, S. Amornpitoksuk, P. Muensit, N. 2012. Low-dimensional piezoelectric materials for nanoenergy scavenging. *the 4th International Conference on Nanostructures*: 1759-1761.
2. Muensit, S. N. **Phooplub, K.** 2012. Small-scale energy harvesting with low-dimensional piezoelectrics. *Internal Conference on Physics and Its Applications*: 7-10

**Oral presentations**

1. **Phooplub, K.** Muensit, N. 2012 Small-scale energy harvesting with nanostructured piezoelectrics. *NanoThailand 2012*, April 9<sup>th</sup>-11<sup>st</sup>, 2014, Khon Kaen, Thailand.
2. **Phooplub, K.** Meesane, J. Muensit, N. 2012 Optimal configurations of a piezoelectric template proposed for collagen assembly. *Burapha University International Conference 2012*, July 9<sup>th</sup>-11<sup>st</sup> 2012 Chonburi, Thailand.

**Poster presentation**

1. **Phooplub, K.** Muensit, N. 2015 Observation of piezoelectric ZnO rods by atomic force microscope. *RGJ-Ph.D. Congress XVI*, June 11<sup>st</sup>-13<sup>rd</sup> 2015 Chonburi, Thailand